First draft of doctoral thesis

The interplay of flat band and disorder in extended Lieb lattices

学 位 申 请 人＿＿＿＿＿＿＿Jie Liu＿＿＿＿＿＿＿

指 导 老 师＿＿＿＿＿＿Rudolf A. Römer＿＿＿＿＿＿

学 院 名 称＿＿＿＿＿＿＿＿＿＿＿＿＿＿＿＿＿

学 科 专 业＿＿＿＿＿＿＿物 理 学＿＿＿＿＿＿

研 究 方 向＿＿＿＿＿＿＿计 算 物 理＿＿＿＿＿

二〇二三年八月十六日

The interplay of flat band and disorder in extended Lieb lattices

Candidate _____

Supervisor _____

College _____

Program _____ Physics _____

Specialization _____ Computational physics _____

Degree _____ Doctor of Philosophy _____

University _____

Date _____ August 16, 2023 _____

摘　要

晶格中波的局域化是指离散介质中不存在输运现象，人们在过去的几十年里面，对它进行了深入的研究。最值得注意的是，这种现象是由晶格中的杂质或者无序势场的存在所引起，从而导致了著名的 Anderson 局域化。然而，波的局域化也可能出现在平移不变的晶格中，其中相消干涉致使（至少一个）布洛赫能带群速度消失，导致宏观简并的本征态局域在晶格有限的格点上，此类局域态被称为紧凑的局域态（CLS）。这些具有无色散能带（平带）的单粒子能谱被称为平带晶格。

在本文中，我们研究了二维和三维平带晶格中的格点势能无序与平带的相互作用效应。由于 Lieb 模型是最简单的平带晶格，也是实验上最容易实现的晶格模型，所以我们主要研究 Lieb 模型及其扩展模型。首先，我们研究了二维 Lieb 模型及其扩展模型中的非关联无序效应。基于有限大小标度理论，我们发现平带处与色散带处的态确实具有完全不同的局域化性质，平带处的态似乎表现出一种类似一维情况的局域性质。然而，对于无序小至与跃迁能相当时，所有的无序仍然导致局域化。

然后，我们研究了三维 Lieb 模型及其扩展模型中的非关联格点无序效应，我们在能量—无序的相图中得到了金属—绝缘体转变曲线。我们发现三维 Lieb 模型及其扩展模型具有比简单立方晶格更低的临界无序，即 Lieb 模型更局域。此外，我们发现临界指数与标准的三维 Anderson 模型的临界指数是一致的。

最后，我们考虑有序势与无序势共存的情况，使得紧凑的局域态（CLS）被保留。有两个令人惊讶的结果，首先有一半的色散带上的非 CLS 态在能量上越发靠近平带能量，其行为也越发像 CLS，即更加局域在 Lieb 格点。其也导致了在 CLS 能量附近 DOS 的累积，最终导致在非常强无序下依旧存在扩展态，即出现了一个发散的迁移率边。其次，是靠近平带能量的小无序区域，出现"逆"Anderson 转变。我们也发现在较大无序区域的临界指数与标准的三维 Anderson 模型的临界指数是一致的。

我们的研究结果对平带晶格中无序与平带的相互作用研究具有重要的意义，可能为未来的信息存储器件提供新的思路，有利于推动量子存储器件设计相关领域的发展。

关键词：Anderson 局域化；平带；转移矩阵方法；能谱统计；有限大小标度理论

Abstract

Wave localization in lattices refers to the absence of transport in discrete media, and it has been intensively studied in the past decades. Most notably, this phenomenon is induced by the presence of impurities and disorder potential in the lattice —i.e. giving rise to the celebrated Anderson localization. However, wave localization may also emerge in translationally invariant lattices, where destructive interference yields the vanish of the group velocity in (at least) one of the Bloch bands, resulting in macroscopically degenerate eigenstates localized within a finite number of lattice sites. These lattices supporting dispersionless (or, flat) energy bands in the single-particle spectrum are called flat bands lattices.

In this thesis, we study the impact of onsite disorder potential in 2D and 3D flat band lattices. In particular, we mainly focus on the Lieb model and its extended versions, as the Lieb lattice is simultaneously one of the simplest and one of the most experimentally achievable flat band lattices.

First, we focus on the impact of uncorrelated disorder in 2D Lieb model and its extension. Based on the Finite size scaling method, we find that states at the flat band and dispersion band indeed have completely different localization properties, with the states at the flat band exhibiting a 1D-like localization behavior. However, for disorder small enough to be comparable to the hopping energy, all disorder still leads to localization.

Then, we focus on 3D Lieb model and its extensions with uncorrelated onsite disorder, where we outline the metal-insulator transition curve in the energy disorder phase diagram. We found that the 3D Lieb model and its extended models have a lower critical disorder strength compared to the simple cubic lattice, meaning that the Lieb model is more localized. Moreover, we found that the critical exponent value is in agreement with the exponent for the standard 3D Anderson transition.

Lastly, we consider a mix of order and disorder in the Lieb models such that the compact localized states (CLS) are preserved. There are two surprising results. First, about half of the non-CLS states on the dispersion band get pushed in energy close to the energy of the CLS and become concentrated on the Lieb sites. This also leads to the accumulation of density of states (DOS) near the CLS energy, eventually resulting in the existence of extended states even under strong disorder, i.e., the emergence of a diverging mobility edge. Second, near the flat band energy and under small disorder, an "inverse" Anderson transition occurs. We also found that the critical exponent in the large disorder

III

regime is consistent with that of the standard 3D Anderson model.

Our research results have significant implications for the study of the interaction between disorder and flat bands in a lattice, and may provide new insights for future information storage devices, which would be beneficial in advancing the field of quantum storage device design

Key Words: Anderson localization; flat band; transfer matrix method; energy spectrum statistic; finite size scaling method

目录

Chapter1 Introduction

1.1 Introduction to disorder system

1.1.1 Anderson localization

Since Anderson proposed the concept of disorder in 1958 [1], the disordered system has attracted much attention of scientists. It is well known that the wave vector k can be used to label the states in a perfect periodic solid system as the band theory, developed by F.Blochm R.Peierls, and A.H. Wilson in 1930s. This outstanding theory is successfully in recognizing metals, insulators, and semiconductors, based on the Bragg reflection in crystalline lattice. While, there are no perfect materials in real world, all of them are appeared with imperfections, such as impurities and vacancies, which destroyed the translation invariance of these system, and these systems are collectively called disorder systems. After including disorder, the system lost periodicity, and the wave vector k is not a good quantum number anymore. So we need new technical skills to explore the properties of disorder system.

Assuming considering a model without electron-electron interactions, and the electrons are only scattered by the random potential played by the disorder, this is known as *Anderson model*. In the case of weak disorder, the wave-function is a plane wave in short distance, while scattered in long distance by the disorder random potential. The distance over which the plane wave moves freely before being scattered is called as the *mean free path*. These multi-scattered waves, which extended to the whole system as the form

$$\Psi_k(\vec{r}) = u_k(\vec{r}) \exp(i\vec{k}\vec{r}) \ , \tag{1.1}$$

where λ is *localization length* and the corresponding states $\Psi(\vec{r})$ are called *localized states* as showed in Fig. 1.1. The transition from extended states to localized states driven by disorder, where induced a metal-insulator transition(MIT) as localized the whole states, is called *Anderson transition*. Let us consider a process that, the mean free path l is larger than the electronic wavelength λ_F(inverse of k_F) as the disorder is weak initially, i.e. $l \gg \lambda_F$. In this stage, the electrons can be assumed scattered by individual potential, and cause the *diffusive propagation*. The electrical conductivity can be expressed as the form $\sigma = e^2 D(E)\rho(E)$, where $D(E)$ and $\rho(E)$ are diffusive coefficient and density of states, respectively. With increasing disorder, the mean free length becomes more and more short, once it approach $l \sim \lambda_F$ for appropriate strong disorder, the properties changed dramatically. Physically, there is a Lifshitz criterion, which claims that localization is
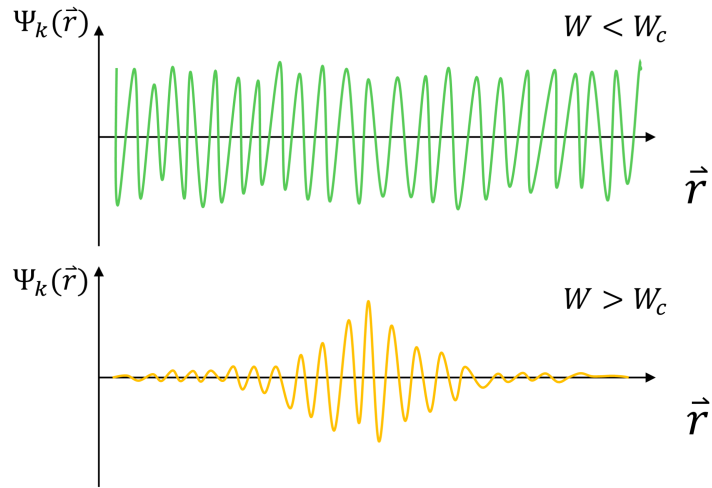
图 1.1: Extended(up) and localized(down) states.

expected when mean free path l is comparable to the wavelength λ_F for the strong disorder.

At our real life, things look more complicate as we need to deal with finite size system due to the maturity of technology, which enabling us to produce smaller structures, such as submicron devices, i.e. mesoscopic system. It makes us have to consider relation of system size L, and characteristic lengths, including mean free path l and localization length λ, to research the localization properties of disorder system. For weak disorder and a approximate large system, if inequalities $l \ll L \ll \lambda$ satisfied, the electron can diffuses through the whole system, where is called as *diffusive regime*. With increasing system size, once L is larger than λ, then electron becomes localized and can not spread out. On the contrary, if making the system shorter and shorter, and $L \ll l$, then the electrons can propagate through the whole system and scattered by only several random potentials, where is known as *ballistic regime*.

In the diffusive regime, the conductivity equation $\sigma = e^2 D(E) \rho(E)$ is fulfilled but with a small correction caused by quantum interference effects, as the quantum interference effects play an important role in the diffusive regime. The conductance shows an logarithmic decrease with increase of system size L, which is called weak localization correction.

1.1.2 Density of states (DOS) and mobility edge

In order to make our arguments more vivid, let us take a simple example of Anderson model. Considering a cubic lattice with constant hopping t for nearest neighbor, while other hopping terms remain zeros. For the onsite potential energy ϵ_{xyz}, it follows uniform

random distributed, .i.e in interval $[-W/2, W/2]$, where W is called disorder strength. In the absence of disorder W, it recovers to clean system with periodicity and we can give the dispersion relation as

$$E = 2t\cos(k_x) + 2t\cos(k_y) + 2t\cos(k_z) \quad, \tag{1.2}$$

where wave vector $\vec{k} = k_x\vec{i} + k_y\vec{j} + k_z\vec{k}$. The density of states(DOS) can be obtained analytically by $\rho(E) \sim \partial k/\partial E$[39]. The energy spectrum ranges from $-6t$ to $6t$, with symmetric distribution $\rho(E) = \rho(-E)$.

In the presence of disorder, density of states becomes a good measure of energy spectrum instead of dispersion relations, which is impossible to obtain because of the lack of spatial translation symmetry, leading us having no idea to get the analytical density of states anymore. Luckily, the numerical methods saved us and help us to get density of states by counting the number of states in a unit energy interval over different disorder configurations.

For appropriate disorder, extended and localized states coexist. Plenty of experience tells us that the localized states dwell on tails of energy band while extended on band center. There is a critical energy, E_c, separating extended states from localized states, is called *mobility edge* [Mott 1967] as showed in Fig. 1.2. If the Fermi energy E_F are located at regimes $E_F < E_c$, i.e. tails of band, where wavelength $\lambda_F \sim l$, the localization happens. Since the states around the Fermi energy are all localized, the system becomes an insulator, which is called *Anderson insulator*, where density of states are non-zero but with zero conductance. At the contrary, if $E_F > E_c$, states around the Fermi energy are extended, system can be regarded as a metal. By changing the Fermi energy from tails to center of band, i.e. across the mobility edge, the system takes a phase transition from insulator to metal.
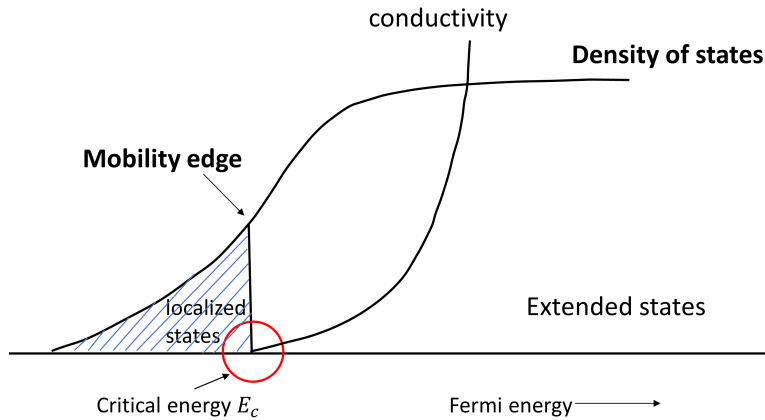
图 1.2: The concept of mobility edge.

Actually, there are two mobility edges in a band, E_{cU} and E_{cL}, and they tell extended

states in center apart from localized states in upper and lower band tails, respectively. Disorder can shift the mobility edge, as there are more extended states for weak disorder and more localized states for strong disorder. The increase of disorder is accompanied by the shift of mobility edge towards to center of band. When $E_{cU} = E_{cL}$ appeared, the two mobility edges coincide in the center of band. This corresponding special disorder W_c is known as critical disorder, since there are no more extended states in spectrum once any disorder $W > W_c$. Mobility edge, E_c, as a function of disorder W, .i.e. $E_c(W)$ gives the critical line, as in Fig. 4.2 dividing extended and localized states in $E - W$ phase diagram.

Need to mention, many techniques and theory results for electron are also suitable for phonons and spin waves with disorder.

1.1.3   Critical exponent and scaling relation

As the critical line separates the extended and localized states, .i.e metal and insulator, we can use two different quantities to represent the properties of different regions on both sides. The conductivity σ and localization length λ become the candidatures, where conductivity σ characterizes the transport properties in the metallic regime, while localization length λ characterizes the localization properties in the localized regime. As the metal-insulator transition is expected to be second order phase transition [2–4], the critical exponents emerge as the disorder and energy dependence of metallic conductivity and localization length on both sides of MIT. In the metallic regime, the conductivity $\sigma > 0$, while it is zero at the critical point W_c or E_c(at least for orthogonal system), which can be formed as

$$\sigma \sim (W_c - W)^s \tag{1.3}$$

or

$$\sigma \sim (E_c - E)^s \tag{1.4}$$

around the transition region. On the contrary, the localization length around the transition region can be expressed as

$$\lambda \sim (W - W_c)^{-\nu} \tag{1.5}$$

or

$$\lambda \sim (E - E_c)^{-\nu} \quad , \tag{1.6}$$

which is divergent at the exact critical point [2]. The relationship between s and ν is determined by the Wegner scaling relation $s = (d - 2)\nu$ [5]. At our simulations, we can extract this exponent ν via finite-size scaling(FSS) [2, 6].

1.1.4 Scaling theory of localization

Scaling theory of localization [7], which is an one-parameter scaling theory based on the ideals of Thouless [8], assumes that for sufficiently large system, when increasing system size, the conductance with rescaled size doesn't depend on energy, disorder or system size, but only on the conductance itself,

$$\beta(g) = \frac{\partial \ln g}{\partial \ln L} \quad . \tag{1.7}$$

The large system size represents the size of system L is larger than the whole characteristic lengths in system, and all the microscopic details can be regarded as irrelevant.

However, the form of the function $\beta(g)$ can be only described qualitatively from two limits. First, consider the conductance is infinity, then Ohm's law is expected to apply, .i.e

$$g \sim \sigma L^{d-2} \quad , \tag{1.8}$$

later we obtain $\beta(g) = d - 2$. Second, we consider the conductance as small as possible, namely $g \ll 1$, the expected exponential localization behavior gives the form as

$$g \sim \exp(-L/\lambda) \quad , \tag{1.9}$$

and thus $\beta(g) \sim \ln g$. Without loss of generality, if assuming $\beta(g)$ is always a continuous and monotonically increasing function. Then we can make a plot by interpolating between two limits as showed in Fig. 1.3.

For $d < 2$, function $\beta < 0$ indicates g decreases with increasing L; for the system with infinite size, it reaches to a localized regime and all states are localized, thus there are no metal-insulator transition appeared. For $d = 2$, as it is a critical regime, it is difficult to determine whether there is a phase transition. But it is generally believed that no metal-insulator transition occurs, and that all states are localized. For the case of $d > 2$, a fixed point $\beta = 0$ exist, which implying the conductance g is independent of system size and remains a constant, g_c; for initial conductance $g = g_c + \delta g$, where $\beta > 0$, g increases with L and reaches the metal regime; while for initial conductance $g = g_c - \delta g$, where $\beta < 0$, g decreases with L, and approaches the insulator regime. Thus, there is a metal-insulator transition separated by critical point g_c.

In conclusion, the scaling theory is a semiquantitative success based on the trade-off that focus on some important feature on macroscopic scales, but discard the microscopic details. This theory predicts that there are no metal-insulator transition in 1D and time-reversal invariant 2D system, but appeared in higher dimension, such as 3D.
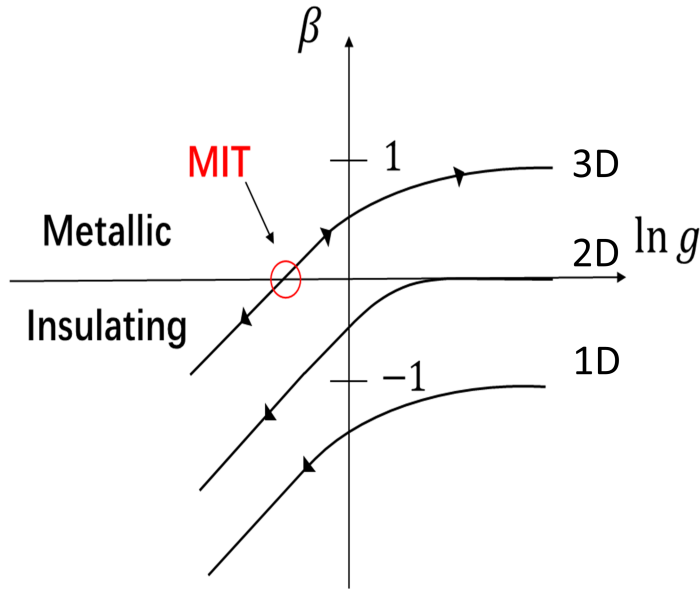
图 1.3: The schematic diagram of one-parameter scaling hypothesis. The arrow is the direction of flow with increasing system size.

1.1.5   Universality

In the topic of critical phenomena, the university is an inescapable concept. Under plenty of experiments, we have the belief that the critical exponents remain constant regardless the change of microscopic details of the Hamiltonian. Instead, what determine the university class are dimension and symmetries of the system. Of course, some quantities, such as the precise value of critical disorder W_c or critical energy E_c, are dependent on the microscopic details and thus are no-universal.

Within the early classification scheme corresponding to Wigner-Dyson classification of random matrix theory(RMT) ensembles, three universality classes for Anderson transition, .i.e , orthogonal, unitary and symplectic are be defined. The scheme are mainly considered two symmetries, namely the invariance of the Hamiltonian under time reversal and spin rotations, details are showed in Table 1.1. Although it has been understood that a complete set of random matrix theories includes, in addition to the three Wigner-Dyson classes, three chiral ensembles and four Bogoliubov-de Gennes ensembles, and the additional ensembles are characterized by one of the additional symmetries–chiral or the particle-hole [3], other symmetries don't play a big role in disorder system. We can simply use these three categories as detailed in Table 1.1.

The verification of the universality of critical exponents, and the dependence of symmetry and dimension is the main problem in disorder system referred to Anderson localization.

universality class	TRS	SRS	H
orthogonal	yes	-	real, symmetric
unitary	no	yes	complex, self adjoint
symplectic	yes	no	real, symplectic

表 1.1: Universality classes

1.1.6 The observation of Anderson localization in experiment

It is rather difficult to find a clean experimental system to observe the Anderson transition unambiguously. Cold atomic matter waves are very attractive because they an be directly observed, and most experimental imperfections as well as atom-atom interactions can be precisely controlled within limits. The observation of Anderson localization for matter waves. [9] has been realized by Juliette Billy et al in 2008 with cold atom system. As shown in Fig. 1.4(a), the BEC is obtained by magnetic-optical traps, where the details are in the caption. The wave packet begins to evolve after longitudinal trap is switched off and then localizes, which is exhibited in Fig. 1.4(b). Fig. 1.4(c) shows the density profiles in semi-log coordinates, the light red line represents that the initial wave packet locates at origin, the dark red line is the data one second after release, where the system has approached stationary regime, and the blue line is the exponential fits, which shows localization properties.

All the results in experimental for Anderson localization are qualitative at present, the quantitative results of quantum simulations are always a difficult problem.

1.2 Introduction to flat band and its applications

1.2.1 Flat band, CLS and generation of flat band

Flat band is the k-independent dispersion relation, and is a flat straight line in $k - E$ energy spectrum graph. The flat band is different from the normal parabolic and Dirac linear dispersion relations as showed in Fig. 1.5.

The eigenstates corresponding to flatbands are typically spatially compact – *i.e.* they span over a finite subsection of the lattice. Hence, they are called "Compact localized state" (CLS). Examples of one-dimensional flat band networks and their correspondent CLS can be seen in Fig. 1.6, where the CLS are highlighted with the black dots

Based on the tight-binding method, basically, there are two methods to generate a lattice with flat band. One is through symmetry, and the other is through fine-tuning the coupling. The original flat band models, dice lattice [11], followed by Lieb lattice [12], both
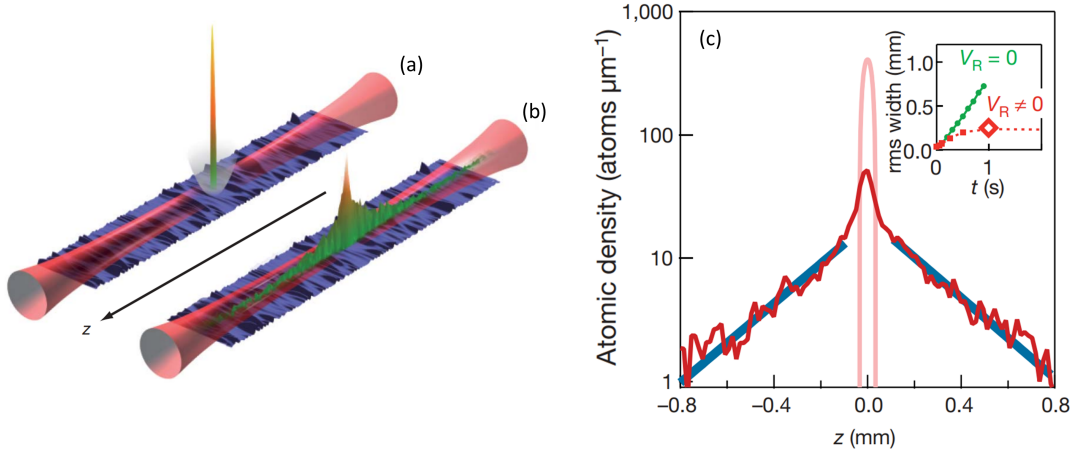
图 1.4: Direct experimental observation of one-dimensional Anderson localization of an atomic matter wave in a disorder potential. Observation of exponential localization. (a), A small BEC(1.7×10^4 atoms, we call it wave packet for convenience) is formed in a hybrid trap that is the combination of a horizontal optical waveguide, offering a strong transverses confinement(in x-y plane) that ensures an effectively one-dimensional dynamics, and a loose magnetic longitudinal trap that makes the wave packet initially at the center. The disorder potential with amplitude V_R is created by a speckle pattern as shown in blue. (b), Once the longitudinal trap is switched off, the wave packet evolves freely, diffuses and eventually freezes at long times in a characteristic exponential shape. (c), The atomic density profiles, the light red line shows the initial result, the dark red line shows the result one second after release, and the blue line is the fit result. In the inset, it is the root-mean-square(rms) width of the profile versus time t, which shows the stationary regime is reached after $0.5s$. The figures are taken from paper [9].
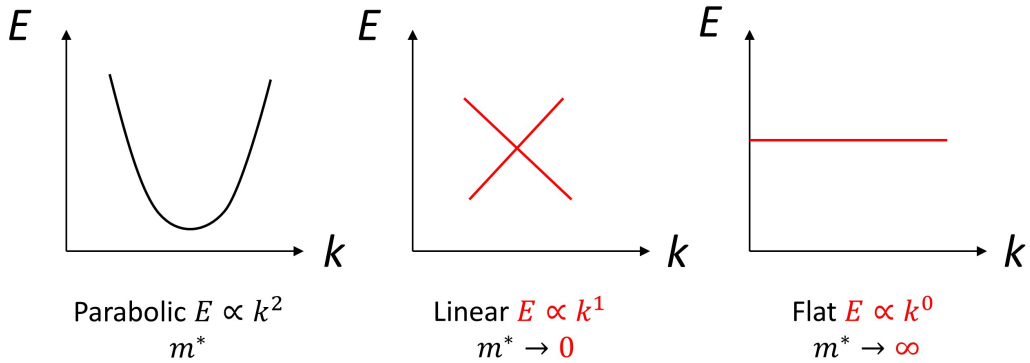
图 1.5: Types of dispersive bands. (a) the normal parabolic dispersion relation, (b) the Dirac type dispersion relation and (c) the flat band dispersion relation.

are with chiral symmetry. Mielke proposed the flat band models based on line graphs [13],
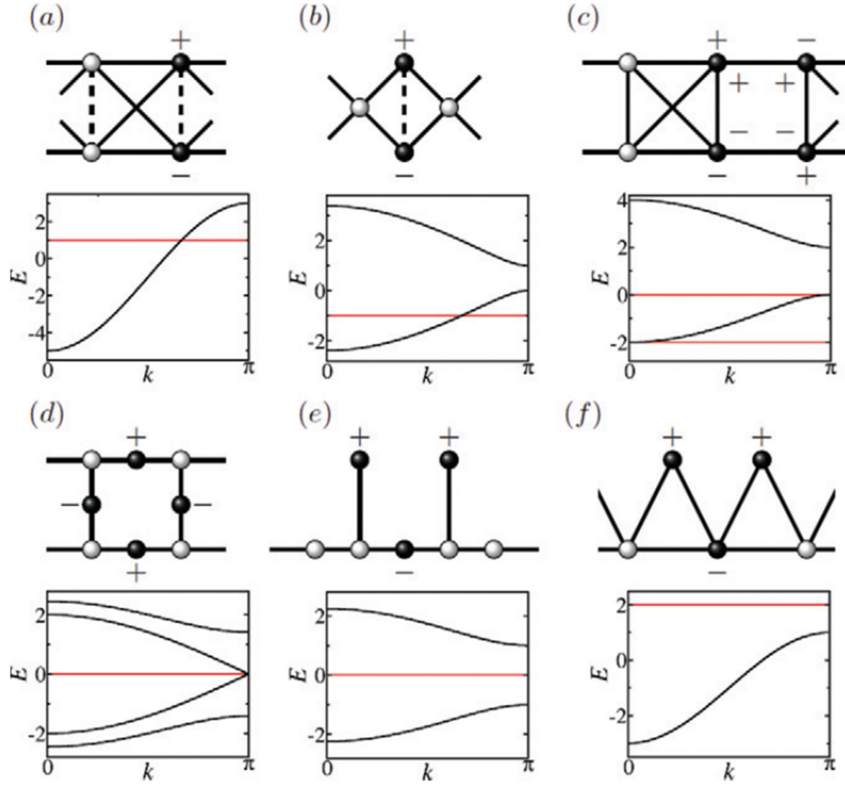
图 1.6: 1D flat band lattices. Circles denote lattice sites, solid lines are hopping elements $t_{jj'} = 1$ and dashed lines are hopping with tunable value t. Filled circles show the localization of a compact localized state with identical wave amplitudes and alternating signs as indicated, other lattice sites have strict zero amplitudes. The irreducible band structure is shown below each lattice. (a) Cross-stitch, (b) diamond chain, (c) 1D pyrochlore, (d) 1D Lieb, (d) stub and (f) sawtooth chain. (Figure is taken from Ref. [10])

and Tasaki put forward the "decorated" lattices [14], which are by fine-tuning coupling.

Later, CLS were used as the "generator" of flat band. According to the size of CLS, $U-$ the unit cell size CLS occupied, the flat bands have different type. For $U = 1$, the flat band is protected with local symmetry [10], as it can be completely decoupled from the rest of lattice by a local change of basis; while for $U > 1$, the flat band is generated by fine-tuning coupling [15], rather than a local symmetry. However, as CLS-based construction methods just works for one-dimensional lattices, a complete generalization to higher dimension remains an open problem. The new methods need to be developed, such as origami rules [16], repetition of oligomers [17], local symmertries [18], an self-similar constructions [19, 20].

1.2.2   Why flat bands are charming

The disappearance of group velocity $\nabla_k E$ of flat band, .i.e quenched kinetic energy, makes the potential prominent. Thus, it becomes a ideal platform to achieve the strong correlated system. The flat band is sensitive to the presence of disorder and interaction, and results in a nonzero dispersion.

As talked in previous part, the disorder can induce Anderson localization and result in phase transitions. Besides disorder, the presence of flat band will also exert an influence on localization properties, such as modifying the scaling of localization length in 1D [21–23], and mobility edge [24], inverse Anderson transition [25, 26] and disorder-induced topological phase transitions [**?**]. The interaction of quantum particles in flat bands, which inducing spontaneous symmetry breaking and resulting in a various strongly correlated quantum phases [27–33] attracted lots of attention. What's more, the incorporation of topology and flat band is another interesting area [34, 35].

In a word, as firstly introduced to analytically study ferromagnetic ground states in many-body systems [11, 12], flat band models have since been used to study a plethora of physical phenomena, such as fractional quantum Hall effect [36–38], spin liquids [39, 40], ferromagnetism [13, 41–43], disorder-free many-body localization [44, 45], superfluidity and superconductivity [46–52]. Hence, flat bands are indeed are charming to scientists.

1.2.3   The realization of flat band in experiments

With the mature of fabrication techniques, great progress has been made in the realization of flat band. For the electronic flat bands, Abilio et al. observed the flat band in superconducting wire networks [53]; Drost et al. [54] and Slot et al. [55], based on STM to control atoms, achieved independently the flat band in Lieb lattice, followed by Li et. al. [56], who observed the flat band in kagome lattice with multilayer silicene structure. In the optical flat band field, flat band in kagome lattice [57] was obtained by Jo et al., and Lieb lattices [58, 59] with flat band were also achieved. As for the photonic flat band, photonic systems [60–63] with flat band were implemented based on the femtosecond laser-writing technique; what's more, the kagome [64] lattice and Lieb [65] lattice were realized via terahertz spoof plasmons as well. The observation of flat band ground on the optical induction technique in Lieb [66] lattice and kagome [67] lattice, was reported over the same period.

1.3   The reasons for choosing this subject

The success preparation of artificial setting, implies there are many previous theoretical works that can be tested in experiments and new theoretical works need to be explored and explained. On the one hand, Lieb lattice, as its simple geometry structure and abundant physical properties, has been achieved in many settings, including photonic systems [60–62,65], optical cold atoms systems [58,59] and electronic systems [54,55]. On the other hand, there are more lavish properties on 3D systems than 2D systems, and it's easy to generalize 2D Lieb lattice to 3D Lieb lattice. Thus, Lieb lattice is a ideal lattice model to be considered.

The compact localized states(CLS), as the eigenstates of flat band in real space, occupy one or several unit cells, which means these states can not be spread out as they localized on these unit cells. However, the flat band consists of high-degenerated energy levels, which have the same eigenenergy, hence their eigenstates are not unique. A new state of linear combination of these eigenstates is also the eigenstate of the high-degenerated flat-band eigenenergy. This new state can even occupy specific lattice points throughout the whole lattice, hence it is counter-intuitive that all CLS are localized.

After introducing disorder in the CLS system, on the one hand, the disorder depresses the transportation as the Anderson localization, on the other hand, the disorder destroys the high-degenerated flat band, .i.e CLS, which can recover to delocalization. The idea for our work comes from that if including small disorder, the CLS are largely retained, .i.e the state occupied specific lattice points throughout the whole lattice is retained. Then the natural question to ask is whether delocalization occurs in the 2D disorder system or more novel properties appears in 3D disorder system. Based on this question, we carried out our study showed in this section.

The Lieb model and its extensions, $\mathcal{L}_2(n)$, $n = 1, 2, 3, 4$, are our experimental models. The disorder W are introduced by changing the potentials on cube and hube sites, equivalently, and the hopping potentials t are set to 1 as the energy scale.

Chapter2   Models and Methods

2.1   Models

2.1.1   The extended Lieb lattices $\mathcal{L}_d(n)$

The 2D and 3D extended Lieb models can be considered as inserting atoms uniformly spaced between two neighbor sites in square and cube lattices, respectively. Symbol $\mathcal{L}_d(n)$ represents a d-dimensional model with n inserted atoms between two neighbor sites of original lattice, .i.e, $n = 2$ is two-dimensional square lattice and $n = 3$ is three-dimensional cube lattice, as showed in Fig. 2.1. For convenience, we call the original atoms of square(cube) lattice *square*(*cube*) sites, the later-inserted atoms *Lieb* sites.

<div style="text-align:center">(a)   (b)   (c)   (d)</div>
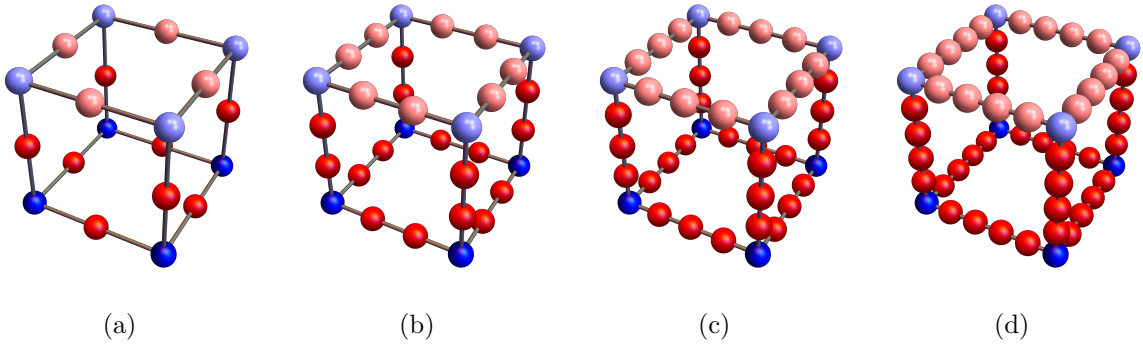
图 2.1: (a-d) Schematic representation of Lieb and extended Lieb lattice $\mathcal{L}_d(n)$. The lightly colored spheres highlight the situation in 2D while together with the fully colored spheres they represent 3D lattices. Blue spheres denote the cube sites while red spheres denote the Lieb sites. The dark lines between sites are guides to the eye and indicate the hopping profiles.

2.1.2   Anderson model based on the Lieb lattice $\mathcal{L}_2(1)$ and it's Wannier representation

To explore the effects of disorder, we adopt the Anderson model. The Anderson model [1] is a simple one-electron model for such a disorder-driven MIT, neglecting spin-orbit coupling, electron-electron interactions and the presence of magnetic field. The Hamiltonian consists two competing terms, a random onsite potential term tending to retain the particle in the energy minima and a kinetic energy term allowing hopping from site to site. We start from writing the Hamiltonian of Anderson model based on the $\mathcal{L}_2(1)$ lattice, it gives as below,

$$H = \sum_{\vec{r}} \varepsilon_{\vec{r}} |\vec{r}\rangle\langle\vec{r}| - \sum_{\vec{r}\neq\vec{r}\prime} t_{\vec{r}\vec{r}\prime} |\vec{r}\rangle\langle\vec{r}\prime| \ , \tag{2.1}$$

here, the set of $|\vec{r}\rangle$ indicates the orthonormal Wannier states corresponding to electrons located at sites $\vec{r} = (x, y)$ of the Lieb lattice $\mathcal{L}_2(1)$ and $\varepsilon_{\vec{r}}$ is the onsite potential [68]. Normally, the Anderson disorder is achieved by introducing the $\varepsilon_{\vec{r}}$ with uniformly distributed potential in the interval $[-W/2, W/2]$. As usual, we set the hopping integrals $t_{\vec{r},\vec{r}\prime} \equiv 1$ for nearest-neighbor sites $\vec{r}$ and $\vec{r}\prime$ and $t_{\vec{r},\vec{r}\prime} \equiv 0$ otherwise.

In the real space representation, we can write the Hamiltonian in the matrix form. In the concrete, let's take the $\mathcal{L}_2(1)$ with $M = 2$ with the hard boundary condition to elaborate. There are 3 atoms in a unit cell for $\mathcal{L}_2(1)$, hence the system for $M = 2$ has $12(3 \times 2^2)$ atoms such that the hamiltonian is a 12×12 matrix, and it can be expressed as bellow,

$$\begin{bmatrix} \varepsilon_1 & 1 & 1 & 0 & 0 & 0 & 0 & 0 & 0 & 0 & 0 & 0 \\ 1 & \varepsilon_2 & 0 & 1 & 0 & 0 & 0 & 0 & 0 & 0 & 0 & 0 \\ 1 & 0 & \varepsilon_3 & 0 & 0 & 0 & 1 & 0 & 0 & 0 & 0 & 0 \\ 0 & 1 & 0 & \varepsilon_4 & 1 & 1 & 0 & 0 & 0 & 0 & 0 & 0 \\ 0 & 0 & 0 & 1 & \varepsilon_5 & 0 & 0 & 0 & 0 & 0 & 0 & 0 \\ 0 & 0 & 0 & 1 & 0 & \varepsilon_6 & 0 & 0 & 0 & 1 & 0 & 0 \\ 0 & 0 & 1 & 0 & 0 & 0 & \varepsilon_7 & 1 & 1 & 0 & 0 & 0 \\ 0 & 0 & 0 & 0 & 0 & 0 & 1 & \varepsilon_8 & 0 & 1 & 0 & 0 \\ 0 & 0 & 0 & 0 & 0 & 0 & 1 & 0 & \varepsilon_9 & 0 & 0 & 0 \\ 0 & 0 & 0 & 0 & 0 & 1 & 0 & 1 & 0 & \varepsilon_{10} & 1 & 1 \\ 0 & 0 & 0 & 0 & 0 & 0 & 0 & 0 & 0 & 1 & \varepsilon_{11} & 0 \\ 0 & 0 & 0 & 0 & 0 & 0 & 0 & 0 & 0 & 1 & 0 & \varepsilon_{12} \end{bmatrix}, \tag{2.2}$$

where onsite potentials $\varepsilon_{\vec{r}} \in \left[-\frac{W}{2}, \frac{W}{2}\right]$ uniformly. Via exact diagonalization, we obtain 12 eigenvalues and 12 corresponding eigenstates.

Basically, the methods invented to explore the characteristic of disorder system are mainly based on analyzing eigenvalues and eigenstates, such as the statistic of spectrum including $P(s)$ and improved versions, .i.e, the statistics of spectral gap ratio $P(r)$, $P(|z|)$, and the inverse participation numbers(IPN) and so on, which we will introduce in detail later.

2.2　The CLS of $\mathcal{L}_d(n)$

In order to have a deeper insight into CLS for $\mathcal{L}_2(n)$. Firstly, we consider $\mathcal{L}_2(1)$ and $\mathcal{L}_2(2)$ with small size, and calculate the eigenvalues and eigenstates via exact diagonalization method. As the CLS is a concept in block material, we infer the condition in the thermodynamic limits. Next, from $\mathcal{L}_2(1)$ and $\mathcal{L}_2(2)$, we get the generalization of $\mathcal{L}_2(n)$. Last, we provide a new scheme to construct the CLS for $\mathcal{L}_2(n)$.

2.2.1　The CLS of $\mathcal{L}_2(1)$

We start from $\mathcal{L}_2(1)$ with finite Lieb plaquettes, and focus on the distributions of their $E = 0$ eigenvalues and eigenstates. Later, we can deduce that with infinite Lieb plaquettes, .i.e, in the thermodynamic limit, which includes the CLS.

The eigenenergies and eigenstates for $\mathcal{L}_2(1)$ with finite size plaquettes

First, we start from $\mathcal{L}_2(1)$ with 1 Lieb plaquette as shown in Fig. 2.2, based on the tight-binding method, the Hamiltonian gives as,

$$H = \sum_{\vec{r}} \varepsilon_{\vec{r}} |\vec{r}\rangle\langle\vec{r}| - \sum_{\vec{r} \neq \vec{r}\prime} t_{\vec{r}\vec{r}\prime} |\vec{r}\rangle\langle\vec{r}\prime| \ . \tag{2.3}$$

Here, the set of $|\vec{r}\rangle$ indicates the orthonormal Wannier states corresponding to electrons located at sites $\vec{r} = (x, y)$ of the Lieb lattice $\mathcal{L}_2(1)$, $\varepsilon_{\vec{r}}$ is the onsite potential and $t_{\vec{r},\vec{r}\prime}$ is the hopping integrals. Here for convenience we set the onsite potential to zero and hopping term to 1 for nearest-neighbor sites while zero otherwise.

图 2.2: The lattice diagram of $\mathcal{L}_2(1)$ with 1 Lieb plaquette and the distribution of amplitudes of eigenstates for $E = 0$.

The matrix form of Hamiltonian in the Wannier representation is given by

$$
\begin{bmatrix}
0 & 1 & 1 & (1) & 0 & (1) & 0 & 0 \\
1 & 0 & 0 & 1 & 0 & 0 & 0 & 0 \\
1 & 0 & 0 & 0 & 0 & 1 & 0 & 0 \\
(1) & 1 & 0 & 0 & 1 & 0 & 0 & (1) \\
0 & 0 & 0 & 1 & 0 & 0 & 0 & 1 \\
(1) & 0 & 1 & 0 & 0 & 0 & 1 & (1) \\
0 & 0 & 0 & 0 & 0 & 1 & 0 & 1 \\
0 & 0 & 0 & (1) & 1 & (1) & 1 & 0
\end{bmatrix},
\tag{2.4}
$$

the numbers 1 in parentheses () present the periodic condition, and they are zero for hard boundary condition. Here, we mainly consider with hard boundary condition. After exact diagonalization 8 eigenenergies and eigenstates are obtained. We find there is one eigenenergy of $E = 0$ with eigenstate $(0, 1, -1, 0, -1, 0, 1, 0)^{\top}$ and we plot these amplitudes in Fig. 2.2. Apparently, the amplitudes on *square* sites are all zero, originating from the destructive interference of neighbor *Lieb* sites. By the way, there is an accidental eigenenergy of $E = 0$ with eigenstate $(1, 0, 0, -1, 0, -1, 0, 1)^{\top}$, whose amplitudes are all located at *square* sites. However the value of this accidental eigenenergy will shift while holding the eigenstate constant if changing the hard boundary condition to periodic condition.

图 2.3: The lattice diagram of $\mathcal{L}_2(1)$ with 4 Lieb plaquettes. (a-c) are three distributions of amplitudes of eigenstates for $E = 0$. For intuition, we just show the non-zero amplitudes.

Further, we go to the $\mathcal{L}_2(1)$ with 4 Lieb plaquettes as shown in Fig. 2.3. Via the same method, we can obtain 21 eigenenergies and eigenstates. There are 4 degenerated eigenenergies $E = 0$, and three distributions of amplitudes of their eigenstates are plotted in Fig. 2.3(a-c).

Actually, as the eigenenergy $E = 0$ is degenerate, hence its eigenstate is not unique. For instance, if a eigenvalue λ_1 with eigenstate ψ_1 satisfying $H\psi_1 = \lambda_1\psi_1$, and another eigenvalue λ_2 with eigenstate ψ_2 satisfying $H\psi_2 = \lambda_2\psi_2$. When $\lambda_1 = \lambda_2 = \lambda$, we call eigenvalue λ degenerate. The new vector $\psi = a\psi_1 + b\psi_2$ is also the eigenstate of H with the same eigenvalue λ, as

$$H\psi = H(a\psi_1+b\psi_2) = aH\psi_1+bH\psi_2 = a\lambda_1\psi_1+b\lambda_2\psi_2 = a\lambda\psi_1+b\lambda\psi_2 = \lambda(a\psi_1+b\psi_2) = \lambda\psi. \tag{2.5}$$

Apparently, the third eigenstate as shown in Fig. 2.3(c) can be seen as the superposition as the first and the second eigenstates showed in Fig. 2.3(a) and Fig. 2.3(b), respectively. Nevertheless, we can extract the irreducible eigenstate, which just occupying one 2D Lieb plaquette of the lattice as shown in Fig. 2.3(a) and 2.3(b). There are four small Lieb plaquettes in Fig. 2.3, namely top left, top right, bottom left and bottom right, and there are exactly four degenerate eigenvalues $E = 0$.

Interesting, similar to $\mathcal{L}_2(1)$ with 1 plaquette, there is also an accidental eigenenergy of $E = 0$, whose eigenstate occupies only the *square* sites contrary to previous 4 degenerate eigenstates, but this accidental eigenenergy of $E = 0$ is destroyed by changing from hard boundary condition to periodic boundary condition.
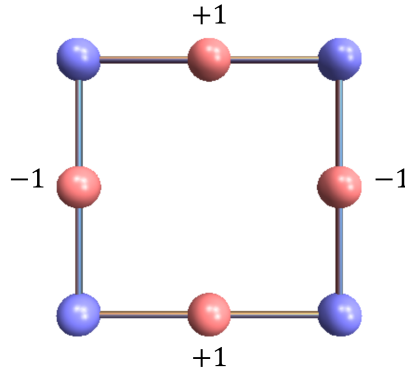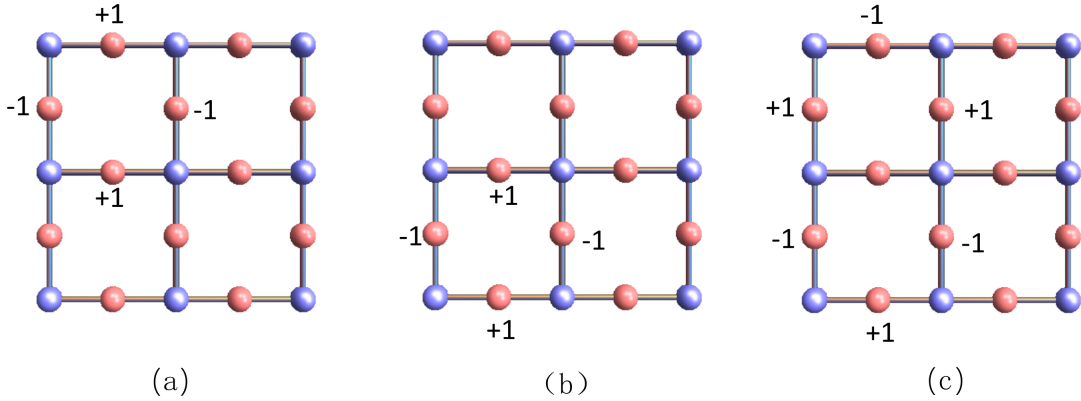

图 2.4: The lattice diagram of $\mathcal{L}_2(1)$ with 9 Lieb plaquettes. (a-b) are three distributions of amplitudes of eigenstates for $E = 0$. For intuition, we just show the non-zero amplitudes.

In order to get more information, we calculate the $\mathcal{L}_2(1)$ with 9 Lieb plaquettes. Indeed, we obtain 9 degenerate eigenvalues $E = 0$ whose amplitudes of eigenstates are only located on *Lieb* sites as shown in Fig. 2.4. Similarly, there is also an accidental eigenvalue $E = 0$ with amplitude only occupying *cube* sites. But it will be ruined after changing from hard boundary condition to periodic condition as well.

The deduction for $\mathcal{L}_2(1)$ with infinite size plaquettes and its CLS

From the above results, we can infer that there are infinite number of eigenenergies $E = 0$ for $\mathcal{L}_2(1)$ in the thermodynamic limit. Based on the band theory, these highly-degenerated eigenenergies forms an special energy band which is called flat band as it's a horizontal line in the $E - k$ space. Their corresponding eigenstates are not fixed as they are degenerate, but we can easily extract their irreducible eigenstates which occupying only the *Lieb* sites within one Lieb plaquette. These eigenstates corresponding highly-degenerated energy in the real space representation are known as *compact localized states*, namely CLS.

2.2.2   The CLS of $\mathcal{L}_2(2)$

Similar with $\mathcal{L}_2(1)$, we repeat previous steps and take the eigenvalues and eigenstates for $\mathcal{L}_2(2)$ with finite size plaquettes. Later, we can deduce that with infinite Lieb plaquettes, .i.e, in the thermodynamic limit, which includes the CLS.

The eigenenergies and eigenstates for $\mathcal{L}_2(2)$ with finite size plaquettes

Firstly, we turn into $\mathcal{L}_2(2)$ lattice with 1 plaquette, we obtain one eigenenergy $E = -1$ and another $E = +1$, and their amplitudes of eigenstates are plotted in Fig. 2.5(a) and Fig. 2.5(b), respectively. We find the amplitudes of eigenstates are all located at the *Lieb* sites while are zero at *cube* sites. What's more, there is an accidental eigenvalue $E = 1$ and $E = -1$ but will ruined after changing from hard boundary condition to periodic boundary condition as well.
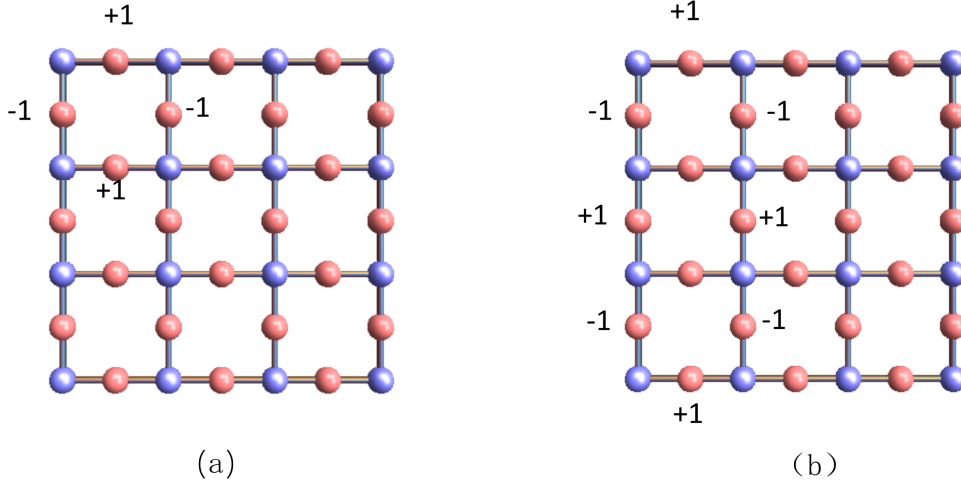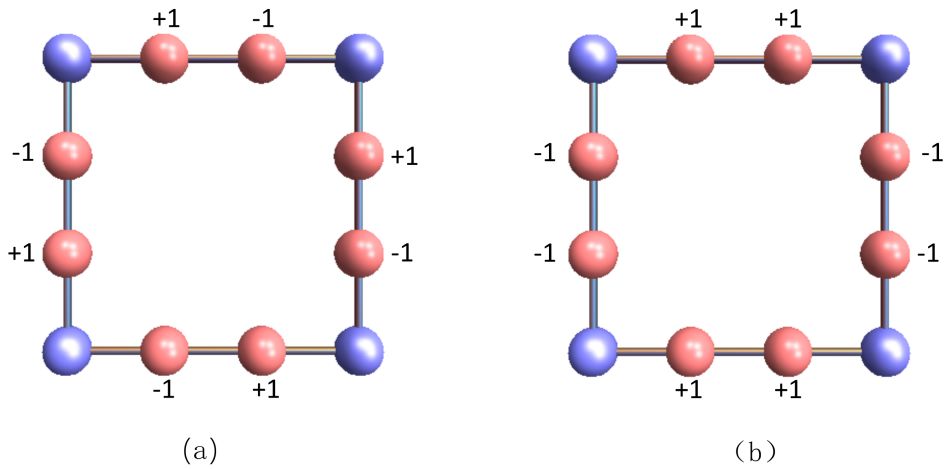

图 2.5: The lattice diagram of $\mathcal{L}_2(2)$ with 1 Lieb plaquettes. (a) and (b) are two distributions of amplitudes of eigenstates for $E = -1$ and $E = 1$, respectively. For intuition, we just show the non-zero amplitudes.

Further, we increase the plaquettes up to 4 for $\mathcal{L}_2(2)$. As expected, we get 4 of the identical eigenenergy both for $E = -1$ and $E = 1$, and the amplitudes distributions of one of 4 eigenstates for both are exhibited in Fig. 2.6 (a) and Fig. 2.6 (b), respectively. However, there is no accidental eigenvalues $E = -1$ or $E = 1$ as $\mathcal{L}_2(2)$ with one plaquette.

(a)   （b）
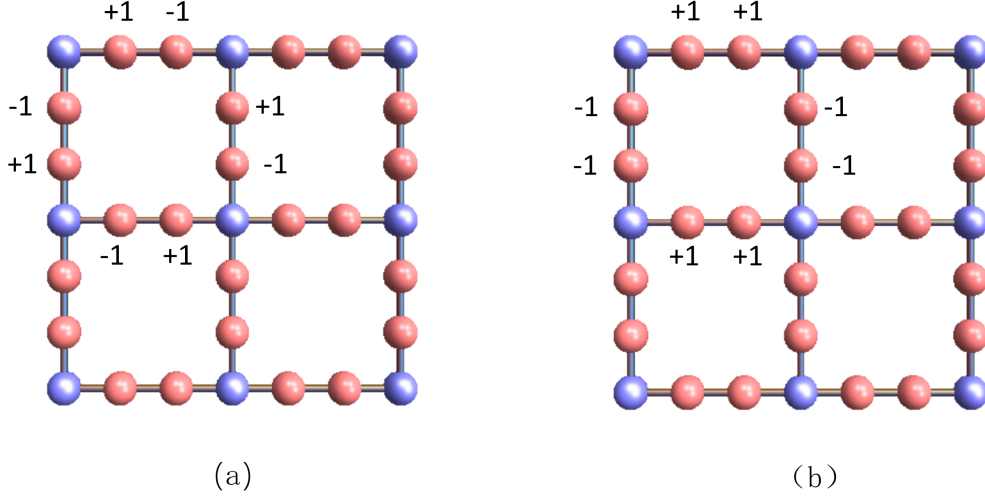
图 2.6: The lattice diagram of $\mathcal{L}_2(2)$ with 4 Lieb plaquettes. (a) and (b) are two distributions of amplitudes of eigenstates for $E = -1$ and $E = 1$, respectively. For intuition, we just show the non-zero amplitudes.

The deduction for $\mathcal{L}_2(2)$ with infinite number of plaquettes and its CLS

We guess there are an infinite number of $E = 1$, as well as $E = -1$ for $\mathcal{L}_2(2)$ in the thermodynamic limit, and they form two flat bands at $E = 1$ and $E = -1$ in the $E - k$ space. Their irreducible eigenstates are just located at the *Lieb* sites within one plaquette. These eigenstates corresponding to the highly degenerated energy $E = 1$ and $E = -1$ in the representation of real space are called compact localized states(CLS).

2.2.3 The CLS of $\mathcal{L}_2(n)$

Apparently, for $\mathcal{L}_2(n)$, there are n degenerate flat bands. Thus, for any n, there exist n-families of macroscopically compactly localized states (CLS), all of which have strictly non-zero amplitude in the Lieb sites enclosed within each 2D square plaquette of the lattice – as shown in Fig. 2.7. As we just consider the n up to 4 in our paper, we just show the four cases.

Since the above method is introduced by direct diagonalization, which is hard to go ahead for large scale systems. Based on the previous results, now we introduce a new scheme to construct the CLS for $\mathcal{L}_2(n)$ with any n.

(a) $E = 0$

(b) $E = \pm 1$

(c) $E = 0, \pm \sqrt{2}$

(d) $E = \pm \frac{1}{2} \left(1 \pm \sqrt{5} \right)$
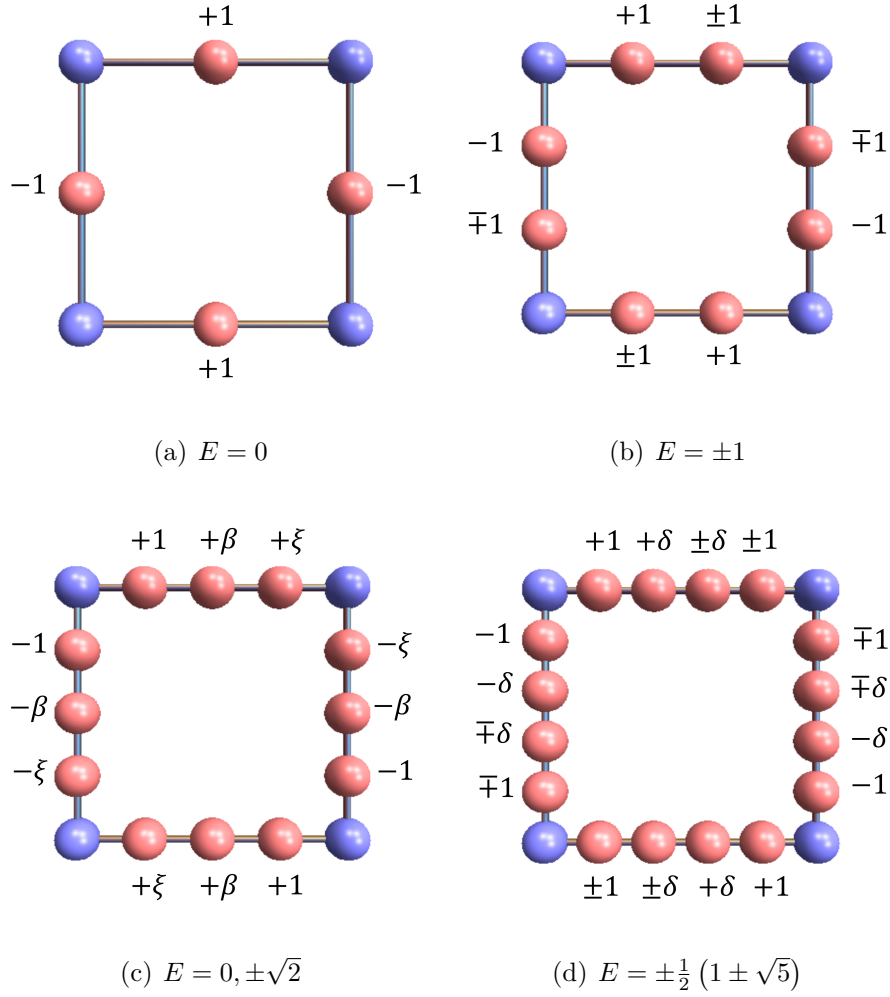
图 2.7: (a-d) Plaquettes with their CLS indicated by their (unnormalized) wave function amplitudes $|\vec{r}\rangle$. In (a-d) the flat bands are (a) $E = 0$ for $n = 1$ and (b) $E = \pm 1$ for $n = 2$. In (c), for $n = 3$ the three flat bands are $E = \beta = 0, \pm \sqrt{2}$, with $\xi = +1$ for $\beta = \pm \sqrt{2}$ and $\xi = -1$ for $\beta = 0$. In (d), for $n = 4$ the four flat bands are $E = \pm \delta$, with $\delta = \frac{1}{2} \left(1 \pm \sqrt{5} \right)$.

As the irreducible CLS for $\mathcal{L}_2(n)$ have strictly non-zero amplitude in the Lieb sites only within a 2D plaquette of the lattice. Thus, it is instructive to focus on a 2D plaquette enclosed within four neighbouring cube sites – highlighted in green color in Fig. 2.8(a), left side. We consider the 1D chain formed by the n Lieb sites in one of the four edges of the plaquette. We then denote by $v^j = (v_1^j, \ldots, v_n^j)$ one of the n eigenstates of this 1D chain with eigenenergy λ_j – as sketched in Fig. 2.8(a).

A CLS of $\mathcal{L}_2(n)$ is then constructed by looping v^j around the plaquette as shown in Fig. 2.8(b). Proceeding clockwise from top-left, the construction works as follows:
– in <u>Step 1</u> we consider v^j along the upper edge. Hence, the amplitudes on the Lieb sites next to the top-left and top-right cube sites are v_1^j and v_n^j, respectively;
– in <u>Step 2</u> we ensure destructive interference in the top-right cube site of the plaquette

(colored in yellow and indicated with a thunder symbol) by setting $-v_n^j$ in the top Lieb site of the right edge of the plaquette. The remaining $n-1$ Lieb sites are then filled by $-v_i^j$ with the index i running in a downward direction. The amplitude of the bottom Lieb site of this chain thus is $-v_1^j$;

– in Step 3 we ensure destructive interference in the bottom-right cube site of the plaquette (highlighted alike Step 2) by setting v_1^j in the right Lieb site of the bottom edge of the plaquette. The remaining $n-1$ Lieb sites are then filled by v_i^j with the index i running in a leftward direction. The amplitude of the most-left Lieb site of this chain thus is v_n^j;

– in Step 4 we ensure destructive interference in the highlighted bottom-left cube site of the plaquette by setting $-v_n^j$ in the bottom Lieb site of the left edge of the plaquette. The remaining $n-1$ Lieb sites are then filled by $-v_i^j$ with the index i running in a upward direction. The amplitude of the top Lieb site of this chain thus is $-v_1^j$, which ensures destructive interference in the highlighted top-left cube site.

This iterative procedure yields a compact eigenstate of energy λ_j. Since there exist n eigenstate $\{v^i\}_{i=1}^n$ with energies $\lambda_i \neq \lambda_j$ for $i \neq j$ for the 1D chain of n Lieb sites, this construction can be done n times – generating n families of CLS for the lattice $\mathcal{L}_2(n)$, and therefore n flat bands $\{\lambda_i\}_{i=1}^n$.

(a)   (b)
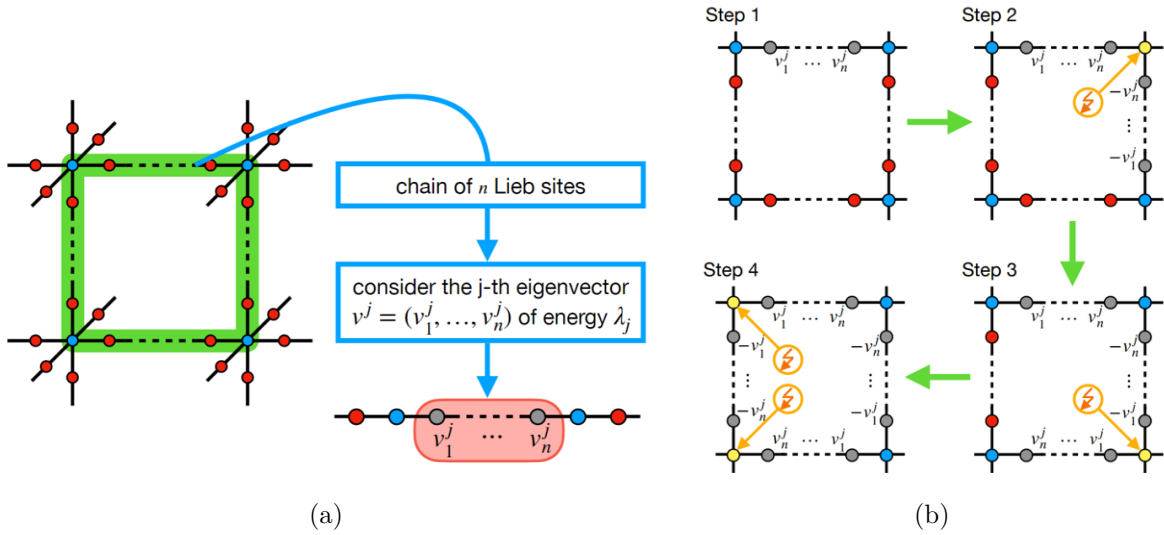
图 2.8: (a) Section of the lattice $\mathcal{L}_2(n)$ around a 2D plaquette (green color). We consider the 1D chain formed by the n Lieb sites sandwiched between two cube sites along one edge of the plaquette, and highlight one of the eigenstate v^j of eigenenergy λ_j. (b) Four steps construction of a CLS of $\mathcal{L}_2(n)$ with energy λ_j by looping v^j around the 2D plaquette. In each step, we highlight in yellow and with the thunder symbol the cube site where the destructive interference is enforced.

2.2.4   The CLS of $\mathcal{L}_3(n)$

In order to figure out the CLS of $\mathcal{L}_3(n)$, firstly we take $\mathcal{L}_3(1)$ with finite cells following the same steps as for $\mathcal{L}_2(n)$. After computing the eigenenergies and eigenstates with exact diagonalization, we can analyse these eigenstates and eigenstates of $\mathcal{L}_3(1)$. Later, we can extrapolate to $\mathcal{L}_3(1)$ in the thermodynamic limits and further to $\mathcal{L}_3(n)$.

The eigenenergies and eigenstates for $\mathcal{L}_3(1)$ and $\mathcal{L}_3(2)$ with finite size cells

We start from $\mathcal{L}_3(1)$ with 1 cell as shown in Fig. 2.9(a).

<center>(a)   （b）</center>
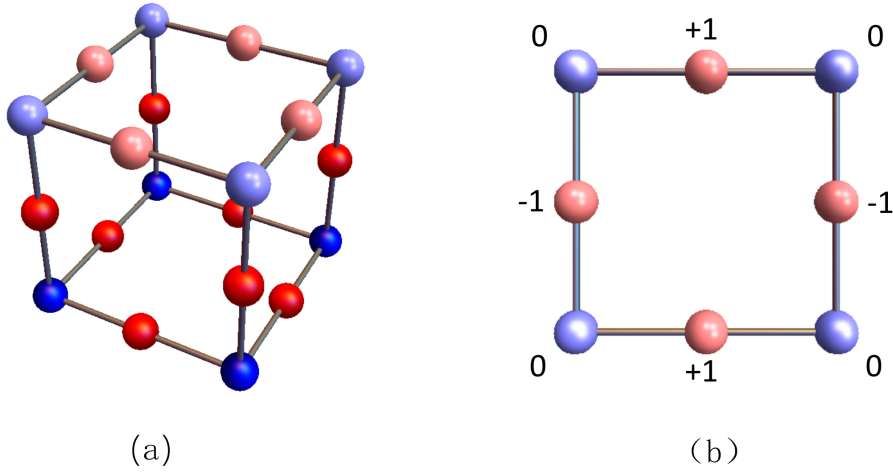
图 2.9: (a) Schematic of Lieb model $\mathcal{L}_3(1)$ with 1 cell, the upper layer with light red/blue atoms represents one 2D plaquette. (b) One plaquette from (a), is shown with the distribution of amplitudes for one eigenstate $E = 0$, and the amplitudes for all the rest atoms in (a) are zeros.

We obtain 5 eigenenergies $E = 0$ with hard boundary condition. We plot the distributions of amplitudes of one of these 5 eigenvectors in Fig. 2.9(b). We just show the upper layer cut from Fig. 2.10(a) in Fig. 2.9(b), since the amplitudes for all the rest atoms in Fig. 2.10(a) are zeros. Surprisingly, we find this distribution in Fig. 2.10(b) is exactly the same as $\mathcal{L}_2(1)$. Of course, the upper layer is not special, six sides are equivalent, .i.e, we find these 5 eigenstates are located at any one 2D plaquette of Fig. 2.9(a) or their superpositions.

Later, we go to $\mathcal{L}_3(1)$ with 8 cubes as displayed in Fig. 2.10(a), we get 28 eigenenergies $E = 0$ with hard boundary condition. The Fig. 2.10(b) and (c) are obtained from Fig. 2.10(a) as the same scheme as obtaining Fig. 2.9(b) from Fig. 2.9(a). Two of these eigenvectors are plot in Fig. 2.10(b) and (c), which is exactly the same as $\mathcal{L}_2(1)$ as well. Similarly, there are 9 sides in Fig. 2.10(a) that are the same as Fig. 2.10(b). we can easily generalize that these 28 eigenenergies $E = 0$ occupy any one 2D plaquette or their superpositions of these 9 sides of Fig. 2.10(a).
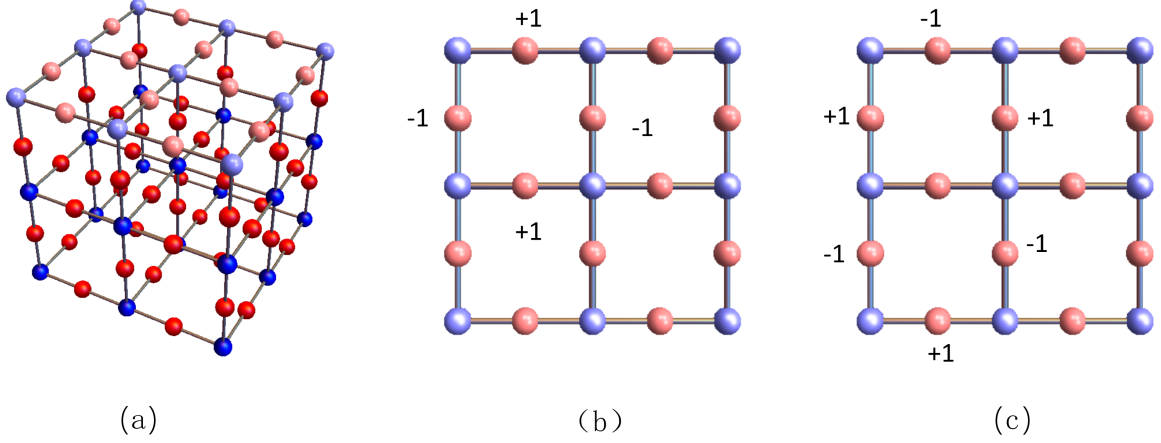
图 2.10: (a) Schematic of Lieb model $\mathcal{L}_3(1)$ with 8 cells. (b) and (c) are cuts from the upper layer of (a), which consisting 4 2D plaquettes. The distributions of amplitudes for two eigenstates $E = 0$ are shown in (b) and (c), and the amplitudes for all rest atoms with no numbers are zeros.

Then, we calculate the $\mathcal{L}_3(2)$ with 1 cube. We show two eigenstates for $E = -1$ and $E = 1$ at (b) and (c) respectively, since the amplitudes of these two eigenstates just occupy on one plaquette, leaving all the rest atoms with zero amplitudes. Similarly, the six sides equivalent. We found Fig. 2.11(b) and (c) are exactly the same as Fig. 2.5(a) and (b).

The deduction for $\mathcal{L}_3(n)$ and its CLS

Hence, up to here, we include that it's easily to extract the CLS for $\mathcal{L}_3(n)$ based on the $\mathcal{L}_2(n)$ – just pick one plaquette from $\mathcal{L}_3(n)$, which transfer $\mathcal{L}_3(n)$ to $\mathcal{L}_2(n)$, and repeat the steps as detailed in Fig. 2.8. By the way, there is a difference between $\mathcal{L}_3(n)$ and $\mathcal{L}_2(n)$. For any n, there are n double-degenerate flat bands for $\mathcal{L}_3(n)$ but only n one-degenerate flat bands for $\mathcal{L}_2(n)$. Thus, for any n, there exist $2n$-families of macroscopically degenerate compactly localized states (CLS), all of which have strictly non-zero amplitude in the Lieb sites enclosed within each 2D square plaquette of the lattice.

Since there are $3n + 1$ atoms in a unit cell for $\mathcal{L}_3(n)$, it posses a total of $3n + 1$ Bloch bands. In a cube cut-off of the lattice with N unit-cells per side each band posses a total of N^3 states. Such cube version of $\mathcal{L}_3(n)$ hence support $3N^3$ CLS – $i.e.$ as many as the number of 2D plaquettes in the cube. However, it easily follows that N^3 of these CLS are linear combination of the remaining compact states, yielding an irreducible number of $2N^3$ CLS at energy λ_j. These states consequently form two flat bands for the $\mathcal{L}_3(n)$ at $E = \lambda_j$ – or, equivalently, a double-counted flat band at $E = \lambda_j$.

Since there exist n eigenstate $\{v^i\}_{i=1}^n$ with energies $\lambda_i \neq \lambda_j$ for $i \neq j$ for the 1D chain
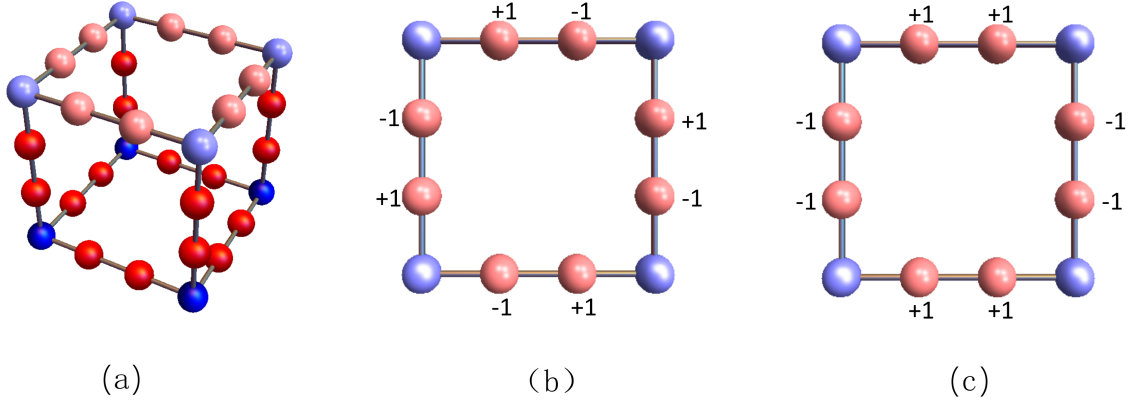
图 2.11: (a) Schematic of Lieb model $\mathcal{L}_3(2)$ with 1 cell. (b) and (c) are cuts from the upper layer of (a), shown with the distribution of amplitudes for eigenstates $E = -1$ and $E = 1$, and the amplitudes for all the rest atoms with no numbers are zeros.

of n Lieb sites, this construction can be done n times – generating n families of CLS for the lattice $\mathcal{L}_3(n)$, and therefore $2n$ flat bands $\{\lambda_i\}_{i=1}^n$ – or, equivalently, n double-degenerate flat bands. Hence, Fig. 2.7 shows the CLS for $\mathcal{L}_3(n)$ as well.

2.3 Transfer matrix method (TMM)

Transfer matrix method (TMM), as a numerical iterative technique to calculate localization length of disorder system, has been employed widely. This method have two benefits, first, it is not necessary to calculate wave functions, which could evade large size calculations; second, the accuracy is controlled and chosen before starting a calculation. The method considers electrons transferring, according to the single-particle, stationary Schrödinger equation of the system, along the quasi-1D bar(strip) with fixed transversal square(line) cross sections of $M^2(M)$ unit-cells via highly optimized matrix-vector calculations. One iteratively obtains estimates of the self-averaged localization length $\lambda_M(E,W)$, with the $\Lambda_M = \lambda_M(E,W)/M$ being the dimensionless, reduced localization length, where we can regard as the localization length in the unit of width M. The result is converging, if the error is within our tolerance after enough matrix-vector calculations, where enough means the number of electron transfers $\tilde{M}$, .i.e, the number of matrix-vector calculations in the longitudinal direction, is typically $\tilde{M} > 10^7$–10^9 such that $\tilde{M} \gg M$ along the bar(strip) [69, 70]. To make the explanation more concrete, we take the model $\mathcal{L}_2(1)$ as a example [68]. Starting point is the stationary Schröding equation $H\Psi = E\Psi$ in the wannier representation, where the Hamiltonian H is expressed as Equation 2.3. If we label the atom A, B and C in the dotted square (x,y), $(x-1,y)$ and $(x,y-1)$ as showed in Fig. 2.12, respectively. The wave function amplitude in the atoms A, B and
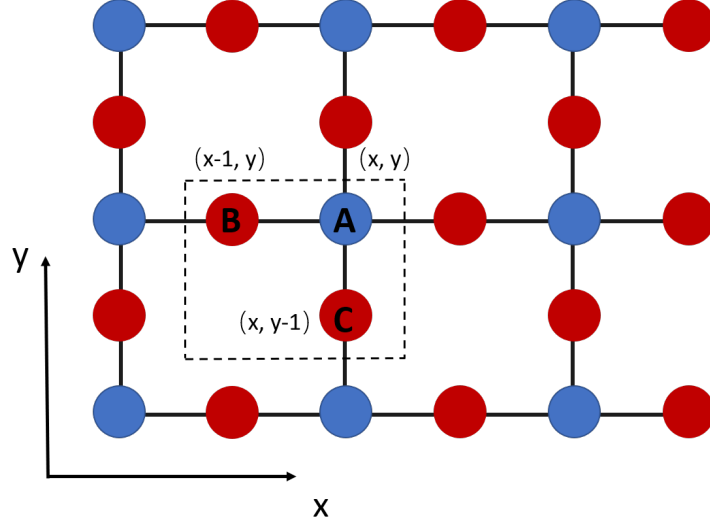
图 2.12: Schematic of Lieb model $\mathcal{L}_2(1)$. The atoms A, B and C labeled with coordinates in dotted square is a unit cell, the black lines are the hopping between neighbor atoms.

C follows the equations as below,

$$E\psi_{x,y}^A = \varepsilon_{x,y}\psi_{x,y}^A - t\psi_{x-1,y}^B - \psi_{x+1,y}^B - t\psi_{x,y-1}^C - t\psi_{x,y+1}^C \quad , \tag{2.6}$$

$$E\psi_{x,y}^B = \varepsilon_{x,y}\psi_{x,y}^B - t\psi_{x-1,y}^A - t\psi_{x+1,y}^A \quad , \tag{2.7}$$

$$E\psi_{x,y}^C = \varepsilon_{x,y}\psi_{x,y}^C - t\psi_{x,y-1}^A - t\psi_{x,y+1}^A \quad , \tag{2.8}$$

where the onsite potential energy $\varepsilon_{x,y}$ follows random and uniform distribution $\left[-\frac{W}{2}, \frac{W}{2}\right]$, t is the hopping strength, and E is the energy.

By replacing ψ^C with ψ^A, the equation 2.8 can be written as $\psi_{x,y}^C = (-t\psi_{x,y-1}^A - t\psi_{x,y+1}^A)/(E - \varepsilon_{x,y})$, and insetting this $\psi_{x,y}^C$ into equation 2.6, we obtain

$$\psi_{x+1,y}^B = (\frac{\varepsilon_{x,y} - E}{t} - \frac{t}{\varepsilon_{x,y-1} - E} - \frac{t}{\varepsilon_{x,y+1} - E})\psi_{x,y}^A - \frac{t}{\varepsilon_{x,y-1} - E}\psi_{x,y-2}^A - \frac{t}{\varepsilon_{x,y+1} - E}\psi_{x,y+2}^A$$
$$- \psi_{x-1,y}^B \quad . \tag{2.9}$$

Via writing it in the form of a matrix,

$$\begin{pmatrix} \Psi_{x+1,y}^B \\ \\ \Psi_{x,y}^A \end{pmatrix} = \begin{pmatrix} \frac{\varepsilon_{x,y}-E}{t} - (\frac{t}{\varepsilon_{x,y-1}-E} + \frac{t}{\varepsilon_{x,y+1}-E}) - \Pi_2(\frac{t}{\varepsilon_{x,y-1}-E} + \frac{t}{\varepsilon_{x,y+1}-E}) & -1 \\ \\ 1 & 0 \end{pmatrix} \begin{pmatrix} \Psi_{x,y}^A \\ \\ \Psi_{x-1,y}^B \end{pmatrix} , \tag{2.10}$$

where the Π_2 the hopping connection to neighboring A sites in the y-direction.

Then, by summing over y, .i.e for a special slice(a fix x), putting all amplitudes of A atoms in the matrix form, marked as ψ_x^A, we obtain the generalization of matrix equation 2.10, with $\mathbf{T}_{A\to B}$ labeling the transfer of wave vector amplitudes from sites A to sites B in the x-direction as below

$$
\begin{pmatrix} \psi_{x+1}^B \\ \\ \psi_x^A \end{pmatrix} = \mathbf{T}_{A\to B} \begin{pmatrix} \psi_x^A \\ \\ \psi_{x-1}^B \end{pmatrix}
$$

$$
= \begin{pmatrix} \left(\frac{\varepsilon_{x,y}-E}{t} - \frac{t}{\varepsilon_{x,y-1}-E} - \frac{t}{\varepsilon_{x,y+1}-E}\right)\mathbf{1}_M - \left(\frac{\mathbf{t}_y}{\varepsilon_{x,y-1}-E} + \frac{\mathbf{t}_y^\dagger}{\varepsilon_{x,y+1}-E}\right) & -\mathbf{1}_M \\ \\ \mathbf{1}_M & \mathbf{0}_M \end{pmatrix} \begin{pmatrix} \psi_x^A \\ \\ \psi_{x-1}^B \end{pmatrix} ,
$$

$$(2.11)$$

where $\mathbf{1}_M$ and $\mathbf{0}_M$ are the $M \times M$ identity and zero matrices, and $\mathbf{t}_y$ is a $M \times M$ matrix as the form

$$
\mathbf{t}_y = t \begin{pmatrix} 0 & 1 & 0 & \cdots & 0 & 0 \\ 0 & 0 & 1 & \cdots & 0 & 0 \\ \vdots & & \ddots & & & \vdots \\ 0 & 0 & 0 & \cdots & 1 & 0 \\ 0 & 0 & 0 & \cdots & 0 & 1 \\ (1) & 0 & 0 & \cdots & 0 & 0 \end{pmatrix} ,
$$

$$(2.12)$$

and $\mathbf{t}_y^\dagger$ is the complex conjugate form of $\mathbf{t}_y$. Hence the $\mathbf{t}_y$ and $\mathbf{t}_y^\dagger$ are the generalization of Π_2 and denote the connections to neighbouring A sites in y-direction as well. The (1) in the bottom left of matrix $\mathbf{t}_y$ represents the periodic boundary condition, and hard boundary condition if it's zero. In our derivation, to make sure that the transfter matrix has the form of $2M \times 2M$ size, the C sites have been effectively renormalized away into effective onsite energies and changed vertical hopping terms. The term $\frac{\varepsilon_{x,y}-E}{t}\mathbf{1}_M \equiv$ diag $\left(\frac{\varepsilon_{x,1}-E}{t}, \frac{\varepsilon_{x,2}-E}{t}, \ldots, \frac{\varepsilon_{x,M}-E}{t}\right)$ in the upper left of equation 2.11.

Following the same steps, the equation 2.7 can be written as follow,

$$
\begin{pmatrix} \Psi_{x+1}^A \\ \\ \Psi_x^B \end{pmatrix} = \mathbf{T}_{B\to A} \begin{pmatrix} \Psi_x^B \\ \\ \Psi_{x-1}^A \end{pmatrix} = \begin{pmatrix} \left(\frac{\varepsilon_{x,y}-E}{t}\right)\mathbf{1}_M & -\mathbf{1}_M \\ \\ \mathbf{1}_M & \mathbf{0}_M \end{pmatrix} \begin{pmatrix} \Psi_x^B \\ \\ \Psi_{x-1}^A \end{pmatrix} .
$$

$$(2.13)$$

In short, The TMM for $\mathcal{L}_2(1)$ can be expressed as follow. First, considering a quasi-1D strip of length $\tilde{M} \gg M$ as shown in Fig. 2.12, the propagation direction is along the x direction, where M and $\tilde{M}$ are the numbers of unit cell in y and x direction. Second, the transfer matrix process contains two different transfer matrices, T_{AB} and T_{BA} along the

x direction, .i.e, multiply these matrices $T_{AB}T_{BA}T_{AB}\ldots T_{BA}T_{AB}$ with an initial complete state $\Psi_x^A(1) = (1, 0, \ldots, 0)$, $\Psi_x^A(2) = (0, 1, \ldots, 0)$, ..., $\Psi_x^A(M) = (0, 0, \ldots, 1)$. Third, due to the numerical instabilities of transfer matrix method, which will lost the information of γ_{min}, we need reorthogonalize the M states at least after every $10th$ multiplication via Gram-Schmidt method [71], obtain the Lyapunov exponents γ_i, $i = 1, \ldots M$ and study their accumulated changes in variance until we reach a desired accuracy for the smallest γ_{min}, and then the localization length λ is obtained based on the $\lambda(M, E, W) = 1/\gamma_{min}$ [2, 72–74] for a given energy E and disorder strength W. Last, since the reduced localization length $\Lambda_M \equiv \lambda/M$ will be scaled in our finite size scaling, we need talk about the standard error of Λ_M, mark as $\Delta(\Lambda_M)$,

$$\Delta(\Lambda_M) = \Delta(\frac{\lambda}{M}) = \frac{1}{M}\Delta\lambda = \frac{1}{M}\Delta\frac{1}{\gamma_{min}} = \frac{1}{M}\frac{1}{\gamma_{min}^2}\Delta\gamma_{min} \quad . \tag{2.14}$$

For other extended $\mathcal{L}_2(n)$ and all $\mathcal{L}_3(n)$, as the basic idea is the same as $\mathcal{L}_2(1)$, we will not discuss in detail to avoid repeating. Please refer the paper of Mao [68, 69] for details.

2.4 Spectral statistic methods

2.4.1 Exact diagonalization and sparse matrix diagonalization methods

We firstly get the eigenenergy spectrum of disorder system via exact diagonalization method. However, the limit of computing source constrains us only to deal with small system size with exact diagonalization method. Normally for a system with N particles, the Harmiltonian matrix is a $N \times N$ matrix, and the exact diagonalization method gives us a spectrum with N eigenvalues and eigenstates. There is a routine called Jadamilu, who trades off the number of eigenvalues available and the calculable system size. This routine just focus on a given target value and obtain the closed eigenvalues of a given quantity in order to reach higher system size at the same machine condition. For instance, if we set the target energy and the number of eigenvalues to be calculated as E_t and n, where $n \ll N$, then the routine will return n eigenvalues closest to E_t and the calculable system size N' is much larger than N in the same machine condition. More detials can refere this article [75].

2.4.2 Spectral gap ratio statistic

Based on the random matrix theory (RMT), the energy level statistics(ELS) has been confirmed as a powerful tool to characterize the metal-insulator transition[3,31,50]. However, the unfolding procedure [76, 77] has to be considered in the ELS.

In 2007, a new statistic method, with the advantage of getting rid of unfolding as the independence of the local density of states, has been proposed by Oganesyan and Huse [78]. Considering a ascending energy spectrum $\{E_i\}$, the adjacent gap ratio is defined as

$$r_i = min(s_i, s_{i+1})/max(s_i, s_{i+1}) \tag{2.15}$$

with $s_i = E_i - E_{i-1}$. The r-values follow distribution $P(r)$ of the Gaussian orthogonal matrix ensemble(GOE) in the extended regime, while obey Poisson distribution in the localized regime as showed in Fig. 2.13. For the GOE distribution, the numerical mean value $\langle r \rangle = \int_0^1 rP(r)\mathrm{d}r = 0.5295$ [78]; the analytical surmise gives $\langle r \rangle_{Sur} = 4 - 2\sqrt{3} \approx 0.53590$ [79]. For the Poisson distribution, the mean value $\langle r \rangle_{Poi} = 2\ln 2 - 1 \approx 0.386$. The metal-insulator transition mapping to r-statistic becomes the rapid change of the mean value $\langle r \rangle$ from 0.5295 to 0.386. However, the shift is smooth in the actual calculation due to the finite size effect, and it trends to a vertical line as system size increase. As for the standard error of $< r >$, it's given by $\Delta(< r >) = \sqrt{([\langle r \rangle^2] - [\langle r \rangle]^2)/(R-1)}$, where $[\ ]$ denotes the average over R disorder potential realization, and $\langle \rangle$ represents the average within a given potential realization [78].

A more recent measure introduced in Refs. [80, 81] by defining a extended gap ratio

$$|z_i| = |E_i - E_{NN}|/|E_i - E_{NNN}| \quad , \tag{2.16}$$

with E_{NN} and E_{NNN} the nearest and the second-nearest eigenenergies to E_i, respectively. The distributions of $|z|$ and mean values $\langle |z| \rangle$ for extended and localized states are also shown in Fig. 2.13. The change of mean value $\langle |z| \rangle$ from $\langle |z| \rangle_{\text{ext}} = 0.5687(1)$ to $\langle |z| \rangle_{\text{loc}} = 0.5000(1)$ corresponds to the metal-insulator transition, where these values have been computed from 1000 independent random realization of 20000×20000 matrices for GOE and 1000 realization of random diagonals with 20000 entries in our paper [82], respectively. The calculations also yield $\langle r \rangle_{\text{GOE}} = 0.5307(1)$ which is in excellent agreement with the best fit value obtained by Atas et al. [79] for $\langle r \rangle_{\text{Sur}}$.

2.4.3   The participation number P and inverse participation Ratio(IPR)

The r-statistic and z-statistic introduced above are the spectral statistic methods. Next, we present a measurement method based on the eigenstates. Starting from the Schröding equation

$$H\Psi_i = E_i\Psi_i \quad , \tag{2.17}$$

where E_i and Ψ_i are the eigenvalue and eigenstate. Expanding the eigenstate Ψ_i based on Wannier basis $|j\rangle$ as below,

$$\Psi_i = \sum_j \psi_j^{(i)}|j\rangle \quad , \tag{2.18}$$
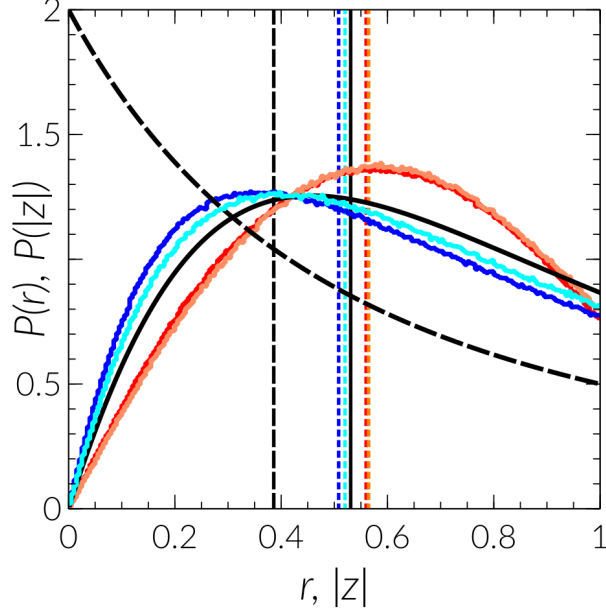
图 2.13: Distributions of the energy level ratios r (dark and light blue) and $|z|$ (dark and light red) for a $d = 3$ Lieb model with 44^3 sites (Liu et al., 2020) and averaged over $\sim 8 \times 10^6$ ratios for each curve. Darker colors denote slightly larger disorders. The black dashed and solid lines denote the exact $P_{Poisson}(r)$ and a surmise for $P_{GOE}(r)$. No such predictions are yet known for $P(|z|)$ (Luo et al., 2021). The vertical dashed/solid lines are the corresponding mean values, $< r >$ for exact $P_{Poisson}(r)$ (black dashed), $< r >$ for a surmise of $P_{GOE}(r)$ (black solid), $< r >$ for numerical results (dark/light blue) and $< |z| >$ for numerical results (dark/light red). The figure is quoted from the literature [83].

where the $\psi_j^{(i)}$ is the amplitude of eigenstate Ψ_i projected on site j. By introducing a quantity, namely participation number P, the inverse participation ratio(IPR) [84] is be defined as

$$IPR = 1/P(E_i) = \sum_j |\psi_j^{(i)}|^4 \quad , \tag{2.19}$$

and we can distinguish the extended states from localized states in term of the value IPR or P. First, let us consider the P as the measurement. For the extended states, as the states spread through the whole system(assuming system size is N), the probability to find state Ψ_i in lattice position j is $|\psi_j^{(i)}|^2 \sim \frac{1}{N}$, the value P gives

$$1/P(E_i) = \sum_j |\psi_j^{(i)}|^4 = \sum_j (\frac{1}{N})^2 = \frac{N}{N^2} = \frac{1}{N} \quad , \tag{2.20}$$

.i.e $P(E_i) \sim N$ for the extended state. For localized states, the $|\psi_j|^2$ is a finite number (between(0,1]) in the localized regime (assuming the size of localized regime is M, with $0 < M \ll N$), while is zero outside the localized regime. Thus, we can get $P(E_i) \sim M$ for the localized state. Intuitively, the participation number P is the number of positions

the state can occupied; it is N for extended state as it can occupy the whole system while finite number M for localized state as it localized in a small regime. Specially for $M = 1$, the state is localized at an isolated point.

In practice, the IPR is a good measurement to distinguish localized states from extended states for a large enough system, as $IPR \sim 0$ for extended states while $0 < IPR \leq 1$ for localized states.

2.5   Numerical scaling analysis

2.5.1   The scaling before 1999

According to the one-parameter scaling theory detailed in Sec. 1.1.4, the critical behavior can be described by a divergent correlation length of infinite system

$$\xi_\infty(W) \sim |W - W_c|^{-\nu} \quad , \tag{2.21}$$

where W_c and ν are the critical disorder and critical exponent, respectively. The presence of universality of critical exponent is a solid foundation for single parameter scaling. In order to test the validity of one-parameter scaling theory, the numerical verification of critical exponent is the main work of the theory of Anderson localization.

Phase transitions occur only in the thermodynamic limits, while only finite system size can be obtained in our actual simulation. In order to resolve this contradiction, we have to employ the scaling laws

$$X(W', bL) = F(X(W', L), b) \quad , \tag{2.22}$$

where X denotes the finite-size data and is a dimensionless vector, b is the scale factor and W' is the composite parameter, which containing disorder W and energy E. Via making a approximation, namely assuming the behavior of X under the changes of length scale $L' \to bL$ depends on X alone, and not on L or W'. Then the equation (2.22) can be written as the form below,

$$\frac{\mathrm{d}\ln X}{\mathrm{d}\ln L} = \chi(X) \quad , \tag{2.23}$$

after integrating equation 2.23 we get

$$X(L, W') = f(L/\xi_\infty(W')) \quad , \tag{2.24}$$

where the $\xi_\infty(W')$ is the correlated length of infinite system, and dependent only on the W' but not on L. All data with different size L can be scaled on the scaling function f through being scaled by $\xi_\infty(W')$.

In the numerical simulation of transfer matrix method, we take the strip/bar width M as the system size L, W instead of W' for convenience, and the reduced localization length $\Lambda(M, W)$ as $X(L, W')$, .i.e

$$X(L, W') = \Lambda(M, W) = \Lambda_M(W) = \lambda_M(W)/M \quad , \qquad (2.25)$$

where λ_M is the localization length. Hence, the scaling function of reduced localization length Λ_M can be written as below,

$$\Lambda_M(W) = f(M/\xi_\infty(W)) \quad . \qquad (2.26)$$

As we calculated the Λ_M with TMM, what we need is to perform the procedure based on a least squares method introduced in ref. [70] to fit parameter $\xi_\infty(W)$ in equation 2.26. In principle, we can fit the data with obtained $\xi_\infty(W)$ to extract critical exponent ν according to equation 2.21. However, the presence of the round error of the singularity in $\xi_\infty(W)$ at critical point seemingly results in systematic errors, which implies it can only give a low precision result of ν.

Of course, we can also avoid to fit the correlation function, and turn to fit the data Λ directly. If we expand the function $f(x)$ and keep the first two terms, $f(x) = f(0) + Cx^\alpha$, then replace x by $M/\xi_\infty \sim M|W - W_c|^\nu$ in terms of Eq. 2.21. We obtain $f(M/\xi_\infty) = f(W_c) + CM^\alpha|W - W_c|^{\alpha\nu} = f(W_c) + CM^{1/\nu}|W - W_c|$, with $\alpha = 1/\nu$. Similar, expanding Eq. 2.26 in the critical point W_c and keep linear terms,

$$\Lambda(M, W) = \Lambda_c + A(W - W_c)M^{1/\nu} \quad , \qquad (2.27)$$

where $\Lambda_c = \Lambda(W = W_c)$ doesn't depend on the system size M. The critical disorder W_c and critical exponent ν can be estimated by fitting data according to this equation. However, as only the linear terms are considered, it restricts the data to a small range of critical disorder W_c.

With the improvement of computing performance, the data with larger system size can be obtained, and showed a systematic shift of the crossing point [85], which hadn't been presented before as the low precision. The problem made the one-parameter scaling in trouble. In actual, the exponent ν in Eq. 2.21 contains two groups, namely relevant and irrelevant in terms of the $v < 0$ or $v > 0$ [2], which corresponding to the direction of flow is away from the fixed point or towards it in renormalization group space. The variables in irrelevant part are dependent on system size M, and play a import role in finite system; they determine how Λ depends on various microscopic details of models, such as correlation length, the distribution of disorder, etc. The one-parameter scaling assumption requires the irrelevant variables η to manifest as the form

$$\eta(M) \sim M^{-y} \quad , \qquad (2.28)$$

which can be ignored in the thermodynamic limit of $M \to \infty$, and y is the irrelevant exponent.

In 1999, Slevin and Ohtsuki proposed a method [6] based on the ideal to solve this problem, and this method so far has been widely adopted. In the next section, we will focus on this approach.

2.5.2   Finite size scaling method

In their work, the main improvements are the inclusion of two kinds of corrections to scaling, namely irrelevant scaling variable and nonlinearities of the disorder dependence of the scaling variables. Based on the renormalization group equation, they consider a dimensionless quantity $\Lambda = \lambda/M$ as a function of scaling variables,

$$\Lambda = f(M/b, \chi_r b^{1/\nu}, \chi_i b^y) \quad , \tag{2.29}$$

where b and M are the sale factor and strip/bar width as before, χ_r and χ_i are relevant and irrelevant scaling variables, and ν and y are the corresponding critical exponents, respectively. The irrelevant variable χ_i requires $y < 0$. By setting the length scale $b = M$, it gives

$$\Lambda = F(\chi_r M^{1/\nu}, \chi_i M^y) \quad , \tag{2.30}$$

where function F is dependent on f. It is reasonable to assume that F can be Taylor expanded according the irrelevant scaling variable as F is smooth function in finite M,

$$\Lambda = \sum_{n=0}^{n_I} \chi_i^n M^{ny} F_n(\chi_r M^{1/\nu}) \quad , \tag{2.31}$$

where function F_n is dependent on relevant variable χ_r but not on irrelevant variable χ_i. For the term of $n = 0$, F_0 recovers to the traditional scaling behavior, which doesn't consider the irrelevant scaling variable and nonlinearities. For the terms of $n > 0$, as the existence of factor $\chi_i^n M^{ny}$, it represents that the effects of irrelevant scaling variable is considered. If we expand the function F_n in terms of the relevant scaling variable χ_r even further, we have

$$F_n(\chi_r M^{1/\nu}) = \sum_{m=0}^{n_R} \chi_r^m M^{m/\nu} F_{nm} \quad . \tag{2.32}$$

The nonlinearities are accounted by expanding the scaling variables χ_r and χ_i according to dimensionless disorder $w = (W_c - W)/W_c$ like below,

$$\chi_r(w) = \sum_{n=1}^{m_R} b_n w^n \quad , \qquad \chi_i(w) = \sum_{n=0}^{m_I} c_n w^n \quad , \tag{2.33}$$

where W_c is the critical disorder, and $|w|$ is a measure of near the critical disorder. The smaller the value $|w|$ is, the closer to critical disorder W_c it is. In order to fix the absolute scale, we set $b_1 = c_0 = 1$.

Once setting $n_R = 1$, $m_R = 1$, $n_I = 0$, and $m_I = 0$, we recover to the case of Eq. 2.27, which getting rid of the consideration of nonliearities and irrelevant terms that depend on system size. To fit the data in a larger W ranges, we can consider the nonlinearities and set the $n_R \geq 2$ and $m_R \geq 2$ to appropriate fit functions. In the fitting procedure, the number of fitting parameters is given by $N_p = (n_I + 1)(m_R + 1) + m_R + m_I + 2$.

We can clearly see the nature of the correction terms caused by irrelevant parameter($\chi_i > 0$) by rewriting equation 2.31 as the form below,

$$\Lambda = F_0(\chi_r M^{1/\nu}) + \sum_{n=1}^{n_I} \chi_i^n M^{ny} F_1(\chi_r M^{1/\nu}) \quad , \tag{2.34}$$

there is a systematic shift caused by finite system size, which will disappear when M is large enough as irrelevant exponent $y < 0$. The scaling behavior requires to subtract the correction terms coming from irrelevant variable,

$$\Lambda_{corrected} = \Lambda - \sum_{n=1}^{n_I} \chi_i^n M^{ny} F_1(\chi_r M^{1/\nu}) \quad . \tag{2.35}$$

The corrected term has the form

$$\Lambda_{corrected} = F_\pm(M/\xi_\infty) \quad , \tag{2.36}$$

with correlation length behaving as

$$\xi_\infty = \xi_\pm |\chi_r|^{-\nu} \quad , \tag{2.37}$$

where functions $F_\pm(x) = F_0[\pm(\xi_\pm x)^{1/\nu}]$, and $\xi_\pm$ is constant. In the real simulation, we don't have to determine the constant $\xi_\pm$ in order to extract the critical parameter W_c and ν and we can simply set $\xi_\pm = 1$. By the way, in the case of getting rid of irrelevant variable χ_i, we don't need to take system size dependent correction term under consideration, and we have $\Lambda = F_\pm(M/\xi)$.

Once replacing parameter χ_r in equation 2.37 with nonlinear expansion equation 2.33, we obtain a complicated form of correlation length, which is totally different with equation 2.21. However, if we ignore the nonlinearity, .i.e, setting $m_R = 1$ and $m_I = 0$, the relevant parameter χ_r has the form $\chi_r \sim w$; after inserting it into equation 2.37, the correlation length is in a simple power law form $\xi_\infty \sim |w|^{-\nu}$, which is exactly the same as the form of equation 2.21.

The function F_n, critical exponent ν and irrelevant exponent y are expected to be universal, but the expansion coefficients $\{b_n\}$ and $\{c_n\}$ are not.

2.5.3   The non-linear fitting procedure

The nonlinear fitting procedure is used to fit the data based on equation 2.30, 2.31 and 2.32 via *Mathematica.* According to minimizing the χ^2 statistics, which measuring the deviation between model Λ_{fit} and data Λ_i,

$$\chi^2 = \sum_{i=1}^{N_d} \frac{(\Lambda_i - \Lambda_{fit}(a_{00}, \ldots, a_{n_i n_r}, b_2, \ldots, b_{m_r}, c_1, \ldots, c_{m_i}, W_c, \nu, y))^2}{\sigma_i^2} \quad , \qquad (2.38)$$

where σ_i is the error of the corresponding data Λ_i, we can obtain the parameters with their confidence intervals in model Λ_{fit}, such as W_c, ν, and y. We use goodness-of-fit Q [86] to judge the quality of fit, it is defined as

$$Q = \Gamma_Q(\frac{N_d - N_p}{2}, \frac{\chi^2}{2}) \quad , \qquad (2.39)$$

where Γ_Q is the incomplete gamma function, N_d and N_p are the numbers of data and parameters, respectively. The real number Q is in the interval $[0, 1]$, where $Q > 0.01$ indicates a acceptable fit [86], and $Q = 1$ shows a perfect fit to data, which may result in over-fitting. The goodness-of-fit $Q = 0.5$, corresponding to $N_d - N_p = \chi^2$, means a good fit [86]. In our simulations, we regard the fits of $0.05 < Q < 0.95$ as the candidates, which is neither over-fitting nor under-fitting.

Chapter3 Disorder effects in the two-dimensional Lieb lattice and its extensions

3.1 Introduction

Flat energy bands have recently received renewed attention due to much experimental progress in the last decade [87]. Systems that exhibit flat-band physics correspond usually to specially "engineered" lattice structures such as quasi-1D lattices [22,88,89], diamond-type lattices [25], and so-called Lieb lattices, [27, 47, 90–93]. Indeed, the Lieb lattice, a two-dimensional (2D) extension of a simple cubic lattice, was the first where the flat band structure was recognized and used to enhance magnetic effects in model studies [12, 41, 42]. What's more, the dirac cone is also a bright spot. Actually, the CuO_2 plane of cuprate superconductors is also a Lieb lattice, and its flat band is conjectured that it would be relevant with the origin of high-temperature superconductivity [47–49]. Many theoretical and experimental works based on the Lieb model are exported as detailed in the introduction part.

In this work, we employ the Anderson model based on two-dimensional Lieb lattice and its extensions, and investigate how the localization properties in the neighboring dispersive bands are changed by the disorder [68]. We find that the whole states in the Lieb lattice and its extensions are localized for $W \leq 1$. Our results indicate that the finite-size scaled localization lengths ξ for the energies corresponding to flat bands in the clean system ($W = 0$) show a behaviour reminiscent of perturbative result for 1D. This could potentially provide spatial information about the nature of these localized states. For energies corresponding to dispersive bands in the clean system there is a tendency towards much larger localization lengths as is expected from the 2D Anderson model of localization [94].

3.2 Models

We consider a parametric family of two-dimensional Lieb lattices $\mathcal{L}_2(n)$, $n = 1, 2, 3, 4$ and the schemes are shown in Fig. 2.1. The Hamiltonian gives as

$$H = \sum_{\vec{r}} \varepsilon_{\vec{r}} |\vec{r}\rangle \langle \vec{r}| - \sum_{\vec{r} \neq \vec{r}\prime} t_{\vec{r}\vec{r}\prime} |\vec{r}\rangle \langle \vec{r}\prime| \ , \tag{3.1}$$

where the set of $|\vec{r}\rangle$ indicates the orthonormal Wannier states corresponding to electrons located at sites $\vec{r} = (x, y)$ of the Lieb lattice $\mathcal{L}_2(n)$ and $\varepsilon_{\vec{r}}$ is the onsite potential [68], which follows uniformly distribution with disorder strength W, .i.e, $[-W/2, W/2]$. As usual, we set the hopping integrals $t_{\vec{r}, \vec{r}\prime} \equiv 1$ for nearest-neighbor sites $\vec{r}$ and $\vec{r}\prime$ as energy scale and $t_{\vec{r}, \vec{r}\prime} \equiv 0$ otherwise.

3.3   Results

3.3.1   Dispersion relations and DOS
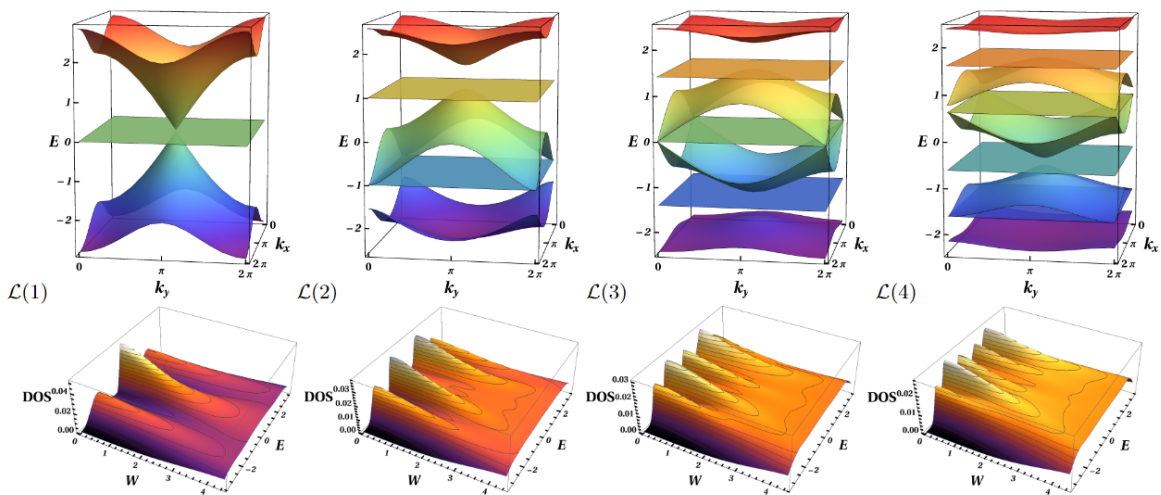
图 3.1: The band structure (top row) and the smoothed and normalized density of states (DOS, bottom row) for $\mathcal{L}_2(1)$ with width $M = 13$, $\mathcal{L}_2(2)$ with $M = 10$, $\mathcal{L}_2(3)$ with $M = 9$ and $\mathcal{L}_2(4)$ with $M = 8$. Colours in the top row vary from purple at low energies to red at high energies. In the bottom row, the colour indicates the numerical values of the DOS and the thin black lines are equal-DOS contours.

Before including disorder, we calculate the dispersion relations based on tight-binding method for $\mathcal{L}_2(n)$ ($n = 1, 2, 3, 4$), which are summarized in Tab. 3.1. Just to make it more intuitive, we plot the dispersion relations in Fig. 3.1, apparently there are n flat bands separated by $n + 1$ dispersive bands [95] for $\mathcal{L}_2(n)$. What's more, there are Dirac cones touching with flat band in special points in the (k_x, k_y) plane for $\mathcal{L}_2(1)$ and $\mathcal{L}_2(3)$ but no for $\mathcal{L}_2(2)$ and $\mathcal{L}_2(4)$.

After turning on disorder, we take a new quantity – disorder-dependent density of states(DOS) to measure the energy spectrum in stead of dispersion relations because of the lack of spatial translation symmetry. For the flat bands, the kinetic energy is zero and the potential energy becomes prominent, which is dominant by random disorder W.

	The number of atoms in a unit cell	The number of flat bands	dispersion relations	
$\mathcal{L}_2(1)$	3	1	$E_1 = 0$ $E_{2,3} = \pm\sqrt{4+2q}$	$q = \cos k_x + \cos k_y$
$\mathcal{L}_2(2)$	5	2	$E_{1,2} = \pm 1$ $E_3 = \rho_+ + \rho_-$ $E_4 = \omega\rho_+ + \omega^2\rho_-$ $E_5 = \omega\rho_- + \omega^2\rho_+$	$\omega = \frac{-1+\sqrt{3}i}{2}$ $\rho_\pm = \sqrt[3]{q \pm \sqrt{q^2 - \left(\frac{5}{3}\right)^3}}$
$\mathcal{L}_2(3)$	7	3	$E_1 = 0$ $E_{2,3} = \pm\sqrt{2}$ $E_{4,5,6,7} = \pm\sqrt{3 \pm \sqrt{5+2q}}$	
$\mathcal{L}_2(4)$	9	4	$E_{1,2,3,4} = \frac{1}{2}\left(\pm 1 \pm \sqrt{5}\right)$ $E_{5,6,7,8,9} \rightarrow E^5 - 7E^3 + 9E - 2q = 0$	

表 3.1: Dispersion relations for $\mathcal{L}_2(n)$, $n = 1, 2, 3, 4$. Need to mention, we have chosen the unit length in real space to be 1, and k_x, k_y are the wave vectors in the reciprocal space. Even though the $E_{4,5}$ of $\mathcal{L}_2(2)$ looks like it has an imaginary part, the $E_{4,5}$ actually are real roots as ρ_+ and ρ_- are complex conjugates of each other and the same as ω and ω^2.

Hence, small disorder can lift the high-degenerated flat bands and make the states in flat bands merge in neighbor dispersive bands. To search the interplay of flat bands and dispersive bands in disorder systems, we have calculated disorder-dependent DOS via exact diagonalization over 300 samples, where the system size M^2 are from $13^2, 10^2, 9^2$ to 8^2 for $\mathcal{L}_2(1)$, $\mathcal{L}_2(2)$, $\mathcal{L}_2(3)$ and $\mathcal{L}_2(4)$, respectively. After applying a Gaussian broadening to obtain a smoother a DOS, results are showed in the bottom line of Fig. 3.1. In a word, when the disorder W increased to the order of $2-3$, the DOS loses it's peak features.

3.3.2 Localization and finite size scaling

As there are flat bands in $E = 0$ for $\mathcal{L}_2(1)$ and $\mathcal{L}_2(3)$ but no for $\mathcal{L}_2(2)$ and $\mathcal{L}_2(4)$. We focus on energy $E = 0$ for all models $\mathcal{L}_2(n)$, which allow us to distinguish directly the localization properties between original flat bands($\mathcal{L}_2(1)$ and $\mathcal{L}_2(3)$) and original dispersive bands($\mathcal{L}_2(2)$ and $\mathcal{L}_2(4)$) under the effects of disorder. We have calculated the reduced localization length $\Lambda_M(E, W)$ at $E = 0$ via transfer matrix method, .i.e $\Lambda_M(0, W)$, for $\mathcal{L}_2(n)$, $n = 1, 2, 3, 4$ and shown them in Fig. 3.2. The transverse widths of slice are $M = 10, 12, \ldots, 20$ with error 0.1% for $\mathcal{L}_2(1)$, and $M = 10, 12, \ldots, 22$ with error 0.2% for $\mathcal{L}_2(2)$, $\mathcal{L}_2(3)$ and $\mathcal{L}_2(4)$. In Fig. 3.2, the $\Lambda_M(0, W)$ as a function of $1/M$ have been shown in the insets, we find all the $\Lambda_M(0, W)$ decrease with increasing M for
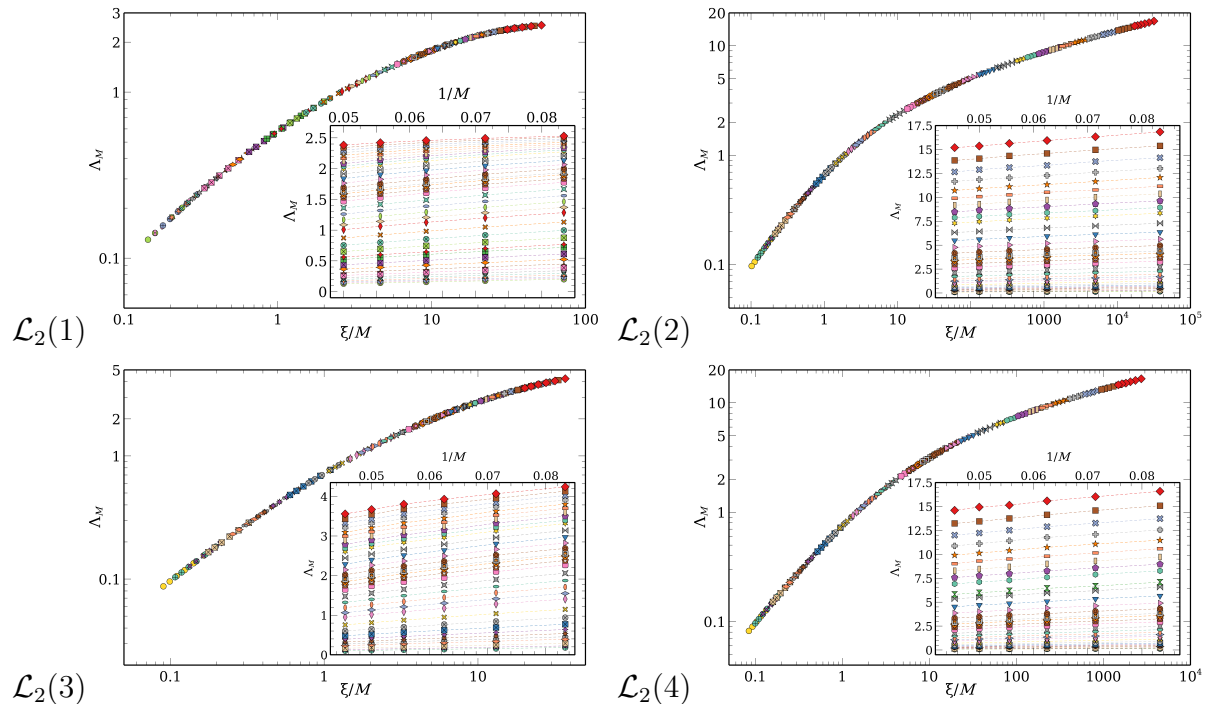
图 3.2: Double logarithmic plot of scaled reduced localization length, Λ_M, as a function of ξ/M for $\mathcal{L}_2(1)$, $\mathcal{L}_2(2)$, $\mathcal{L}_2(3)$ and $\mathcal{L}_2(4)$ as indicated. The chosen values for W are 1.0 ($\diamond$), 1.01, ..., 1.05 ($\square$), ..., 2.0, 2.1, 2.2, 2.4, 2.6 ..., 10.0 ($\bigcirc$) and vary in color. Some data points are not shown with symbols for clarity. Error bars are within symbol size. Insets: Λ_M as a function of $1/M$ for each $\mathcal{L}_2(n)$, respectively. Symbols and colors are as in the main panels, dashed lines are guides to the eye only.

orginal flat band and dispersive band, which imply these are localized states where for sufficiently large W and M, the values of λ_M saturate such that Λ_M, which is defined as λ_M/M, decreases when M increases.

Furthermore, we have also plotted the $\Lambda_M(0, W)$ as a function of ξ/M in the form of double logarithmic in main panels. The data Λ_M can be scaled on single scaling curve, which also decrease with increasing M, hence is consistent with previous results. What's more, for $\lambda_M \ll M$, .i.e $\Lambda_M \ll 1$, we note the linear behavior $\Lambda_M \sim 1/M$, where strong localization with $\lambda_M \sim \lambda_\infty$ is expected. Besides, we observe the localization lengths of states rooting in original flat bands are about one order of magnitude smaller than that rooting in original dispersive bands. This is indeed an acceptable outcome as the states in flat bands are absence of kinetic energy, and hence they become strong localization after introducing disorder.

Next, we give the plots of scaling parameters $\xi(0, W)$ as a function of disorder W in Fig. 3.3. Thouless [70, 96] claims that $\xi(W) \sim W^{-2}$ are expected for small disorder in a strictly 1D disordered chain, while a non-universal behaviour $\xi(W) = a/W^\alpha \exp(\beta W^{-\gamma})$

are expected for the weakly disordered 2D systems, where a, β are positive and α, γ are of order unity [2]. These fits are given in Fig. 3.3 as well, the details of fitting parameters are listed in Tab. 3.2. The fits of flat bands($\mathcal{L}_2(1)$, $\mathcal{L}_2(3)$) and dispersive bands($\mathcal{L}_2(2)$, $\mathcal{L}_2(4)$) are obviously different. The simple power-law fit $\xi(W) \sim W^{-2}$ seems to work well at $1 < W < 2$ for flat bands, while not for dispersive bands. For more details, we can see that our fitting results are not perfect. The efficient a is neither 105 at $E = 0$ [97] for fitting with $\alpha = 2$ in 1D, nor $12M$ [98] in quasi-1D stripes of width M. Further more, it's obvious that the magnitude of the ξ for $\mathcal{L}_2(2)$ and $\mathcal{L}_2(4)$ are near three order of magnitude above that for $\mathcal{L}_2(1)$ and $\mathcal{L}_2(3)$ for weak disorder. The lack of a simple fit to ξ in small disorder is reasonable as the disorder Lieb models $\mathcal{L}_2(n)$ are indeed different in localization behaviour from the standard 2D Anderson model.

3.4   Conclusions

We have studied the localization properties of the disordered 2D Lieb lattice and its extensions with exact diagonalization method and transfer matrix method in this paper. We found the significance of DOS peaks originating from flat bands are quickly destroyed by disorder. Via finit-size scaling, we find there are indeed different localization properties for energies corresponding to flat bands from that to dispersive bands. Nevertheless, all states are localized for disorder as low as 1.

fit function	parameter	estimates	p-value
$\mathcal{L}_2(1)$			
$aW^{-\alpha}$	a	619.1(2)	$< 10^{-10}$
	α	2.0816(7)	$< 10^{-10}$
$aW^{-2}e^{\beta W^{-1}}$	a	553(1)	$< 10^{-10}$
	β	0.117(2)	$< 10^{-10}$
$\mathcal{L}_2(2)$			
$aW^{-\alpha}$	a	310000(6000)	$< 10^{-10}$
	α	9.20(4)	$< 10^{-10}$
$aW^{-\alpha}e^{\beta W^{-\gamma}}$	a	118(2000)	0.94
	α	5(5)	0.26
	β	8(14)	0.56
	γ	0.7(7)	0.27
$aW^{-2}e^{\beta W^{-1}}$	a	14.2(5)	$< 10^{-10}$
	β	10.39(5)	$< 10^{-10}$
$\mathcal{L}_2(3)$			
$aW^{-\alpha}$	a	444.1(3)	$< 10^{-10}$
	α	2.206(2)	$< 10^{-10}$
$aW^{-2}e^{\beta W^{-1}}$	a	334.9(6)	$< 10^{-10}$
	β	0.292(3)	$< 10^{-10}$
$\mathcal{L}_2(4)$			
$aW^{-\alpha}$	a	21600(800)	$< 10^{-10}$
	α	7.33(7)	$< 10^{-10}$
$aW^{\alpha}e^{\beta W^{-\gamma}}$	a	9(101)	0.92
	α	3(5)	0.42
	β	8(11)	0.45
	γ	0.8(6)	0.16
$aW^{-2}e^{\beta W^{-1}}$	a	11.5(2)	$< 10^{-10}$
	β	7.96(3)	$< 10^{-10}$

表 3.2: Fit functions for $\xi(W)$ and lattices $\mathcal{L}_2(1)$, $\mathcal{L}_2(2)$, $\mathcal{L}_2(3)$ and $\mathcal{L}_2(4)$ with a, α, β, γ are fit coefficients estimated from a Levenberg-Marquardt non-linear fitting procedure.
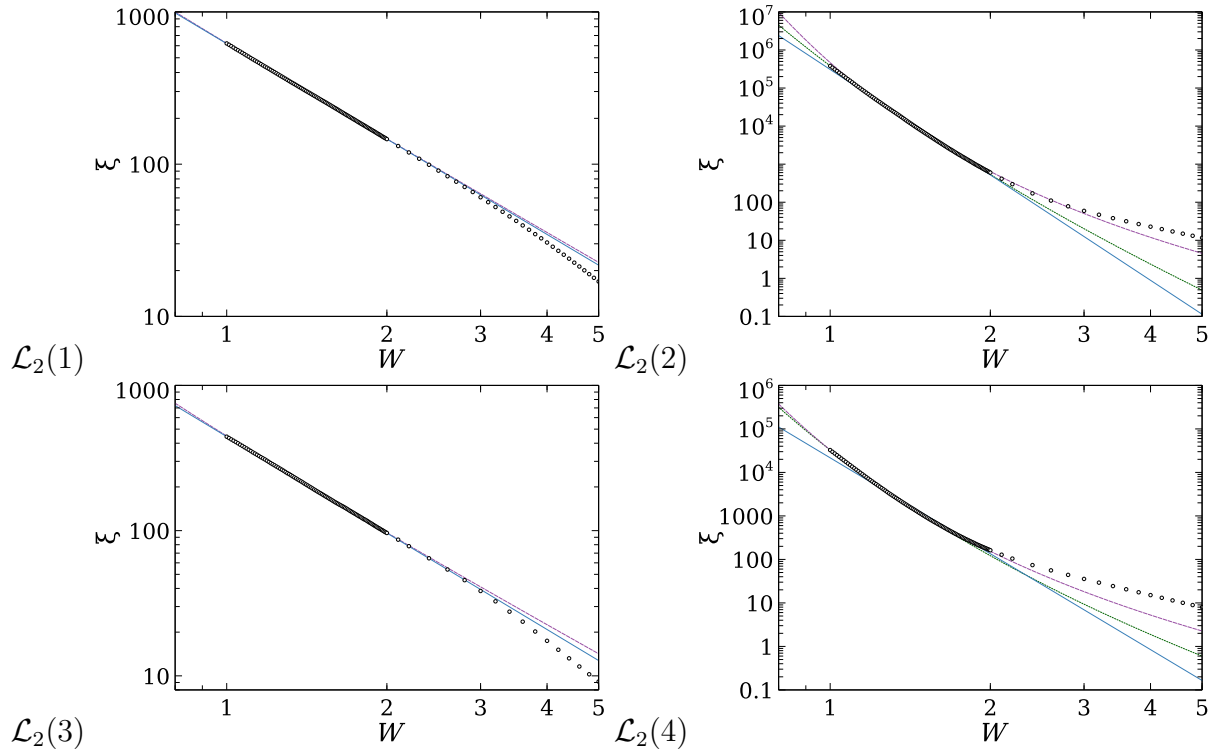
图 3.3: The scaling parameter $\xi(0, W)$ ($\bullet$) and fitted functional forms (lines) for $\mathcal{L}_2(1)$, $\mathcal{L}_2(2)$, $\mathcal{L}_2(3)$ and $\mathcal{L}_2(4)$, respectively. The blue solid line corresponds to $aW^{-\alpha}$, the purple dashed line is the fit function $aW^{-2}e^{\beta W^{-1}}$, while the green dotted line is the fit function $aW^{-\alpha}e^{\beta W^{-\gamma}}$. The values for a, α, β and γ are chosen from Tab. 3.2.

Chapter4 Localization, phases, and transitions in the three-dimensional extended Lieb lattices

4.1 Introduction

The phenomenon of wave localization in disordered lattices has attracted a lot of attention in the condensed-matter community since it was first predicated in 1958 [1]. Later, Abrahams et al. predicts there are no metal-insulator transition in the one and two dimensional single particle systems without magnetic field, and spin-orbit coupling [7]. Indeed, our work detailed in previous chapter shows that in two-dimensional Lieb model and its extensions all states are localized for $W > 1$. Nevertheless, there are more abundant phases in three dimensions, what role does the flat band play in it, and what kind of novel phenomena it causes is a very significant topic. Less attention has been given to 3D flat-band systems [25] or extended Lieb lattices [68, 93]. Furthermore, while disorder in quasi-1D [10, 21, 24, 99] and 2D [100] has previously received some attention, comparatively little work has investigated the influence of disorder on 3D flat-band systems [26, 88, 101]. Our work introduced in this chapter will fill the gap.

In the work, we extend our previous studies of Lieb lattices to the class of 3D Lieb lattices and its extensions. As is well known [2] the Anderson transition in a simple cubic lattice with uniform potential disorder $\epsilon_{\vec{x}} \in [-W/2, W/2]$ at each site $\vec{x}$ is characterized by a critical disorder $W_c = 16.0(5)t$ [102], with t denoting the nearest neighbor hopping strength. The full energy-disorder phase diagram is characterized by a simple-connected region of extended states ranging from $\pm 6t$ at $W = 0$ and ending at $W_c = 16.530(16.524, 16.536)$ for $E = 0$ [103]. The critical exponent of the transition has been determined with ever greater precision as close to, e.g., $\nu = 1.590(1.579, 1.602)$ [103] and $1.57(2)$ [6].

4.2 Models

We consider a parametric family of three-dimensional Lieb lattices $\mathcal{L}_3(n)$, $n = 1, 2, 3, 4$ and the schemes are shown in Fig. 2.1. The Hamiltonian gives as

$$H = \sum_{\vec{r}} \varepsilon_{\vec{r}} |\vec{r}\rangle\langle\vec{r}| - \sum_{\vec{r} \neq \vec{r}\prime} t_{\vec{r}\vec{r}\prime} |\vec{r}\rangle\langle\vec{r}\prime| \ , \tag{4.1}$$

where the set of $|\vec{r}\rangle$ indicates the orthonormal Wannier states corresponding to electrons located at sites $\vec{r} = (x, y, z)$ of the Lieb lattice $\mathcal{L}_3(n)$ and $\varepsilon_{\vec{r}}$ is the onsite potential [68], which follows uniformly distribution with disorder strength W, .i.e, $[-W/2, W/2]$. As usual, we set the hopping integrals $t_{\vec{r},\vec{r}\prime} \equiv 1$ for nearest-neighbor sites $\vec{r}$ and $\vec{r}\prime$ as energy scale and $t_{\vec{r},\vec{r}\prime} \equiv 0$ otherwise.

4.3   Results

4.3.1   Dispersion relations and DOS

We calculate the dispersion relations before including disorder for $\mathcal{L}_3(n)$, the results are summarized in Tab. 4.1. After picking some points of high symmetry forming a closed loop, they are drawn visually in the top line of Fig. 4.1. Compared to the two-dimensional dispersion relations, we found the energy of flat bands for $\mathcal{L}_3(n)$ and $\mathcal{L}_2(n)$ are exactly the same, but it's doubly degenerate for three dimensional cases. Just like in two dimensions, each $\mathcal{L}_3(n)$ has n flat bands separating $n+1$ dispersive bands, and there are linear Dirac cones touching flat bands at special points in the (k_x, k_y, k_z) plane for $\mathcal{L}_3(1)$ and $\mathcal{L}_3(3)$ but only parabolic-type dispersions for $\mathcal{L}_3(2)$ and $\mathcal{L}_3(4)$.

We now turn on the disorder, .i.e, $W > 0$, the disorder-dependent density of states(DOS) are calculated by direct diagonalization for small system sizes $M^3 = 5^3, 5^3, 4^3, 4^3$ for $\mathcal{L}_3(n)$, $n = 1, 2, 3, 4$, respectively. To obtain a good resolution, the DOS is generated from $W = 0$ to $W = 5.2$ in steps of 0.05 over 300 disorder configurations for $\mathcal{L}_3(n)$, $n = 1, 2, 3$, and 100 disorder configurations for $\mathcal{L}_3(4)$. A Gaussian broadening procedure, using Silverman's rule to determine the bandwidth broadening [104] of the energy levels, is applied to obtain a smoother DOS, and the results are displayed in the bottom line of Fig. 4.1. For weak disorder, the large peaks corresponding to original flat bands are prominent for all $\mathcal{L}_3(n)$ models. While from $W \sim 3$ onward, these peaks have merged into one broad DOS.

4.3.2   Phase diagrams

- For $\mathcal{L}_3(1)$ model

  Based on transfer matrix method(TMM), we calculated the energy-disorder phase diagram first for $\mathcal{L}_3(1)$ and show it in Fig. 4.2. The phase diagram was determined in terms of the scaling behavior of $\Lambda(E, W)$ for small system size $M = 6, 8$ and 10 with TMM error $\leq 0.1\%$ [105]. For $W < 1$, the data fluctuates too much and are hard to converge in finite number of iterations, hence results below $W < 1$ have been omitted from figure.
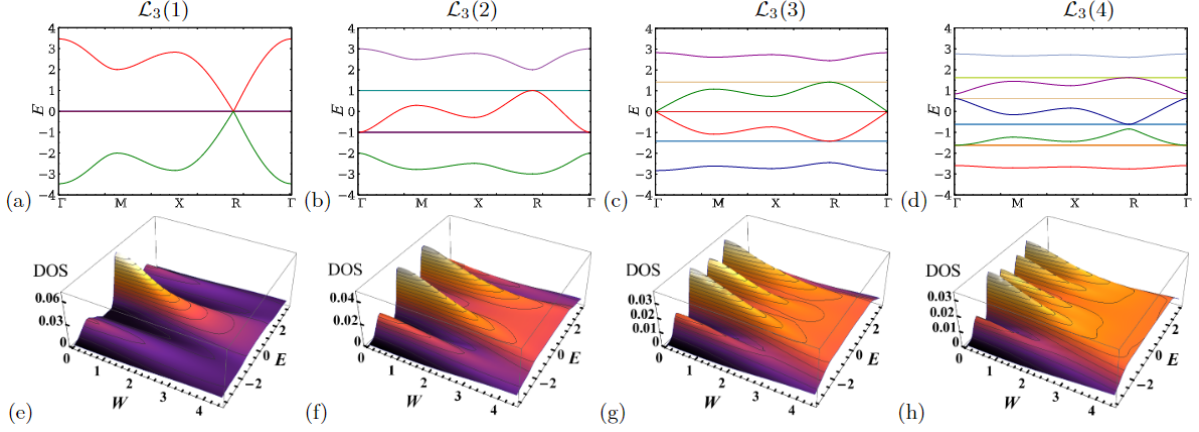
图 4.1: (a)–(d) Dispersion relations for clean systems and (e)–(h) dependence of the normalized DOS on W for $\mathcal{L}_3(1)$ to $\mathcal{L}_3(4)$. In all cases, the flat bands are doubly degenerate. In (a)–(d), we start in (k_x, k_y, k_z) space from the Γ point $(0, 0, 0)$, increase k as $(k, k, 0)$ until we reach the M point $(\pi, \pi, 0)$, decrease as $(k, \pi, 0)$ to the X point $(0, \pi, 0)$, increase via (k, π, k) to the R point (π, π, π), and last, decrease as (k, k, k) back to the Γ point at $(0, 0, 0)$. Different colors in the dispersion relations denote different bands while the colors in the DOS indicate different DOS values as also emphasized by the contour lines.

States are all extended inside the phase diagram, while are localized outside. There a special disorder at $E = 0$ described in the introduction, namely W_c as the disorder value at the transition point from extended to localized behaviour. Extended states coexist with localized states for any one disorder below W_c while extended states are absent once the disorder is greater that W_c, which means system is localized. Back to phase diagram itself, apparently, the phase diagram of $\mathcal{L}_3(1)$ is qualitatively similar to the phase diagram of the standard 3D cubic Anderson model, albeit the bandwidth and the critical disorder at $E = 0$ are different. In more details, compared with $W_c = 16.0(5)$ [102] of standard Anderson localization at $E = 0$, the critical disorder $W_c \sim 8$ of $\mathcal{L}_3(1)$ is reduced by about 50%. It is not particularly obvious that there is a small reentrant region in the band edges for $W \leq 4$, which is also appeared in the 3D Anderson models [106–109]. Nevertheless, the shoulders that develop at $E \sim 2.75$ and $W \sim 6$ seems a novel feature, which is absent in normal 3D Anderson model [106, 107] and other Anderson lattices [105, 110].

The inset of Fig. 4.2 shows that extended phase survives [111, 112], for flatband energy $E = 0$ even the disorder is as low as $W = 0.01$, as the values of Λ_M increase with increasing M.

- For $\mathcal{L}_3(2)$ and $\mathcal{L}_3(3)$ models

Following the same steps as $\mathcal{L}_3(1)$, the phase diagrams for $\mathcal{L}_3(2)$ and $\mathcal{L}_3(3)$ have

	The number of atoms in a unit cell	The number of flat bands	dispersion relations	
$\mathcal{L}_3(1)$	4	2	$E_{1,2} = 0$ $E_{3,4} = \pm\sqrt{6 + 2q}$	$q = \cos k_x + \cos k_y + \cos k_z$
$\mathcal{L}_3(2)$	7	4	$E_{1,2} = 1$ $E_{3,4} = -1$ $E_5 = \rho_+ + \rho_-$ $E_6 = \omega\rho_+ + \omega^2\rho_-$ $E_7 = \omega\rho_- + \omega^2\rho_+$	$\omega = \frac{-1+\sqrt{3}i}{2}$ $\rho_\pm = \sqrt[3]{q \pm \sqrt{q^2 - \left(\frac{7}{3}\right)^3}}$
$\mathcal{L}_3(3)$	10	6	$E_{1,2} = \sqrt{2}$ $E_{3,4} = -\sqrt{2}$ $E_{5,6} = 0$ $E_{7,8,9,10} = \pm\sqrt{4 \pm \sqrt{10 + 2q}}$	
$\mathcal{L}_3(4)$	13	8	$E_{1,2,3,4,5,6,7,8} = \frac{1}{2}\left(\pm 1 \pm \sqrt{5}\right)$ $E_{9,10,11,12,13} \rightarrow\ E^5 - 9E^3 + 13E - 2q = 0$	

表 4.1: Dispersion relations for $\mathcal{L}_3(n)$, $n = 1, 2, 3, 4$. Need to mention, we have chosen the unit length in real space to be 1, and k_x, k_y are the wave vectors in the reciprocal space. Similar to $\mathcal{L}_2(2)$, even though the $E_{6,7}$ of $\mathcal{L}_3(2)$ looks like it has an imaginary part, actually they are real roots as ρ_+ and ρ_- are complex conjugates of each other and the same as ω and ω^2.

been calculated and displayed in Fig. 4.3. The data are determined with TMM error of $\leq 0.2\%$ and with the same system sizes as for $\mathcal{L}_3(1)$. For the same reason as before, we just consider the disorder $W \leq 1$. Our simulation support, as for $\mathcal{L}_3(1)$, a mirror symmetry at $E = 0$ and hence the data are shown in Fig. 4.3 after explicitly symmetrization. To be specific, we picked the points that are symmetrically distributed with respect to $E = 0$, usually the Λ_M of these two symmetric points is different due the presence of random disorder, hence we take the average of these two Λ_M values and return it back to these two points. Next, we found there are also reentrant behaviours for the phase boundaries of the central dispersive band for both $\mathcal{L}_3(2)$ and $\mathcal{L}_3(3)$, although this is not obvious for $\mathcal{L}_3(3)$. Similarly, the extended behavior at low disorder for the flat band energy at $E = 1$ is indicated in the inset of Fig. 4.3 (a).

The obvious difference between the phase diagrams of $\mathcal{L}_3(1)$, $\mathcal{L}_3(2)$ and $\mathcal{L}_3(3)$ is that the extended region for $\mathcal{L}_3(1)$ lattice is simply connected, while for $\mathcal{L}_3(2)$ and $\mathcal{L}_3(3)$ it is disjoint. This difference can be attributed to the presence of the energy gaps in $\mathcal{L}_3(2)$ and $\mathcal{L}_3(3)$ as in Fig. 4.1. Recall the critical disorder W_c mentioned
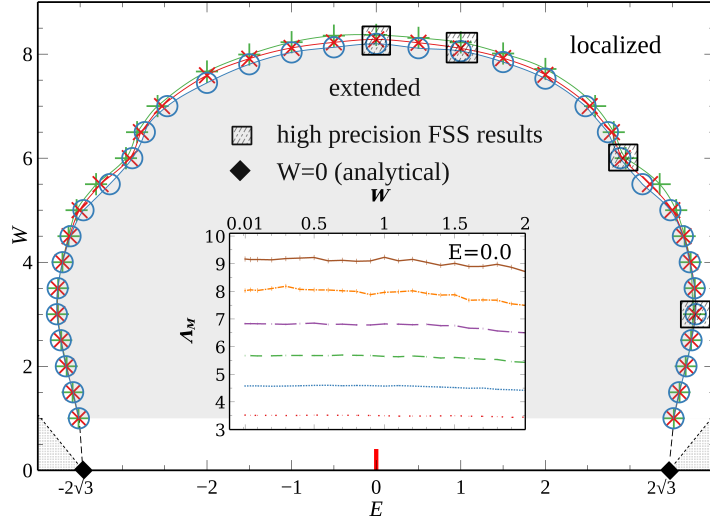
图 4.2: Phase diagram for $\mathcal{L}_3(1)$. The three solid and colored lines represent the approximate location of the phase boundary estimated from small M, i.e. the blue line is constructed by widths $M = 6$ and $M = 8$ with blue circle ($\bigcirc$), and red line by widths $M = 6$ and $M = 10$ with red cross ($\times$), and green line by width $M = 8$ and $M = 10$ with green plus ($+$). The solid squares ($\square$) filled with dashed lines denote high-precision estimates from FSS for large M. The shaded area in the center contains extended states while states outside the phase boundary are localized. The dashed lines on both sides are guides-to-the-eye for the expected continuation of the phase boundary for $W < 1$. The red short vertical line at $E = 0$ represents the position of the two-degenerate flat bands. The diamonds ($\blacklozenge$) denote the band edges for $W = 0$, i.e. $E_{\min} = -2\sqrt{3}$ and $E_{\max} = 2\sqrt{3}$. The dotted lines are the theoretical band edges $\pm(|E_{\min}| + W/2)$ and the forbidden areas below those band edges have been shaded. Inset: Weak disorder behavior at the flat band energy $E = 0$ down to $W = 0.01$. The strip widths vary from $M = 4$ (sparse dotted line), 6 (condensed dotted), 8 (short dashed), $M = 10$ (long dashed), $M = 12$ (dashed-dotted) to $M = 14$ (solid). Error bars are shown but very small.

above, we see that the critical disorders are $W_c \sim 16.530$ for the cubic lattice [103], where n can be regard as 0, ~ 8.6 for $\mathcal{L}_3(1)$, ~ 5.9 for $\mathcal{L}_3(2)$ and ~ 4.8 for $\mathcal{L}_3(3)$, hence manifests a downward trend as n increase. Hence as expected, in the Lieb lattices the last extended states vanish already at much weaker disorders and the trend becomes stronger with increasing n in each successive $\mathcal{L}_3(n)$.

4.3.3 High-precision determination of Critical properties for the Lieb models

- Model of $\mathcal{L}_3(1)$

In order to determine the critical properties at the phase boundaries for the Lieb models, it's necessary to calculate larger system size for a reliable FSS. In all cases,
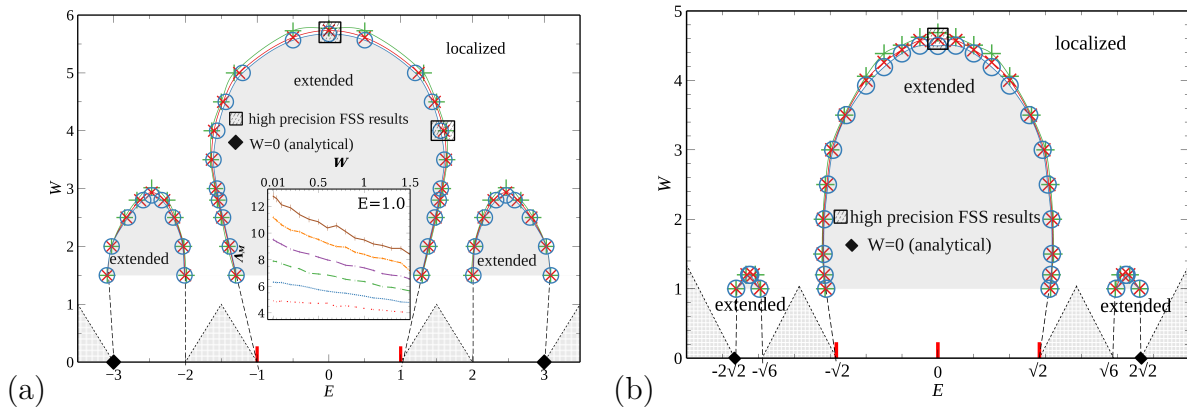
图 4.3: Phase diagrams for (a) $\mathcal{L}_3(2)$ and (b) $\mathcal{L}_3(3)$ lattices. The symbols, lines and colors are as in Fig. 4.2, i.e. representing small M estimates with $M = 6, 8$ and 10. The solid squares ($\square$) denote high-precision FSS results from Λ_M with an TMM error $\leq 0.1\%$ for width $M \leq 16$ and $\leq 0.2\%$ for width $M = 18$. The diamonds ($\blacklozenge$) denote the maximal band edges from $W = 0$ at ± 3 for $\mathcal{L}_3(2)$ and $\pm 2\sqrt{2}$ for $\mathcal{L}_3(3)$. Inset for (a): Weak disorder behavior at the flat band energy $E = 1$ down to $W = 0.01$ with error bars and lines indicated as in Fig. 4.2, i.e., the strip widths vary from $M = 4$ (sparse dotted line) to $M = 14$ (solid).

the results are collected up to $M = 20$ and with TMM convergence errors $\leq 0.1\%$. Based on the phase diagram as in Fig. 4.2 as a rough guide, four points of special interest are picked out, namely, two transitions as a function of W at the band centre at constant $E = 0$ and outside the band centre at $E = 1$; the other two transitions are studied as function of E corresponding to the point marking the reentrant behaviour [106] at constant $W = 3$ and the kink in the phase boundary at constant $W = 6$. In Fig. 4.4, we collect the $\Lambda_M(E, W)$ data, the resulting scaling curves and the variation of the scaling parameter ξ for typical examples of FSS results in a plot. The upper and lower scaling curves represent the extended and localized states, respectively.

In Table ?? we list fits for all 4 cases shown in Fig. 4.4 with higher expansion coefficients n_r and m_r. The consistent results with respect to an increase in an expansion parameter show that our results are stable. We have also checked that they are stable with respect to slight changes in the choice of parameter intervals δW and δE for fixed energy and fixed disorder transitions, respectively. By the way, in the averages part, we considered the error propagation. For instance, 3 quantities a, b, and c with uncertainties δa, δb, and δc, then the uncertainty of quantity d, defined as the average of these 3 quantities, .i.e $d = (a + b + c)/3$, is given by $\delta d = \sqrt{((\delta a)^2 + (\delta b)^2 + (\delta c)^2)/3^2}$.

However, the careful readers must have noticed from the absence of irrelevant pa-

图 4.4: (a) FSS of the localization lengths for $\mathcal{L}_3(1)$ with $E = 0$, (b) $E = 1$, (c) $W = 3$, and (d) $W = 6$. System sizes M are 14 (grey +), 16 (dark yellow ×), 18 (blue +), 20 (purple ⊙). The left half in each panel denotes a plot of Λ_M versus disorder W or energy E, the solid lines are fits to the data acquired by Eqs. (2.31)–(2.33) with (a+b) $n_r = 3$, $m_r = 1$, (c) $n_r = 2$, $m_r = 1$ and (d) $n_r = 1$, $m_r = 1$. The right half in each panel shows the scaling function F (solid line) and the scaled data points with the same n_r and m_r as in the corresponding left half while each inset gives the scaling parameter ξ as a function of disorder strength W, in (a) and (b), or energy E in (c) and (d). The parameters of the fits are shown in detail in Table **??**.
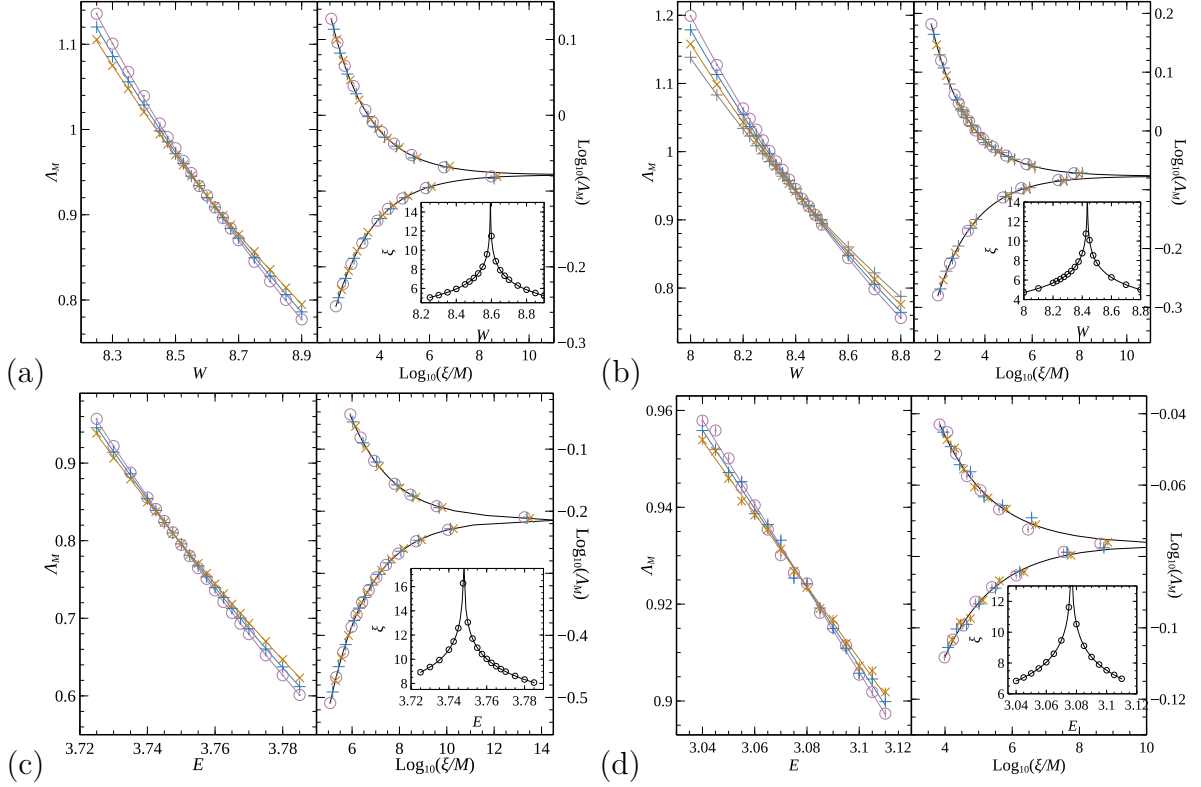
rameters n_i and m_i, this is caused by the poor data quality. We found the accuracy and size of the data are not good enough to reliably fit irrelevant scaling contributions and hence the results in Table **??** are all for $n_i = m_i = 0$ although we have indeed performed our FSS allowing for these additional parameters. Furthermore, we can find out in Fig. 4.4 that the accuracy of the TMM data becomes worse for the fixed disorder transitions at $W = 3$ and especially $W = 6$. The reason for this behaviour is in principle well understood since at the points, the DOS has an appreciable variation which leads to extra corrections not well captured in the FSS [113]. Usually, larger system sizes M can reduce these variations but this is not possible here due to computational limitations.

- Models $\mathcal{L}_3(2)$ and $\mathcal{L}_3(3)$

We follow a similar strategy as in the previous section in order to finite-size scale
the localization lengths for $\mathcal{L}_3(2)$ and $\mathcal{L}_3(3)$. The TMM convergence errors were
chosen as $\leq 0.1\%$ up to $M = 16$ and, due to the increased complexity of these
models, as $\leq 0.2\%$ for the largest system size with $M = 18$. For model $\mathcal{L}_3(2)$ at
energy $E = 0$, we give a plot combining scaling data $\Lambda_M(E = 0, W)$ and scaling
curves with $n_r = 3, m_r = 3$ as shown in Fig. 4.5(a). It is very hard to observe a
clear crossing at W_c from the panel with the $\Lambda_M(E = 0, W)$ data. The situation
improves for $\Lambda_M(E, W = 4)$ in Fig. 4.5(b) which exhibits a clear crossing of Λ_M
around $E_c \sim 1.70$. For model $\mathcal{L}_3(3)$, as the increased complexity, we just focus on
$E = 0$. Similarly with $\mathcal{L}_3(2)$, the crossing for $\Lambda_M(E = 0, W)$ is again somewhat
less clear as shown in Fig. 4.5(c).

Nevertheless, in all three cases, the FSS results produce stable and robust fits with
estimates for W_c, E_c and ν as shown in Table **??**.
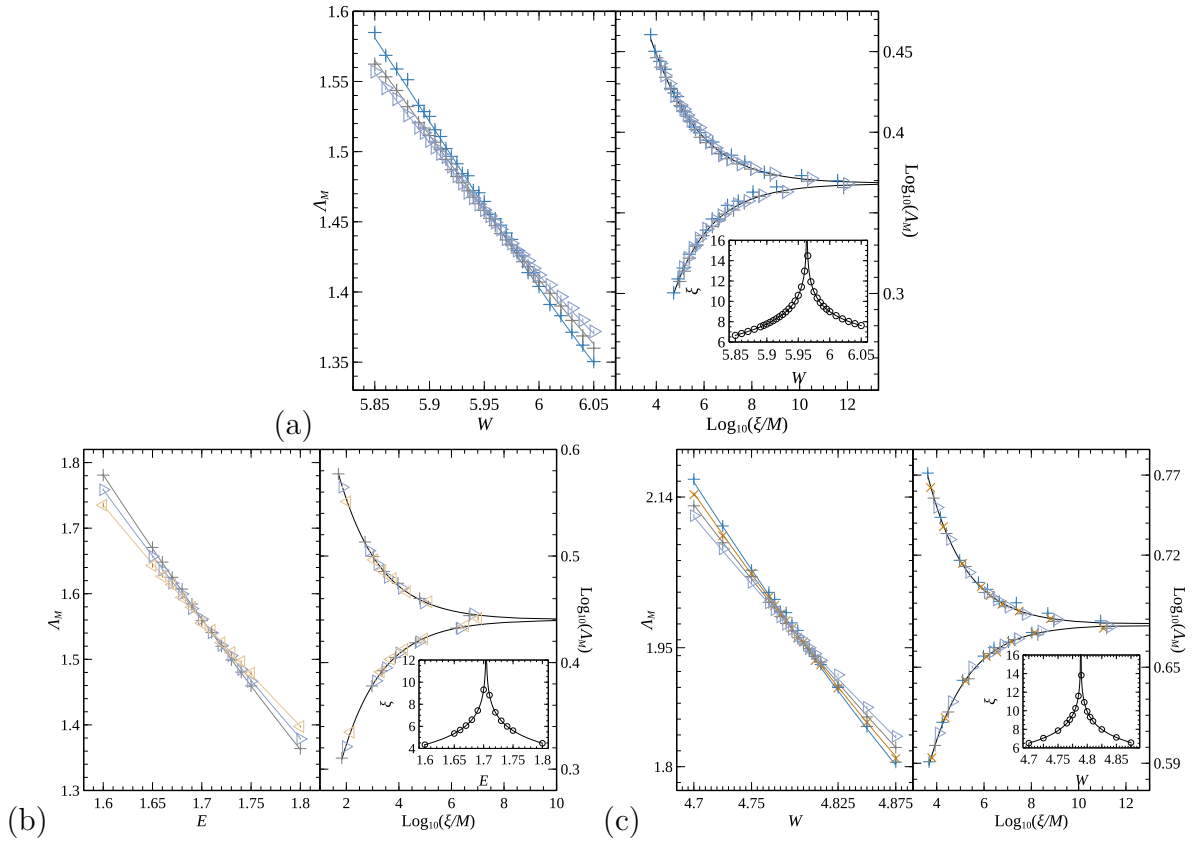
图 4.5: FSS of the localization lengths for (a) $\mathcal{L}_3(1)$ at $E = 0$ and (b) $W = 4$ as well as for (c)
$\mathcal{L}_3(3)$ at $E = 0$. System sizes M are 10 (orange ◁), 12 (blue ▷), 14 (grey +), 16 (dark yellow
×), 18 (blue +). The arrangement in each panel is as in Fig. 4.4, i.e. scaling curves (solid lines)
and scaled Λ_M data (symbols) in the left half of each panel, scaling curve F (lines) with scaled
dat a (symbols) in the right half and ξ in the inset. The chosen expansion coefficients are (a)
$n_r = 2$, $m_r = 2$, (b) $n_r = 2$, $m_r = 1$ and (c) $n_r = 2$, $m_r = 1$ as highlighted in Table **??**.

4.4 Conclusion

We studied the localization properties and the Anderson transition in the 3D Lieb lattice $\mathcal{L}_3(1)$ and its extensions $\mathcal{L}_3(n)$ in the presence of disorder. We computed the disorder-broadened density of states and the energy-disorder phase diagrams for up $n = 4$. Via finite-size scaling, we obtained the critical properties such as critical disorders and energies as well as the universal localization lengths exponent ν, and we summarized all the averaged critical exponents ν in Fig. 4.6. We found that the critical disorder W_c decreases from ~ 16.5 for the cubic lattice, to ~ 8.6 for $\mathcal{L}_3(1)$, ~ 5.9 for $\mathcal{L}_3(2)$ and ~ 4.8 for $\mathcal{L}_3(3)$. Nevertheless, the value of the critical exponent ν for all Lieb lattices studied here and across various disorder and energy transitions agrees within error bars with the generally accepted universal value $\nu = 1.590\ (1.579, 1.602)$.
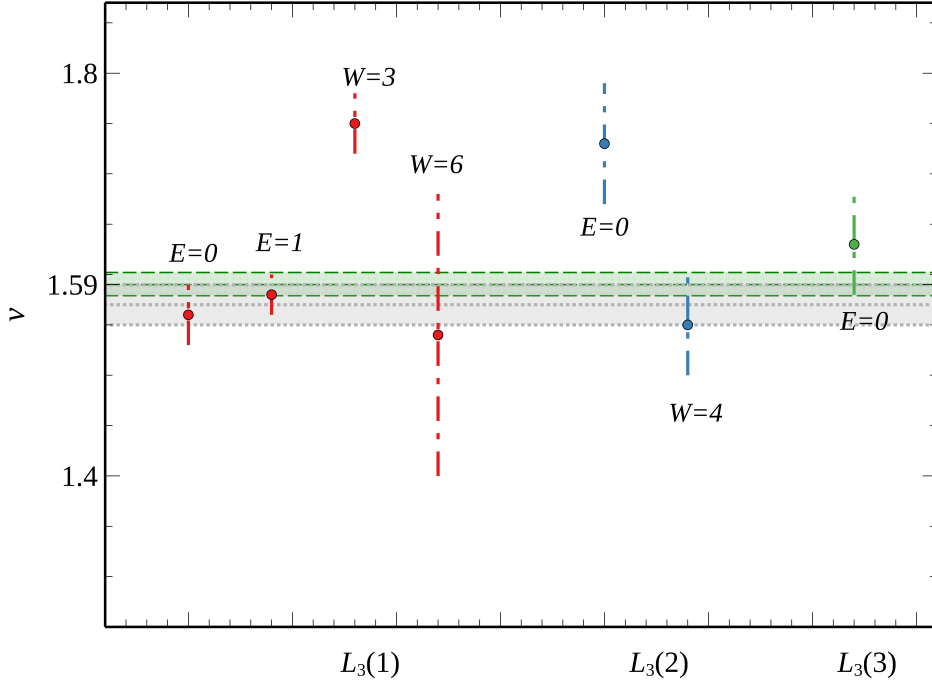
图 4.6: Variation of the averaged critical exponent ν corresponding to $\mathcal{L}_3(1)$ (red), $\mathcal{L}_3(2)$ (blue) and $\mathcal{L}_3(3)$ (green) for the seven averages from Table **??**. The green horizontal dash lines indicate $\nu = 1.590(1.579, 1.602)$ via FSS of wave functions in the 3D Anderson model [103] and the green shadow area denotes its error range. The $\nu = 1.57(2)$ value, indicated by grey dotted lines with grey shadow area denoting its error bar, is from TMM results [6].

Chapter5 Localization properties in Lieb lattices and their extensions

5.1   Introduction

Flat band systems, in which the absence of a dispersion in the band structure leads to a highly dramatic macroscopic degeneracy, have at the flat band energy an effectively reduced kinetic energy. Hence other terms in the Hamiltonian can become prominent, such as many-body interactions. As is well known, states in a flat band are localized [61] because of the high degeneracy. Hence disorder, which one should expect to destroy this degeneracy, might also, at least initially, destroy the localization. So what will happen after disorder is being included in the Hamiltonians describing these localized flat bands is an interesting problem.

In this paper, we are mainly supplementing the previous results [68,69] as introduced in first two chapter.

5.2   Models

The models we consider in this work are $\mathcal{L}_2(n)$ and $\mathcal{L}_3(n)$ with $n = 1, 2, 3, 4$ as shown in Fig. 2.1. The Hamiltonian gives as Equ. 3.1 or Equ. 4.1.

5.3   Results

5.3.1   The two-dimensional Lieb lattice and its extensions

- Previous results for disordered $\mathcal{L}_2(n)$ lattices

  In our previous paper [68], we study the localization properties of $\mathcal{L}_2(n)$ in detail.

  Using direct diagonalization for small system sizes, we compute the density of states (DOS). We can see that in the presence of disorder, the interplay between flat bands and dispersive bands is prominent for all $\mathcal{L}_2(n)$, $n = 1, 2, 3$ and 4. The disorder can quickly lift the degeneracy of flat bands and make the states merge with the neighboring dispersive bands. When $W \gtrsim 2$, the flat band DOS loses its peaks distinguishing and becomes part of a large bulk DOS.

  Next, we use a renormalized transfer-matrix method (TMM) and compute the reduced localization lengths $\Lambda_M(E, W) = \lambda(E, W)/M$, where M corresponds to the width of the quasi-1D transfer-matrix strip. For all $\mathcal{L}_2(n)$, we find that for

$W \gtrsim t$ all states are localized. The localization lengths for states at flat band energies are about one order of magnitude smaller than for states from dispersive bands. We employ traditional one-parameter finite-size scaling methods to estimate a scaling parameter $\xi(E, W)$ [102]. The $\Lambda(E, W)/M$ can be described after scaling by a single scaling branch, corresponding to a fully localized behaviour. After fitting the ξ with disorder W, we use three fitting forms, power low form as $\xi(W) \propto W^{-2}$ [70], a non-universal form $\xi(W) = aW^{-\alpha} \exp(\beta W^{-\gamma})$ and a constraint form $\xi(W) = aW^{-2} \exp(\beta W^{-1})$. For $\mathcal{L}_2(1)$ and $\mathcal{L}_2(3)$ at the flat band energy $E = 0$, we find that the usual power low form $\xi(W) \propto W^{-2}$ for 1D localization fits well for disorder around $1 < W < 2$. However, for $\mathcal{L}_2(2)$ and $\mathcal{L}_2(4)$ at $E = 0$, which is an energy in a dispersive band for these lattices, none of the fits gives a convincing result.

- Scaling function Λ_M vs reduced correlation length ξ_M for $\mathcal{L}_2(n)$
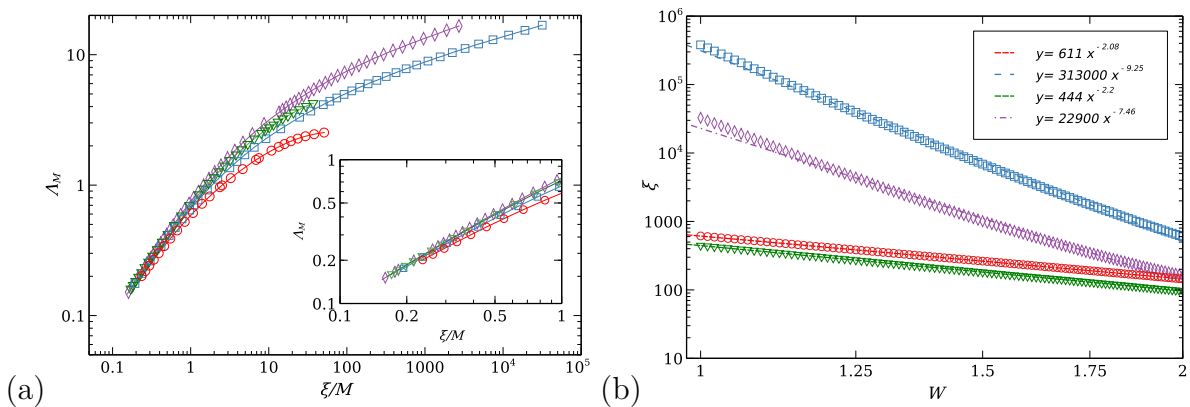
图 5.1: (a) Scaled localization length $\Lambda_M(0, W)$ versus ξ/M at energy $E = 0$ for $\mathcal{L}_2(1)$ (red $\bigcirc$), $\mathcal{L}_2(2)$ (blue $\square$), $\mathcal{L}_2(3)$ (green $\triangledown$) and $\mathcal{L}_2(4)$ (purple $\diamondsuit$). For clarity, lines show all data points while symbols denote only about 15% of all data. Inset: the detail of small reduced correlation length. (b) Scaling parameters $\xi(0, W)$ for the same Lieb lattices as in (a). The dashed lines represent the power law fit functions ax^b. Error bars are within symbol size in both panels.

The scaled localization lengths $\Lambda_M(0, W)$ as a function of scaled correlation length ξ/M for $\mathcal{L}_2(n)$, $n = 1, 2, 3$ and 4 are shown in Fig. 5.1(a) at energy $E = 0$. This corresponds to flat bands for $\mathcal{L}_2(1)$ and $\mathcal{L}_2(3)$ and dispersive band for $\mathcal{L}_2(2)$ and $\mathcal{L}_2(4)$. The $\Lambda_M(0, W)$ data all show the behaviour for localized states, scaling as $\Lambda_M(0, W) \propto \xi(0, W)/M$ for large system sizes and large disorders. In this regime, the behaviour of states in the flat bands and in the dispersive bands is similar as shown also in the inset graph of said figure.

- Scaling parameter ξ vs disorder W for $\mathcal{L}_2(n)$

$$\mathcal{L}_2(n)$$

$$\mathcal{L}_3(n)$$
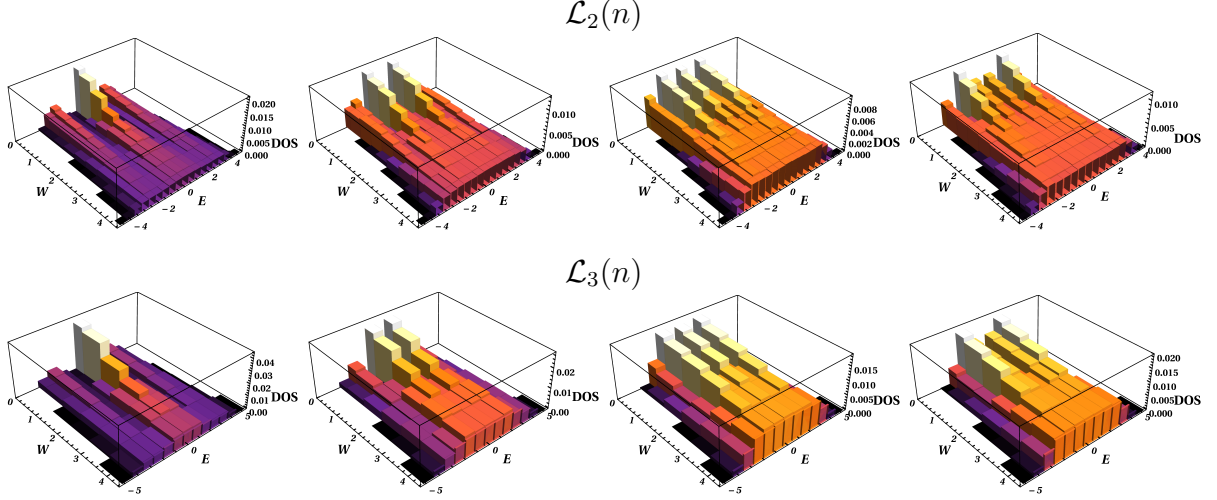
图 5.2: Normalized bar chart histograms of the (E,W)-dependence of the density of states (DOS) for $\mathcal{L}_2(n)$ and $\mathcal{L}_3(n)$. Upper line are for $\mathcal{L}_2(1)$ to $\mathcal{L}_2(4)$, and bottom line are for $\mathcal{L}_3(1)$ to $\mathcal{L}_3(4)$. The colors denote different DOS values ranging from zero (deep purple) to maximal (white). Bin widths in (E,W) directions have been chosen for representational clarity.

The disorder dependence of the scaling parameter ξ for small disorders $t \leq W \leq 2t$ is shown in Fig. 5.1(b), computed from the $\Lambda_M(E=0,W)$ data of Fig. 5.1(a). We see that the behaviour of ξ for $\mathcal{L}_2(1)$ is comparable to $\mathcal{L}_2(3)$; both are well-described by a power law ax^b with exponent approximately $b \sim -2$, similar to localization properties of a standard 1D Anderson model [70]. This might suggest that the localization behaviour of these disordered flat band states at least for weak disorder is similar to the 1D behaviour. On the other hand, for the dispersive states of $\mathcal{L}_2(2)$ and $\mathcal{L}_2(4)$ at $E = 0$, we find that the values of ξ are orders of magnitude larger than for $\mathcal{L}_2(1)$ and $\mathcal{L}_2(3)$. The simple power-law also does not fit anymore and we rather see the more standard behaviour of a 2D Anderson model [70] with a quickly diverging ξ when $W \to 0$. Nevertheless, for both flat band and dispersive band energies, the fits are not very robust and have rather small p values of $< 10^{-10}$. This shows that the true form of the behaviour of $\xi(W \to 0)$ is yet to be determined.

- Density of states without Gaussian broadening for $\mathcal{L}_2(n)$

  The results of the disorder-averaged density of states (DOS), calculated with direct diagonalization, are shown in Fig. 5.2. The system sizes are $M^2 = 13^2$, 10^2, 9^2, 8^2 for $\mathcal{L}_2(n)$, $n = 1, 2, 3$ and 4, respectively. The disorder ranges from $W = 0$ to $W = 5.2$ in steps of 0.05 using 300 independent random samples. We can see the prominent peaks of flat bands close to $W = 0$ have been largely vanished when the disorder reaches up to $W = 2$ for all $\mathcal{L}_2(n)$, $n = 1, 2, 3$ and 4.

5.3.2   Three-dimensional Lieb lattice and its extensions

- Previous results for disordered $\mathcal{L}_3(n)$ lattices

  In Ref. [69], we investigated the DOS, the localization properties and the phase diagrams for the 3D Lieb lattices $\mathcal{L}_3(n)$, $n = 1, 2, 3$ and 4. Obviously, the main difference to the 2D case is the existence of an Anderson metal insulator transition (MIT) in 3D Lieb lattices [69]. Details of the TMM construction for $\mathcal{L}_3(n)$ can also be found in Ref. [69] along with finite-size scaling results for the universal critical exponent ν of the localization lengths. We found ν to be in good agreement with the currently accepted value of $\nu = 1.590(1.579, 1.602)$ [6,103] for the Anderson transition. In the following, we shall elaborate on the stability of the phase diagrams to a change in boundary conditions, highlight the various positions of the transitions in the phase diagrams, comment on the possibility of FSS with irrelevant scaling parameters and also provide the DOS without Gaussian-broadening.

- Phase diagram with periodic boundary condition for $\mathcal{L}_3(1)$

  The phase diagrams given in Ref. [69] have been computed for the $\mathcal{L}_3(n)$ lattices with hard wall boundaries. In Fig. 5.3(a) we now show a phase diagram for $\mathcal{L}_3(1)$ with periodic boundary condition. The phases have been determined by the scaling behaviour of the $\Lambda_M(E, W)$ for system sizes $M = 4$, $M = 6$ and $M = 8$ with error $\leq 0.1\%$ [105]. Comparing this to the results obtained with hard boundary conditions, we find that it looks very similar as expected although the extended region is a little wider in the E axis. As for the hard wall case, we can identify a re-entrant region around disorder $W = 4$ and a shoulder at $E \sim 3$ and $W \sim 6$. Hence as expected, the change in boundary conditions does not change the phase diagrams appreciably already with the small system sizes and modest disorder averages as used here and in Ref. [69].

- Localization and extended transition with $0.01 \leq W \leq 2.0$

  For $W < 1$, it is well known that the convergence of the TMM is very slow. Hence results for appropriately small errors are hard to compute. Usually, this is not a problem since, e.g., in the 3D Anderson model, the limit as $W \to 0$ belongs trivially to the extended phase. However, for the $\mathcal{L}_3(n)$ lattice, we know that at the flat band energies even at $W = 0$, we except compactly localized states [15,114]. Hence it is interesting to see if the localization properties at $W < 1$ for flat band energies indicate any possible "inverse" Anderson transition from extended states at $W \sim 1$ to localized states at small, but finite $W > 0$.
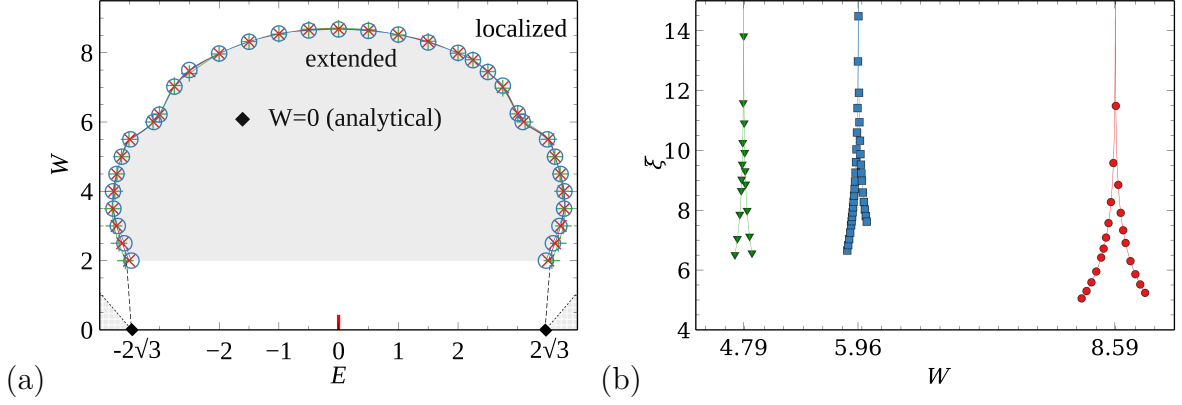
图 5.3: (a) Phase diagram for $\mathcal{L}_3(1)$ in case of periodic boundaries. The three solid and colored lines represent the approximate location of the phase boundary estimated from small M, i.e. the blue line/◯ comes from widths $M = 4$ and $M = 6$, the red line/× from $M = 4$ and $M = 8$, and the green line/+ from $M = 6$ and $M = 8$. The shaded area in the center contains extended states while states outside the phase boundary are localized. The dashed lines on both sides are guides-to-the-eye for the expected continuation of the phase boundary for $W < 2$. The red short vertical line at $E = 0$ represents the position of the doubly-degenerate flat band. The diamonds (♦) denote the band edges for $W = 0$, i.e. $E_{\min} = -2\sqrt{3}$ and $E_{\max} = 2\sqrt{3}$. The dotted lines are the theoretical band edges $\pm(|E_{\min}| + W/2)$ and the forbidden areas below those band edges have been shaded. (b) Scaling parameters ξ versus disorder W for $\mathcal{L}_3(1)$(red ◯), $\mathcal{L}_3(2)$ (blue □) and $\mathcal{L}_3(3)$ (green ▽) at energy $E = 0$. The expansion parameters n_r, n_i, m_r and m_i are the same as the highlighted line in Table 5.1.

In Ref. [69], we had shown that at the flat band energy $E = 0$ for $\mathcal{L}_3(1)$ and at $E = 1$ for $\mathcal{L}_3(2)$, the Λ_M increases with increasing M, indicating extended behaviour, down to disorders as small as $W = 0.01$. In Fig. 5.4(a-c), we now augment that result by studying energies close by. For $\mathcal{L}_3(1)$ and $E = 0.05$ we initially find localized behaviour, e.g., Λ_M decreasing with increasing M up to $M = 10$, but then reversing to extended behaviour for larger M. For $E = 0.1$ the reversal to the extended behaviour already starts at $M = 8$ while for $E = 0.15$, only the extended behaviour remains. In Fig. 5.4(d), we see that for $\mathcal{L}_3(2)$ at $E = 1.05$, the Λ_M decreases with increasing M. This localized behaviour at small W values results from the energy gap for $E > 1$ in the clean system.

We conclude that the presence of the compactly localized states at the flat band energies certainly has an effect at small disorder in terms of the M dependence of Λ_M. For large enough M, we find that the character of the states remains extended down to disorders $W = 0.01$.

- Divergence of the scaling parameter $\xi(W)$
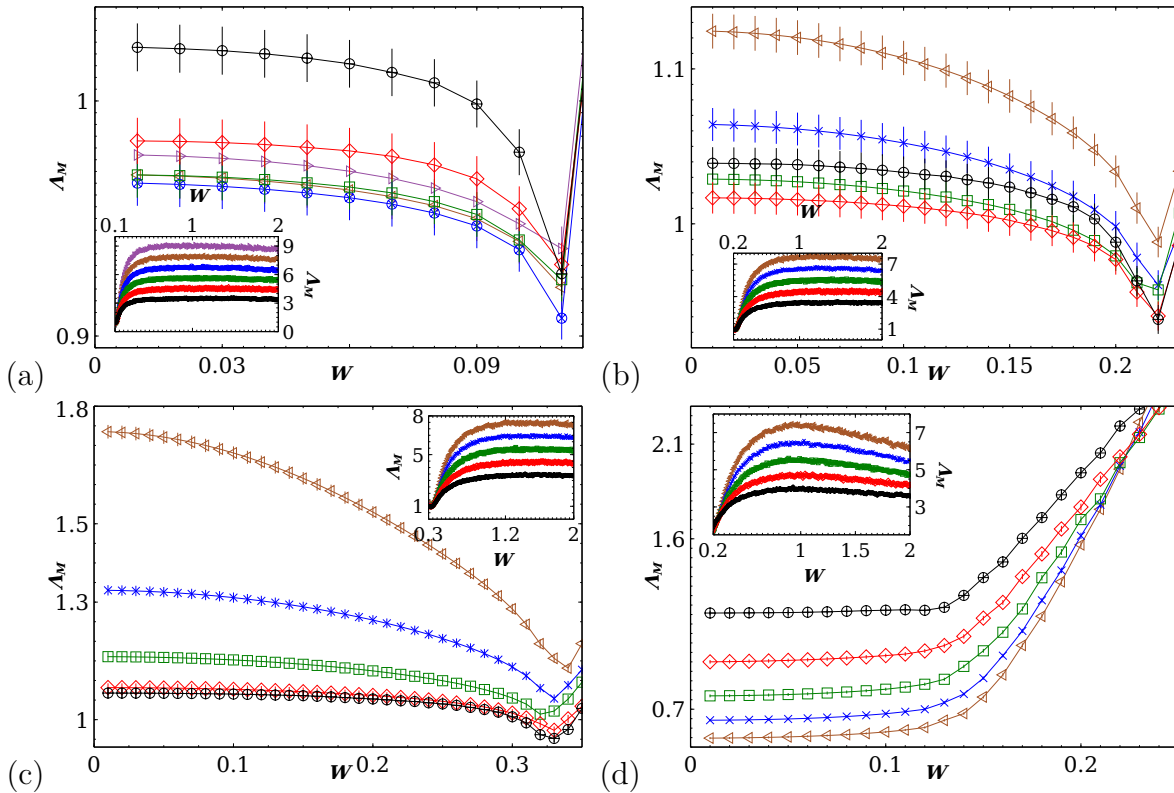
图 5.4: (a) Small W behaviour of Λ_M for $\mathcal{L}_3(1)$ with (a) energy $E = 0.05$, (b) $E = 0.1$, (c) $E = 0.15$, and (d) for $\mathcal{L}_3(2)$ at $E = 1.05$ with disorder down to 0.01 in steps of 0.01 and with error less than 1.0%. System sizes M are 4 (black ⊕), 6 (red ◇), 8 (green □), 10 (dark-blue ×), 12 (brown ◁), 14 (purple ▷). Error bars are denoted with a solid line. Insets: increased disorder range up to $W = 2$ for the corresponding cases in the 4 main panels.

The behaviour of $\xi(W)$ for $\mathcal{L}_3(1)$, $\mathcal{L}_3(2)$ and $\mathcal{L}_3(3)$ is given in Fig. 5.3. We can clearly see how the critical disorder W_c decreases from 8.59 for $\mathcal{L}_3(1)$ to 5.96 for $\mathcal{L}_3(2)$ and finally to 4.79 for $\mathcal{L}_3(3)$. This suggests that a larger n in $\mathcal{L}_3(n)$, i.e. a larger number of additional (red, cp. Fig. 2.1) atoms, leads to stronger localization and hence an MIT already for smaller values of W_c. It could be an interesting study to estimate $W_c(n)$, particularly the limiting behaviour when $n \to \infty$.

- Scaling with irrelevant variables n_i, m_i

  For high-precision estimates of critical properties, including ν, it is by now state of the art to include irrelevant scaling contributions, i.e. scaling as M^{-y} with $y > 0$, in the FSS analysis. However, such FSS methods also require large M values to reliably model the irrelevant scaling. Due to the complexity of the $\mathcal{L}_3(n)$ systems, only values of $M \leq 20$ have been computed in Ref. [69]. For such sizes, adding irrelevant scaling variables is usually not a net benefit. In Table 5.1, we show the results for FSS with and without scaling. We note that although acceptable p values

58

can be obtained for the fits with irrelevant scaling exponent y included, in nearly all cases, this results either in increased error estimates for the relevant exponent ν. Alternatively, one finds estimates for y with very large errors or very large values for y. Except for one case, the final estimate for the physical quantity ν has hardly changed. Hence we conclude that for the available Λ_M data, the inclusion of irrelevant scaling parameter y does not necessarily add towards the accuracy of the estimates for ν. This confirms having made this choice in Ref. [69].

- Density of states without Gaussian broadening for $\mathcal{L}_3(n)$

  The results of for the DOS, calculated with exact diagonalization and without applied Gaussian smoothing, are in Fig. 5.2. The system sizes are $M^3 = 5^3$, 5^3, 4^3, 4^3 for $\mathcal{L}_3(n)$, $n = 1, 2, 3$ and 4, respectively. The disorder ranges are all from $W = 0$ to $W = 5.2$ in step of 0.05 and with 300 samples for $n = 1, 2, 3$ but only 100 samples for $\mathcal{L}_3(4)$ because of computing time limits. Again, the results are very similar to the Gaussian-broadened DOS shown in Ref. [69].

5.4 Conclusion

We have studied the localization properties of the 2D and 3D extended Lieb lattices in this paper. Clearly, the Lieb lattices exhibit stronger localization than their more standard square and cubic Anderson lattices. This can be understood by noting that the transport along the "extra" sites as shown (by red spheres) in Fig. 2.1 is essentially one-dimensional and hence subject to stronger localization. Consequently, in 2D rather small W values can still be studied (most earlier TMM studies for the 2D Anderson model stop already around $W \sim 2$, cp. Fig. (3) of Ref. [94]). Details of the resulting FSS curves for small W are given in Fig. 5.1. In 3D, we similarly see that $W_c(n)$ decreases as a function of n. Results for states near flat bands with particularly small W are shown in Fig. 5.4. Due to the numerical complexity of the $\mathcal{L}_d(n)$ systems, scaling is more challenging than in the Anderson models and only relatively small M values can be reached. Table 5.1 shows that for the available data, there is no need to include irrelevant scaling variables — within the accuracy of the calculation, all estimates of the critical exponent agree with the value found for the Anderson universality class [6, 103].

$$\mathcal{L}_3(1)$$

ΔM	E	δW	n_r	n_i	m_r	m_i	W_c	CI(W_c)	ν	CI(ν)	y	CI(y)	p
16-20	0	8.25-8.9	3	0	1	0	**8.59**	$(58,61)$	**1.6**	$(4,7)$	0	0	0.15
16-20	0	8.25-8.9	2	1	1	1	8.71	$(57,84)$	1.3	$(0.8,1.8)$	4	$(-2,10)$	0.86
14-20	1	8.0-8.8	3	0	1	0	**8.44**	$(42,45)$	**1.6**	$(5,7)$	0	0	0.18
14-20	1	8.0-8.8	3	2	1	1	8.48	$(45,50)$	1.8	$(6,9)$	6.9	$(6.6,7.1)$	0.77

ΔM	W	δE	n_r	n_i	m_r	m_i	E_c	CI(E_c)	ν	CI(ν)	y	CI(y)	p
16-20	3	3.725-3.785	2	0	1	0	**3.75**	$(74,75)$	**1.7**	$(6,9)$	0	0	0.88
16-20	3	3.725-3.785	3	2	1	2	3.75	$(74,75)$	1.5	$(0.6,2.5)$	2	$(-3,8)$	0.7
16-20	6	3.04-3.11	1	0	1	0	**3.08**	$(07,09)$	**1.5**	$(1.0,2.1)$	0	0	0.14
16-20	6	3.04-3.11	1	1	2	1	3.08	$(06,09)$	1.5	$(0.7,2.4)$	47	$(44,50)$	0.13

$$\mathcal{L}_3(2)$$

ΔM	E	δW	n_r	n_i	m_r	m_i	W_c	CI(W_c)	ν	CI(ν)	y	CI(y)	p
12,14,18	0	5.85-6.05	2	0	2	0	**5.96**	$(95,97)$	**1.8**	$(1.5,2.0)$	0	0	0.08
12,14,18	0	5.85-6.05	2	1	1	4	5.97	$(96,98)$	1.7	$(1.3,2.1)$	9	$(2,16)$	0.89

ΔM	W	δE	n_r	n_i	m_r	m_i	E_c	CI(E_c)	ν	CI(ν)	y	CI(y)	p
10-14	4	1.6-1.8	2	0	1	0	**1.70**	$(70,71)$	**1.6**	$(4,7)$	0	0	0.18
10-14	4	1.6-1.8	1	1	2	1	1.72	$(67,78)$	1.6	$(1.1,2.1)$	6	$(-18,31)$	0.38

$$\mathcal{L}_3(3)$$

ΔM	E	δW	n_r	n_i	m_r	m_i	W_c	CI(W_c)	ν	CI(ν)	y	CI(y)	p
12-18	0	4.7–4.875	2	0	1	0	**4.79**	$(78,80)$	**1.6**	$(4,8)$	0	0	0.43
12-18	0	4.7–4.875	2	1	1	2	4.79	$(78,80)$	1.6	$(4,8)$	8284	$(0,1)$	0.11

表 5.1: Critical parameters at the MIT for $\mathcal{L}_3(n)$, $n = 1, 2$ and 3. The columns are denoting the system width M, fixed E (or W), the range of W (or E). The expansion orders n_r, n_i, m_r, m_i are listed as well as the obtained critical disorders W_c (or energies E_c), their 95% confidence intervals (CI), the critical exponent ν, its CI, the irrelevant parameter y, its CI, and the goodness of fit probability p. The confidence interval are given with one significant decimal. For instance, $1.6(4, 8)$ marks that the CI is $(1.4, 1.8)$.

Chapter6   Unconventional delocalization in a family of three-dimensional Lieb lattices

6.1   Introduction

The correlation effect in disorder systems has always been a hot topic. As the results [7] predicted by Abrahams et al. that the localization properties are strongly depend on the lattice dimensionality, the type of lattice geometry considered, as well as the nature of the potential considered [2, 3, 115], and it claims that all states are localized for uncorrelated low dimensional disorder systems. While, a transition from delocalized to localized phase may also occur in $1D$ chains when correlated disordered potentials are considered [116, 117].

Spatial disorder, however, is not the only ingredient that can lead to wave localization phenomena in lattices. In translationally invariant networks, one of the most intensely studied frameworks for eigenstates localization is the case of flat band lattices – *i.e.* networks where destructive interference results in families of macroscopically degenerate single-particle eigenstates localized within a finite number of lattice sites [118–120]. These states, called *compact localized states* (CLS), form a non-dispersive (hence, *flat*) Bloch band $E_j(\mathbf{k}) = $ const. in the energy spectrum which is independent on the momentum $\mathbf{k}$. The CLS have been discussed as potential candidates for information storage applications [121]. However, they are typically sensitive to perturbations. Uncorrelated onsite disorder in most cases lifts the existence of CLS irrespective of the disorder strength and induces wave localization in flat band lattices [10, 21, 22, 26, 68, 100, 122, 123]. In certain cases, however, local symmetries within flat band lattices suggest local correlations in the onsite disorder which result in anomalous localization features – as shown in Refs. [24, 99] for disorder and quasiperiodic potentials in $1D$ and $2D$ sample lattices.

In this work we study the impact of local ordering correlations in a family of $3D$ extended Lieb lattices. These lattice systems, in presence of uncorrelated spatial disorder, exhibit energy-dependent transitions between localized to delocalized phase as showed in our previous results [69]. By exploiting local symmetry in the family of Lieb lattices, we introduce a mix of correlated order and disorder within the lattice. This mix of local order and disorder preserves the existence of the degenerate CLS and induces an effective projection of the non-degenerate states onto the CLS [122]. The projection yields the existence of delocalized states existing mostly within the locally ordered sub-lattice of the systems spanned by the CLS, whose energies lie closer to the macroscopic degeneracy as

the strength of the disorder increases. Ultimately, the persistence of these extended states results in a divergent profile of the mobility edge separating delocalized and localized phases, unlike what was found in Ref. [69] for uncorrelated disorder. Furthermore, we observe that this correlated ordering in the regime of weak disorder induces an "inverse" change from localized to delocalized eigenstates for energies close to the macroscopic degeneracies.

6.2   Models

We consider a parametric family of three-dimensional Lieb lattices $\mathcal{L}_3(n)$, $n = 1, 2, 3, 4$ and the schemes are shown in Fig. 2.1. Based on the tight binding method, the Hamiltonian is

$$H = \sum_{\vec{r}} \varepsilon_{\vec{r}} |\vec{r}\rangle\langle\vec{r}| - \sum_{\vec{r} \neq \vec{r}\prime} t_{\vec{r}\vec{r}\prime} |\vec{r}\rangle\langle\vec{r}\prime| \ , \tag{6.1}$$

where the set of $|\vec{r}\rangle$ indicates the orthonormal Wannier states corresponding to electrons located at sites $\vec{r} = (x, y, z)$ of the Lieb lattice $\mathcal{L}_3(n)$ and $\varepsilon_{\vec{r}}$ is the onsite potential [68]. Here, we consider *locally correlated potentials* $\varepsilon_{\vec{r}}$ which neither destroy the existence of CLS nor renormalize their degeneracy while simultaneously offering the possibility of localization for non-CLS states. To ensure this for any number n of Lieb sites, the simplest choice is to set the onsite potential of Lieb sites $\varepsilon_{\vec{r}}^{(L)}$ constant, *i.e.* $\varepsilon_{\vec{r}}^{(L)} \equiv 0$, while introducing a spatially varying disorder potential on the cube sites $\varepsilon_{\vec{r}}^{(c)}$ via uncorrelated uniform random numbers with disorder strength W such that $\varepsilon_{\vec{r}}^{(c)} \in \left[-\frac{W}{2}, \frac{W}{2}\right]$. As usual, we set the hopping integrals $t_{\vec{r},\vec{r}\prime} \equiv 1$ for nearest-neighbor sites $\vec{r}$ and $\vec{r}\prime$ as energy scale and $t_{\vec{r},\vec{r}\prime} \equiv 0$ otherwise.

6.3   Results

In this chapter, we focus mainly on the first two representative cases of the lattice family, $\mathcal{L}_3(1)$ and $\mathcal{L}_3(2)$. Note that, due to approximate mirror symmetry of the energy spectrum around $E = 0$ (which is exact when $\varepsilon_{\vec{r}}^{(L)} = 0$), we show results only for positive energies $E \geq 0$, although we have computed data for the full spectrum.

6.3.1   For Lieb lattice $\mathcal{L}_3(1)$

In this first case, namely $\mathcal{L}_3(1)$, a single macroscopic degeneracy of CLS exists at $E = 0$. We therefore begin to study the localization lengths Λ_M via TMM at energy

$E \neq 0$, in order to avoid possible complications of the numerical schemes due to the degeneracy.

1. Existence of localization transitions

   These curves show a stable intersection point, indicating the existence of a critical disorder W_c separating metallic from localized phases. Such critical transition is extracted by FSS shown in Fig. 6.1(b,c), yielding $W_c = 16.38(2)$ – which incidentally is roughly the same as the standard Anderson transition $W_c = 16.590(12)$ for a cubic lattice at $E = 0$ [103]. However, the same computation repeated closer to the macroscopic degeneracy – namely at $E = 0.4$, as shown in Fig. 6.1(d-f) – yields a substantially higher critical transition value $W_c \approx 40.29(7)$ than the value for $E = 1$ [**?**].

   In Fig. **??**(a) we show the localization length Λ_M at energy $E = 1$ for M^2 ranging from 16^2 to 22^2 computed with high precision. These two results seem to hint towards a divergence of W_c as the energy approaches the macroscopic degeneracy at $E = 0$. Consequently, we systematically estimate the critical transition $W_c(E)$ within the interval $0 < E \leq 1.5$ – *i.e.* strictly different than $E = 0$ – for small system sizes $M = 6, 8$ via TMM with maximal convergence error of $\leq 0.5\%$. The resulting curve is shown in Fig. 6.2(a) with white circles connected by a solid line within the yellow region – confirming the divergence of $W_c(E \to 0)$.

2. Spectral characterization of the localization transitions

   To further validate the behaviour of $W_c(E)$ and to compute the overall phase-diagram, we look at the spectral properties of the Hamiltonian (2.3). Details on the computations are reported in the caption of Fig. 6.2. The DOS – shown in Fig. 6.2(a) for $E > 0$ and different disorder strengths W – exhibits intriguing phenomena close to the macroscopic degeneracy level $E = 0$ in both the weak and the large W regimes. Namely, we observe (i) a depletion of the DOS at $E \leq 1$ for $W \to 0$, and (ii) a strong enhancement of the DOS at $E \leq 1$ for $W \to \infty$.

   The former observation (i) is related to the fact that in the clean case $W = 0$ the flatband $E = 0$ is touching the remaining dispersive bands via conical intersections – with consequent decrease of the DOS as $E \to 0$, as discussed in Ref. [69]. The latter observation (ii) instead follows from the fact that for large W it becomes energetically favorable for eigenstates to populate the unperturbed Lieb sites (where the CLS live) rather than the disordered cube sites. This is confirmed in Fig. 6.3 where we show the projected norm of eigenstates at the Lieb sites (red colors) and

the cube sites (blue colors) as function of the energy E for different disorder strength W (shown with different symbols).

What appears is an increase of the relative norm in the Lieb sites (and complementary a decrease of the relative norm in the cube-sites) as $|E| \to 0$ – trends which are enhanced as the disorder W increases. In particular, for strong disorder $W = 50$, the norm of the eigenstates for $E \ll 1$ is almost exclusively located at the Lieb sites. Such effective projection of the eigenstates at $E \neq 0$ on the set of CLS at $E = 0$ results in lowering the energies of a large fraction of states close to the macroscopic degeneracy – and, consequently, the strong enhancement of the DOS for $E \ll 1$ as $W \to \infty$. Note that in these calculations we have excluded those eigenstates with $|E| \leq 10^{-4}$, removing the degenerate CLS. However, close to $E = 0$, each of the different potential realizations yields a single eigenstate at $E \sim 10^{-2}$, which is an accidental degeneracy following from the $\langle \varepsilon_{\vec{r}}^{(c)} \rangle_{N \to \infty} \to 0$ [89]. Such eigenstates result in the outlier points close to $E = 0$ in Fig.6.3.

3. Spectral gap ratio statistics

The diverging behaviour of $W_c(E)$ shown in Fig. 6.2(a) had been estimated via TMM. In order to find further support for this behaviour, we now use the independent spectral gap ratio statistics for $\langle r \rangle$ to compute the full phase-diagram for $\mathcal{L}_3(1)$ via sparse-matrix diagonalization. In Fig. 6.2(b) we show the $\langle r \rangle$ for $L = 4 \times 20^3$ as function of the E and W. The results convincingly confirm the diverging trend for the transition curve $W_c(E)$ from extended with $\langle r \rangle \sim \langle r \rangle_{\mathrm{Sur}}$ (~ 0.53) to localized with $\langle r \rangle \sim \langle r \rangle_{\mathrm{Poi}}$ (~ 0.38) as $E \to 0$ for $W \gtrsim 10$. In particular, the r-value-based transition line shows strong agreement with the transition curve obtained from the scaling behaviour of localization lengths Λ_M (shown in Fig. 6.2(b) with white solid line). Furthermore, we observe that close to $E = 0$ in the small W regime, the $\langle r \rangle$ drops from $r \sim 0.529$ – a decrease occurring in correspondence to the depletion of the DOS.

We first have a more in-depth look at the localization-to-delocalization transition (white solid line in Fig. 6.2(b)) when starting from high E and/or W values. Analogously with the TMM, we fix energy to $E = 1$ and study the behaviour of $\langle r \rangle (W)$ for various system sizes N. In Fig. 6.4(a-c) we show FSS results for $\langle r \rangle$ values for N ranging from 18 to 24 around the expected transition value $W_c \approx 16.4$.

We find that the critical disorder $W_c \approx 16.36(2)$ as computed with the r-statistics is in excellent agreement with the critical value $W_c = 16.38(2)$ obtained via TMM. Furthermore, as detailed in Table 6.1, the FSS results are in agreement with the

conventional critical exponents for the 3D Anderson transition [6, 103]. Indeed, the critical exponent $\nu = 1.51$ is also in agreement with the TMM result. Last, we see in Fig. 6.4(a) that the value $\langle r \rangle (W_c) = 0.5145$, which is one of the contour lines highlighted in Fig. 6.4(b), separates localized from extended behaviour, again emphasizing the consistency of our results.

These measurements are further confirmed by the results obtained via the spectral statistics based on the $|z|$ measure introduced in Refs. [80, 81]. In Fig. 6.4(d) we plot the $\langle |z| \rangle (W)$ data and corresponding FSS lines for N ranging from 16 to 24 at $E = 1$, again around the expected $W_c \approx 16.4$. In Fig. 6.4(e-f) we show the associated scaling function and scaling parameter. The results agree with those obtained via r-statistic, albeit with larger error bars, giving a critical transition at $W_c \approx 16.40(3)$. Full details about the finite-size scaling(FSS) and the scaling parameters of Λ_M, r-values and $|z|$-values are reported in Table. 6.1. In particular, we note that FSS is possible even without having to take into account irrelevant corrections to scaling. We have also performed FSS with irrelevant corrections, and found fits with acceptable χ^2 statistics. However, already the FSS without irrelevant corrections is stable, i.e. independent of the chosen disorder range, and robust, i.e. W_c and ν values to not violate their error boundaries when increasing the expansion orders n_r, m_r. We therefore only show the results for the latter case in Table 6.1. This is also the case for the FSS results from the TMM data.

4. The "inverse transition" at small E and W values

As briefly mentioned above when discussing Fig. 6.2, the region of $E \lesssim 1$ and $W \lesssim 10$ for the DOS and phase diagram of $\mathcal{L}_3(1)$ indicates a small DOS $\sim 10^2$ as well as small $\langle r \rangle \sim 0.4$ values. These observations suggest that the regime again corresponds to localized states, and, consequently, the system might in fact exhibit an "inverse" Anderson transition whereby upon increasing W at some fixed $0 < E \lesssim 1$ one can observe a transition back into the extended regime.

In order to study this possibility in detail, we choose $E = 0.4$ and again compute localization lengths Λ_M via TMM as well as $\langle r \rangle$ statistics as function of W for increasing bar width M or system size N, respectively, aiming for a maximal convergence error of 0.1% for TMM. In Fig. 6.5, we show the resulting data. The error bars are mostly within symbol size, highlighting the reliability of the data.

We find that the localization lengths Λ_M shown in Fig. 6.5(a) do indeed exhibit the expected opposite dependency on M. For $W \leq 1$ increasing M leads to an decrease of Λ_M while for $W \gtrsim 15$, increasing M increases Λ_M, at least for the larger sizes

						Reduced localization length Λ_M				
M	E	δW	n_r	m_r	W_c	CI(W_c)	ν	CI(ν)	p
20,22,24,26	0.4	39.0-41.5	2	1	***40.29***	[40.16, 40.42]	***1.50***	[1.28, 1.73]	0.52
20,22,24,26	0.4	39.0-41.5	3	1	40.29	[40.15, 40.43]	1.51	[1.27, 1.75]	0.46
20,22,24,26	0.4	39.0-41.5	3	2	40.35	[40.14, 40.56]	1.51	[1.26, 1.76]	0.44
20,22,24,26	0.4	39.0-41.5	4	1	40.30	[40.16, 40.44]	1.51	[1.27, 1.75]	0.43
Averages:					40.31(4)		1.51(6)		
M	E	δW	n_r	m_r	W_c	CI(W_c)	ν	CI(ν)	p
16,18,20,22	1	15.9-16.8	2	1	***16.38***	[16.36, 16.41]	***1.50***	[1.37, 1.63]	0.22
16,18,20,22	1	15.9-16.8	3	1	16.39	[16.36, 16.41]	1.51	[1.38, 1.65]	0.19
16,18,20,22	1	15.9-16.8	3	2	16.41	[16.38, 16.45]	1.50	[1.37, 1.63]	0.37
16,18,20,22	1	15.9-16.8	4	1	16.39	[16.36, 16.42]	1.51	[1.37, 1.65]	0.18
Averages:					16.39(1)		1.51(4)		
					r-Values				
N	E	δW	n_r	m_r	W_c	CI(W_c)	ν	CI(ν)	p
18,20,22,24	1	16.0-16.7	2	1	***16.36***	[16.32, 16.40]	***1.51***	[1.21, 1.80]	0.56
18,20,22,24	1	16.0-16.7	3	1	16.36	[16.31, 16.40]	1.54	[1.22, 1.86]	0.54
18,20,22,24	1	16.0-16.7	3	2	16.37	[16.32, 16.42]	1.55	[1.22, 1.88]	0.53
18,20,22,24	1	16.0-16.7	4	1	16.36	[16.31, 16.40]	1.54	[1.22, 1.86]	0.51
Averages:					16.36(2)		1.54(9)		
					$|z|$-Values				
N	E	δW	n_r	m_r	W_c	CI(W_c)	ν	CI(ν)	p
16,18,20,22,24	1	16.0-16.7	2	1	***16.40***	[16.34, 16.45]	***1.35***	[1.01, 1.68]	0.67
16,18,20,22,24	1	16.0-16.7	3	1	16.40	[16.34, 16.45]	1.49	[1.10, 1.88]	0.75
16,18,20,22,24	1	16.0-16.7	3	2	16.40	[16.34, 16.47]	1.47	[1.08, 1.85]	0.73
16,18,20,22,24	1	16.0-16.7	4	1	16.40	[16.35, 16.46]	1.46	[1.09, 1.84]	0.75
Averages:					16.40(2)		1.44(10)		

表 6.1: Critical parameters of the traditional (standard) Anderson transition for $\mathcal{L}_3(1)$ with reduced localization length Λ_M, r- and $|z|$-values as indicator, respectively. The columns give the size of the system (the width M of the cross section of a TMM bar and of the side length N of a cube for Λ_M and r- and $|z|$-values, respectively), fixed E, range of W, FSS expansion orders n_r, m_r and the resulting critical disorders W_c, their 95% confidence intervals (CI), the critical exponent ν, and its CI, and the goodness of fit probability p in order. The averages contain the mean of the three preceding W_c and ν values, with standard error of the mean in parentheses. The bold W_c and ν values highlight the fits used as examples in Fig. 6.1 and Fig. 6.4.

studied. Hence there seems to be indeed a change from localized behaviour at small W to extended behaviour at larger W. However, we also observe considerable non-monotonic behaviour, e.g. for $M = 14$, and a complete absence of a clearly defined crossing point to serve as estimate for W_c. The behaviour cannot be captured by the standard FSS techniques and the required "corrections to scaling" are clearly beyond what one can expect a systematic modelling of irrelevant corrections to achieve [6,124]. Nevertheless, using the crossings defined by considering just system sizes $M^2 = 6^2$ and $M^2 = 8^2$ from Fig. 6.5(a), we find that the resulting "phase boundary" faithfully follows the trend for the contours of DOS and $\langle r \rangle$ values as shown in Fig. 6.2(b). Similarly, the $\langle r \rangle$ values reach $\langle r \rangle_{\text{Sur}}$ when $W \gtrsim 6$. For $W \lesssim 2$, the truly localized $\langle r \rangle_{\text{Poi}}$ (~ 0.38) is not attained, but at least we find that $\langle r \rangle$ drops significantly to ~ 0.45. Again as in the case of the TMM data, no clear, system size-independent transition point emerges for the system sizes studied by us.

In summary, the results at $E = 0.4$ indicate the presence of a non-conventional "inverse transition"al change from localized to extended regime as W increases close to the macroscopic degeneracy of CLS. This seems similar to the proposed "inverse" transition reported in a 3D all-band-flat network in the regime of weak uncorrelated disorder [25, 101].

For Lieb models $\mathcal{L}_3(n)$ with $n \geq 2$

We now briefly sketch the situation for the other Lieb lattices $\mathcal{L}_3(2)$, $\mathcal{L}_3(3)$ and $\mathcal{L}_3(4)$. For $\mathcal{L}_3(2)$, we show DOS, $\langle r \rangle$-based phase diagram and TMM-based approximate phase boundaries in Fig. 6.6. The CLS at $E \pm 1$ are not explicitly shown in the figure but clearly visible by the behaviour of the non-CLS states around them. There is an identical signature of depletion of states, as for $\mathcal{L}_3(1)$, in the small W region when $E \rightarrow 1^{\pm}$. On the other hand, for both large E and W the DOS depletes and the $\langle r \rangle$-values indicate localized behavior. Two extended regions emerge, both of which tend to lie close to the region of the CLS when $W \gtrsim 20$. These results are supported again from estimates based on TMM for $M^2 = 6^2$ and $M^2 = 8^2$. We note that due to the absence of CLS for $E = 0$, we can indeed observe the usual change from extended to localized behaviour upon increasing W with $W_c \sim 16$ marking the boundary between both regimes. We can also find the "inverse" behaviour again, e.g. for $\mathcal{L}_3(2)$ for $1 \lesssim E \lesssim 2$, where increasing W leads to a change from localized to delocalized behaviour.

This trend continues for $\mathcal{L}_3(3)$ and $\mathcal{L}_3(4)$ as shown in Fig. 6.7: the originally dispersive bands, when $W = 0$, move their states closer to the CLS upon increasing W, reducing the DOS for energies further from the CLS-energies and eventually localizing

these. A sizable part of the spectrum moves closer to the CLS-energies, with states being moved onto the Lieb sites as shown for $\mathcal{L}_3(1)$.

1. Projected probabilities beyond $E \geq 1.5$ and participation ratios

   In Fig. 6.8 we show the same data as in Fig. 6.3, but now for $E \geq 0$. We find that the projected probabilities cross when $E \sim 2.45$. This happens at all Ws that we have studied, *i.e.* up to $W = 100$. Closer investigation reveals that about 50% of all $4 \times N^3$ possible states are CLS, 25% get shifted towards the CLS energies when W increases, while the remaining 25% localize and spread out into the full range of the spectrum. The relative participation numbers, *i.e.* $P = 1/\sum_{l=1}^{L_{\max}} |\psi(\vec{r}_l)|^4/(L_{\max})$ as shown in panel (b) of Fig. 6.8, indicate that indeed appreciable P are only observed close to the CLS energy $E = 0$ for $\mathcal{L}_3(1)$. Note that here $L_{\max}$ is the number of sites corresponding to cube and Lieb sites, *i.e.* N^3 and $3nN^3$, respectively, for $\mathcal{L}_3(n)$.

2. Phase diagrams of DOS and r-values for $\mathcal{L}_3(3)$ and $\mathcal{L}_3(4)$

   We plot DOS, the $\langle r \rangle$-based phase diagram and TMM-based approximate phase boundaries in Fig. 6.7 for $\mathcal{L}_3(3)$ and $\mathcal{L}_3(4)$. The CLS at $E \pm 1$ are not explicitly indicated in the figures but clearly visible by the behaviour of the non-CLS states around them. There is an identical signature of depletion of states, as for $\mathcal{L}_3(1)$ and $\mathcal{L}_3(2)$, in the small W regions when E approaches the CLS energies. For larger W, clear areas of localization behaviour emerge except for energies close to the CLS energies where even very strong disorder does not appear to suppress delocalized behaviour for the system sizes studied here. We can also find the "inverse" behaviour again in various energy regions although better energy resolution would be needed to reproduce fine details such as given, e.g., for $\mathcal{L}_3(1)$ in Fig. 6.2.

6.3.2   Conclusion

In this paper, we considered the disorder $\varepsilon_{\mathbf{r}}^c$, together with the *order* $\varepsilon_{\mathbf{r}}^L = 0$, retains the distinction between CLS and the rest of the states, leaving the CLS are unchanged for any W. The converse is manifestly not the case: about half of the non-CLS states for, e.g., $\mathcal{L}_3(1)$ get pushed in energy close to the energy of the CLS and become evermore concentrated on the Lieb sites. This leads to an accumulation of DOS near the CLS energies and, ultimately, to the existence of seemingly extended states even for very strong W for all the $\mathcal{L}_3(1)$ to $\mathcal{L}_3(4)$ probed here.

For the transition from extended to localized behaviour upon increasing E or W in the phase diagrams we find that the critical properties can be extracted as usual via

FSS with critical exponent ν compatible with the usual value of the cubic Anderson lattice [6, 103]. Hence, although the changes to the phase diagrams are drastic, the universal nature of the transition at this phase boundary does not change.

However, when instead decreasing E and W from the extended regimes, we do not see a clear signature of a transition as function of a single critical parameter strength. Rather, it appears that the changes of phase behaviour do no follow traditional scaling or require much larger system sizes to reach the scaling regime.

Overall, the model presents a situation where upon increasing W, the CLS are retained while non-CLS states are forced to become more and more CLS-like, in terms of energy as well as in terms of spatial location. As the CLS states are among a class of states that might become relevant for future information storage devices. Our result hence suggest a way in which disorder is not detrimental to such an application, but rather enhances the stability of the CLS.

6.4 Conclusion

In this paper, we considered the disorder $\varepsilon_{\mathbf{r}}^c$, together with the *order* $\varepsilon_{\mathbf{r}}^L = 0$, retains the distinction between CLS and the rest of the states, leaving the CLS are unchanged for any W. The converse is manifestly not the case: about half of the non-CLS states for, e.g., $\mathcal{L}_3(1)$ get pushed in energy close to the energy of the CLS and become evermore concentrated on the Lieb sites. This leads to an accumulation of DOS near the CLS energies and, ultimately, to the existence of seemingly extended states even for very strong W for all the $\mathcal{L}_3(1)$ to $\mathcal{L}_3(4)$ probed here.

For the transition from extended to localized behaviour upon increasing E or W in the phase diagrams we find that the critical properties can be extracted as usual via FSS with critical exponent ν compatible with the usual value of the cubic Anderson lattice [6, 103]. Hence, although the changes to the phase diagrams are drastic, the universal nature of the transition at this phase boundary does not change. However, when instead decreasing E and W from the extended regimes, we do not see a clear signature of a transition as function of a single critical parameter strength. Rather, it appears that the changes of phase behaviour do no follow traditional scaling or require much larger system sizes to reach the scaling regime.

Overall, the model presents a situation where upon increasing W, the CLS are retained while non-CLS states are forced to become more and more CLS-like, in terms of energy as well as in terms of spatial location. As the CLS states are among a class of states that might become relevant for future information storage devices. Our re-

sult hence suggest a way in which disorder is not detrimental to such an application, but rather enhances the stability of the CLS. While solid-state devices with the chosen highly-correlated disorder/order distribution appear unlikely to become readily available soon, a much simpler route could be via cold atoms in optical lattices [58, 125, 126] or in photonic band-gap systems [59–63, 127] where single-site potential modulation has become routine [120]. In such experimental and hence finite set-ups, it may be that the relevance of our finite size results is even more important than any large scale limit. Last, it should be clear that an investigation of the influence on many-body interaction, in the presence of the CLS-preserving disorder considered here, should be most insightful.
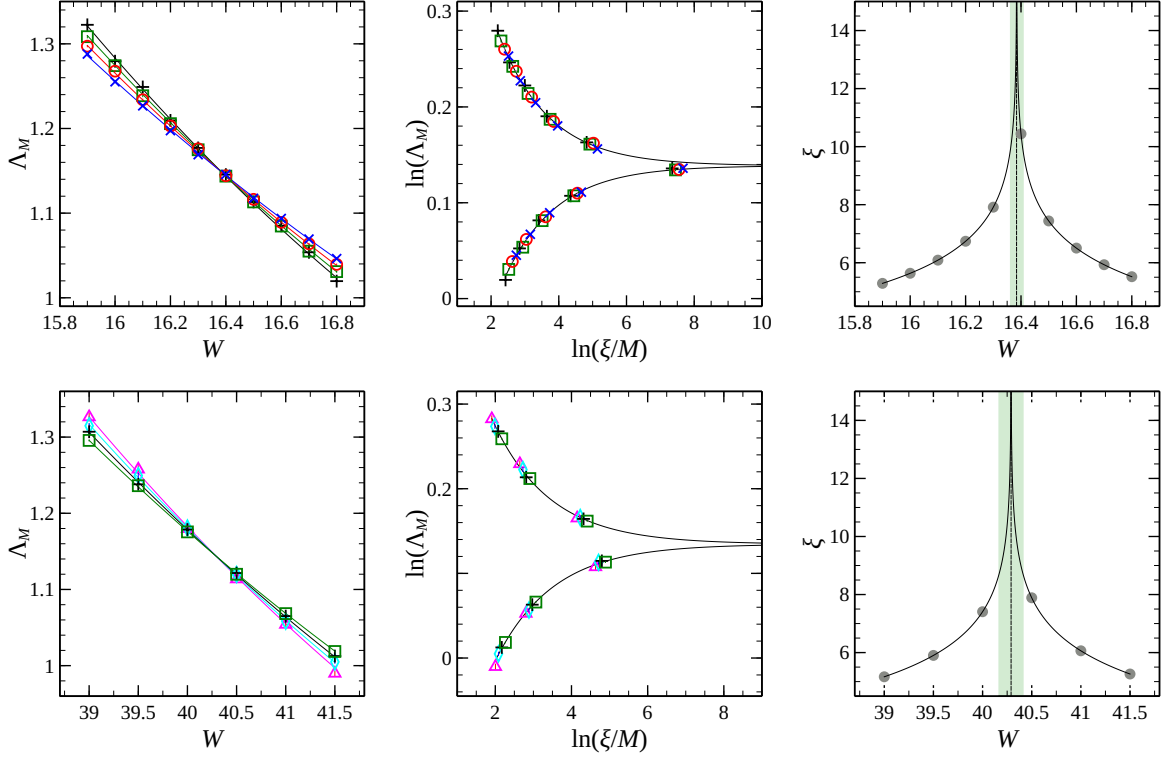
图 6.1: Finite-size scaling of the reduced localization lengths Λ_M for $\mathcal{L}_3(1)$ at large W regimes with $E = 1$ (a,b,c) and $E = 0.4$ (d,e,f), respectively. The bar area M^2 ranges from 16^2 (blue $\times$), 18^2 (red $\bigcirc$) with maximal convergence error $\leq 0.1\%$, to 20^2 (green $\square$), 22^2 (black $+$) with maximal convergence error $\leq 0.22\%$, and to 24^2 (cyan $\diamond$) and 26^2 (magenta $\triangle$) with maximal convergence error $\leq 0.5\%$. The reduced localization length Λ_M versus the disorder strength W on the cube sites, and the fits to the data showed in solid line with expansion coefficients $n_r = 2$ and $m_r = 1$ for both graphs are present in (a) and (d). The (b) and (e) give double logarithmic plot of scaling function Λ_M and ξ/M with scaled data points. The scaling parameter ξ as a function of cube disorder W and the scaled data points are shown in (c) and (f), with the vertical lines indicating the estimated W_c values and their CI intervals in (green) shade. Error bars are within the symbol size. Details of the scaling results are given in Table 6.1.
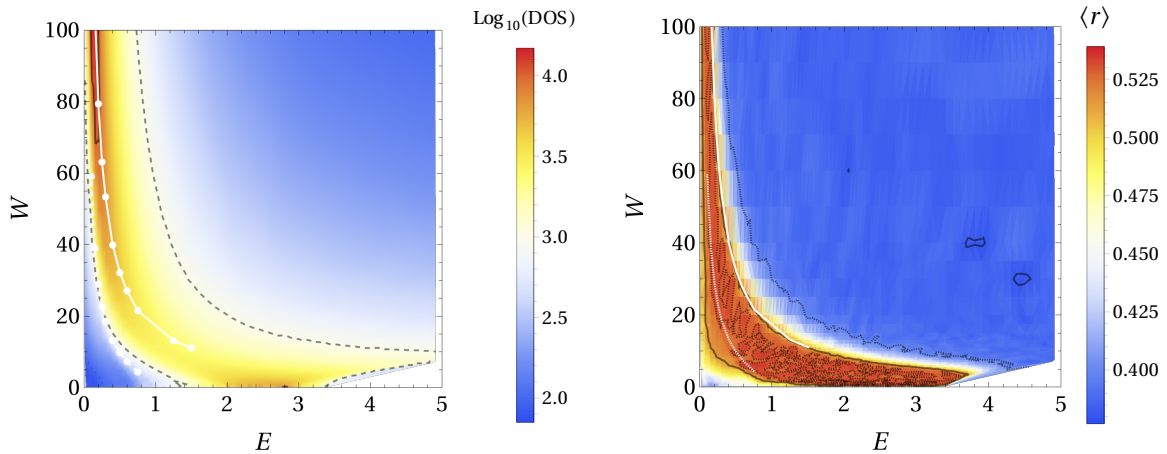
图 6.2: Energy E and disorder W dependant (a) DOS and (b) r-values for $\mathcal{L}_3(1)$. The diagrams have been obtained for system sizes $L = 4 \times 20^3$ and at least 100 independent potential configurations for each (E, W) pair. For each such configuration, up to 100 energy eigenvalues around the target energy E have been computed. The minimal energy spacing is $\Delta E = 0.05$ while the minimal disorder spacing $\Delta W = 0.1$; adaptively chosen 3300 individual (E, W) pairs contribute to the computed DOS and r-value density plots. The flat-band states at $E = 0$ ($\leq 10^{-10}$) are not shown in both panels for clarity. The dark lines for (a) denote contours of 10^3 (dashed) and 10^4 (solid) states, while for (b) the lines in the red-shaded region correspond to $\langle r \rangle = 0.53$ (dashed), 0.5145 (solid) and in the blue-shaded region, they denote $\langle r \rangle = 0.4$ (dashed) and 0.38 (solid). The white lines in (a) and (b) denote estimates of the transitions obtained by small-M TMM with the 2 different lines corresponding to the crossings of Λ_M values between $M = 6$ and $M = 8$ from localized-to-delocalized (solid) and delocalized-to-localized (dashed) behaviour upon decreasing W at constant E. In (a) these small-M estimates for (E_c, W_c) are given as white circles.
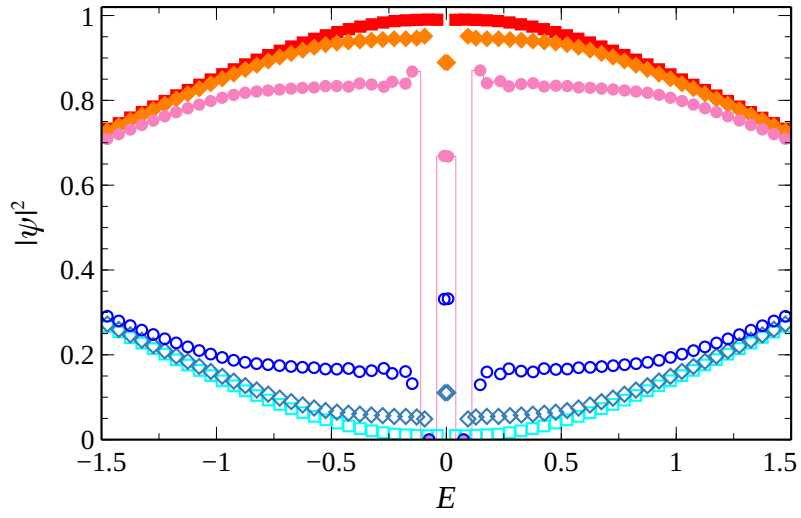
图 6.3: Projected probabilities $|\psi(r)|^2$ for cube sites (blue colors, open symbols) and Lieb sites (red colors, filled symbols) with disorders $W = 10$ ($\circ$), 20 ($\diamond$) and 50 ($\square$) for $\mathcal{L}_3(1)$. The line for Lieb sites with $W = 10$ is given to highlight that the data points represent averages for 144 potential configurations with energy resolution $\Delta E = 0.05$. The system size in all cases is $L = 4 \times 20^3$.
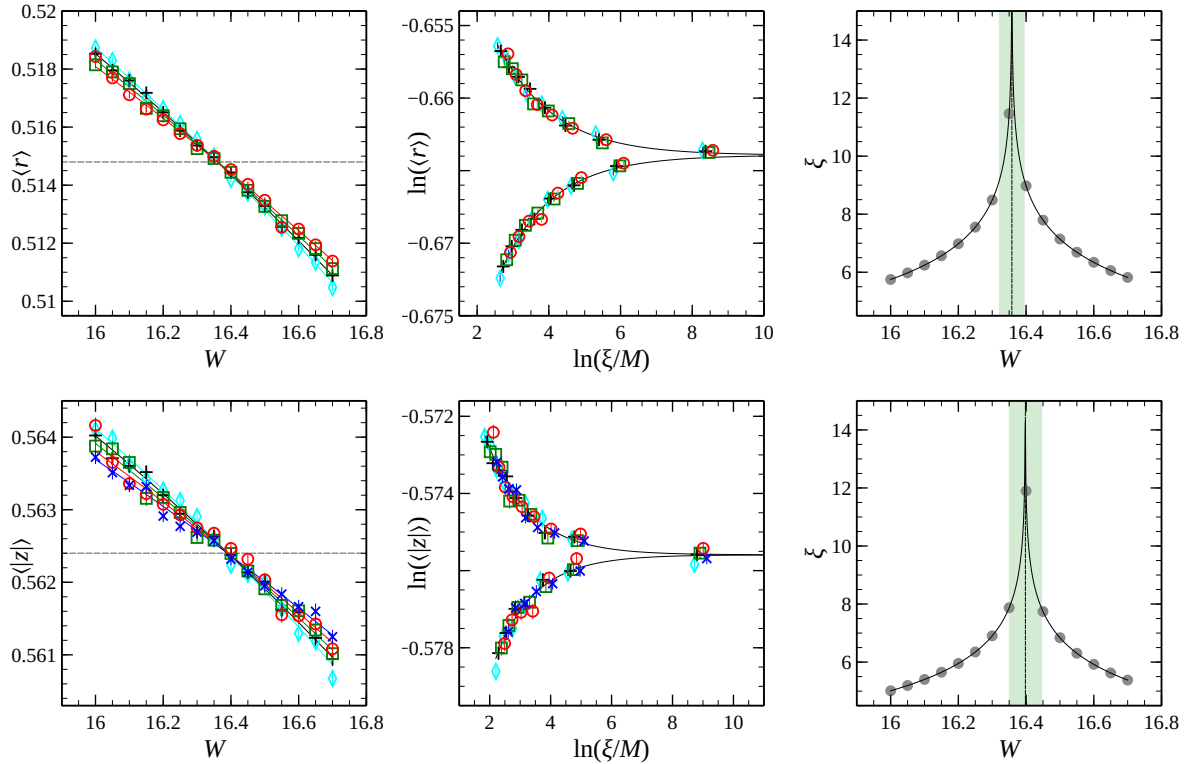
图 6.4: Finite size scaling results of the (a–c) r-values and (d–f) z-values for $\mathcal{L}_3(1)$ in the high W region at $E = 1$, respectively. The system sizes $L = 4 \times N^3$ are from $N = 16$ (blue ×), 18 (red ◯), 20 (geen □), 22 (black +), and to 24 (cyan ◇). For each N and W, 10000 different potential configurations have been calculated and for each we include up to 100 energy eigenvalues around the target energy E in the computing $\langle r \rangle$ and $\langle |z| \rangle$. Panel (a) and (d) show the $\langle r \rangle$-values ($\langle |z| \rangle$-values) versus W data and the fits to the data, as given in Table 6.1 with expansion coefficients $n_r = 2$ and $m_r = 1$, are marked with solid lines. Panels (b) and (e) give double logarithmic plots of scaling function r-values(z-values) versus ξ/M with scaled data points. The scaling parameter $\xi(W)$ is shown in panels (c) and (f). The vertical lines indicate the W_c values and the shaded region their CI. Error bars as shown in panels (a), (b), (d) and (e) are mostly within symbol size. The horizontal lines in panels (a) and (d) denote the values $\langle r \rangle = 0.5148$ (with CI $[0.5143, 0.5153]$) and $\langle |z| \rangle = 0.5624$ (with CI $[0.5621, 0.5627]$) obtained at W_c.
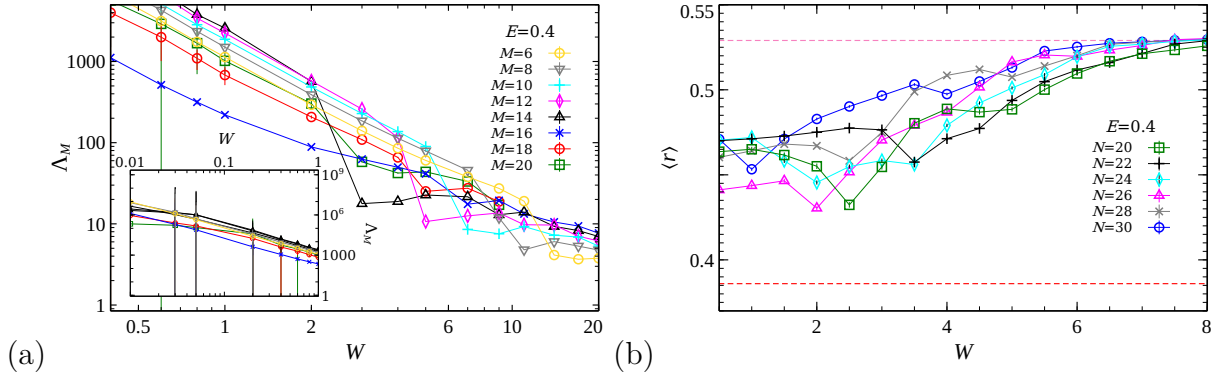
图 6.5: (a) Reduced localization length Λ_M versus disorder W at small disorder for $\mathcal{L}_3(1)$ at $E = 0.4$ and TMM bar area $M = 6^2$ (yellow ◯), 8^2 (grey ▽), 10^2 (cyan +), 12^2 (magenta ◇) and 14^2 (black △), 16^2 (blue ×), 18^2 (red ◯), 20^2 (green □). The error bars are all shown, and within symbol size. The inset focuses on the small W regime $0.01 \leq W \leq 1$. (b) r-values versus disorder W at $E = 0.4$ for system size $L = 4 \times N^3$ with $N = 20$ (green □), 22 (black +), 24 (cyan ◇) and 26 (magenta △), 28 (grey ×), 30 (blue ◯) with 10000 potential realizations for each (N, W) pair. The horizontal dashed green (red) line represents the extended (localized) regime with $\langle r \rangle_{\mathrm{Sur}}$ ($\langle r \rangle_{\mathrm{Poi}}$). All other lines are guides to the eye, only.
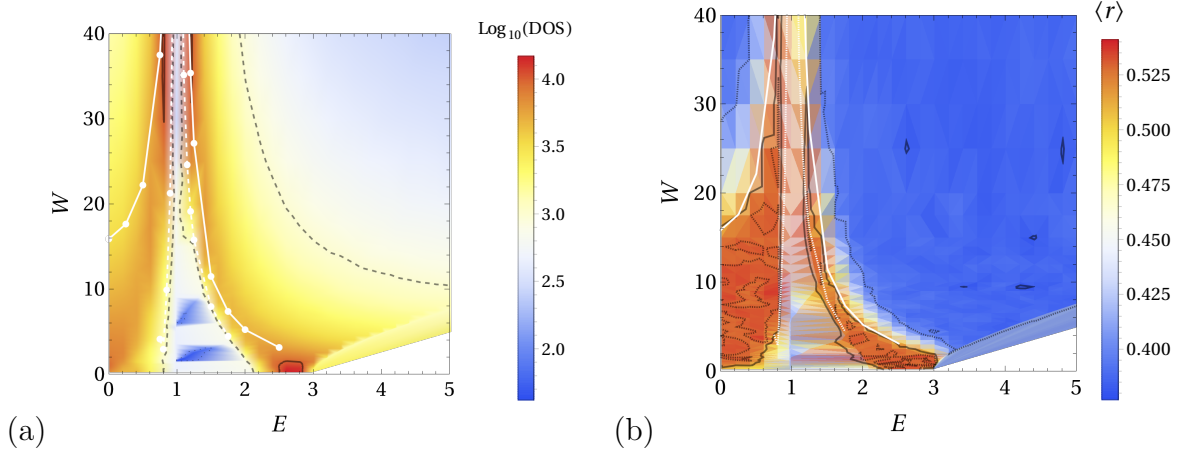

图 6.6: Energy E and disorder W dependant (a) DOS and (b) r-values for $\mathcal{L}_3(2)$. Both panels have been computed with the same parameters as in Fig. 6.2, except that the minimal energy spacing increases to $\Delta E = 0.2$, giving in total 1581 individual (E, W) pairs. The flat-band states at $E = 1$ are not shown in both panels for clarity. The dark lines are as in Fig. 6.2 in (a) given by 10^3 (dashed) and 10^4 (solid) states, while for (b) they correspond to $\langle r \rangle = 0.53$ (dashed), 0.5145 (solid) in the red region, $\langle r \rangle = 0.4$ (dashed) and 0.38 (solid) in the blue region. Also as in Fig. 6.2, the white lines in (a) and (b) denote estimates of the phase boundaries obtained by small-M TMM with the 2 different lines corresponding to the crossings of Λ_M values between $M = 6$ and 8 from localized-to-delocalized (solid) and delocalized-to-localized (dashed) behaviour upon decreasing W at constant E.
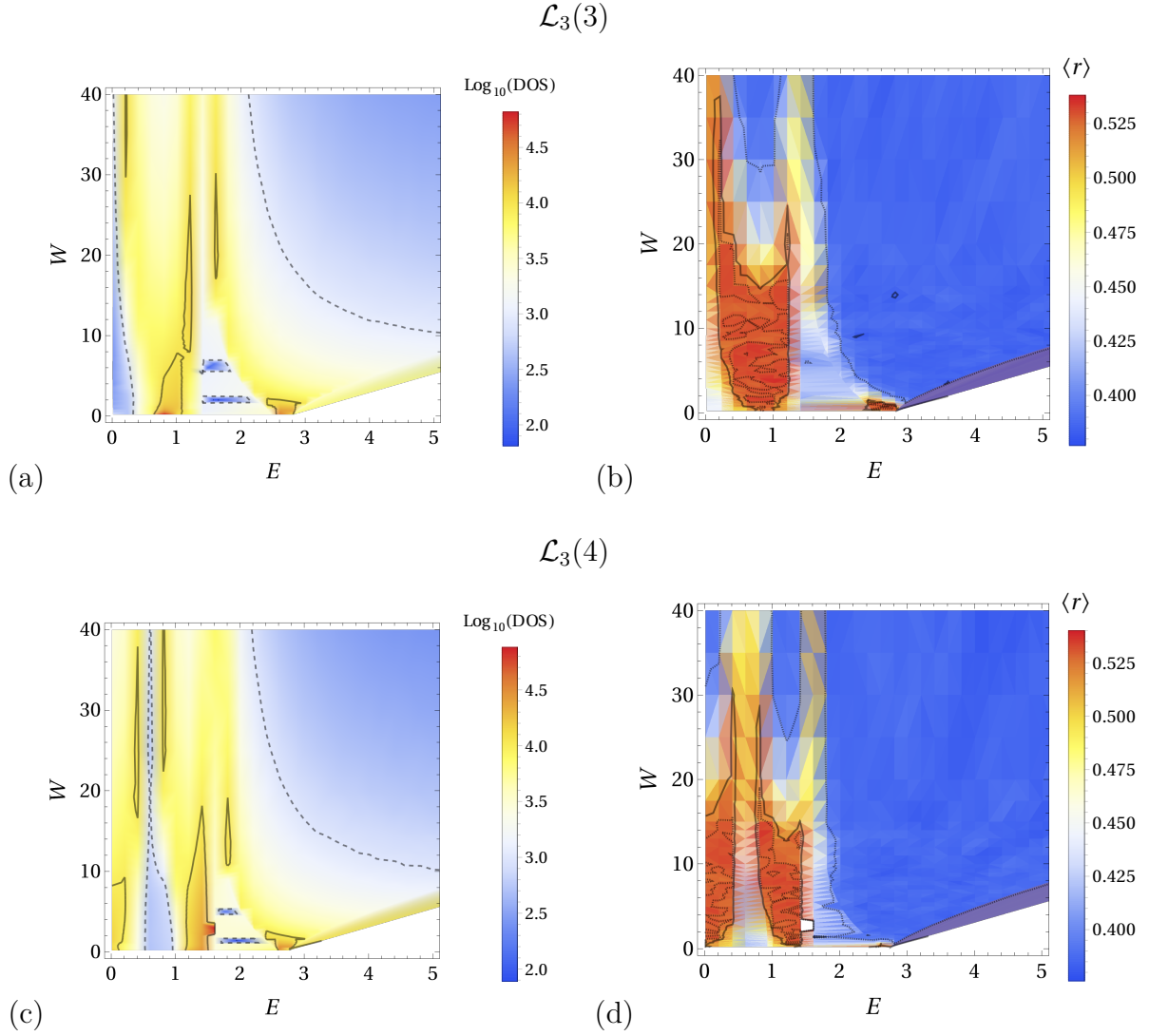
图 6.7: (a,c) DOS and (b,d) r-values for (a,b) $\mathcal{L}_3(3)$ and (c,d) $\mathcal{L}_3(4)$ similar to Fig. 6.6 with a total of 1587 adaptive individual (E, W) pairs. The flat-band states at (a,b) $E = 0$ and $\sqrt{2}$ for $\mathcal{L}_3(3)$ and (c,d) at $E = (\sqrt{5} - 1)/2 \sim 0.618$ and $(1 + \sqrt{5})/2 \sim 1.618$ for $\mathcal{L}_3(4)$ are again not shown in all panels for clarity. The dark lines are also as before, *i.e.* 10^3 (dashed) and 10^4 (solid) in (a,c), while they correspond to $\langle r \rangle = 0.53$ (dashed), 0.5145 (solid) in the red region, $\langle r \rangle = 0.4$ (dashed) and 0.38 (solid) in the blue region in (b,d).
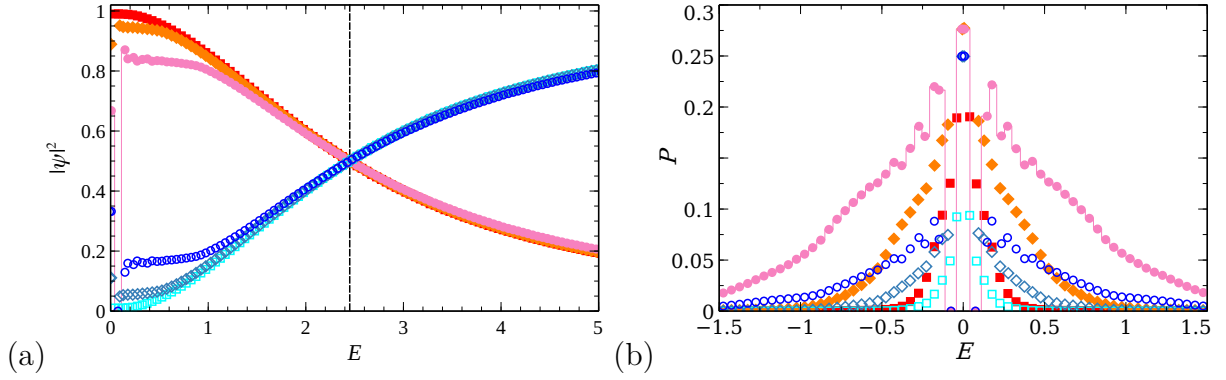
图 6.8: (a) Projected probabilities $|\psi(\vec{r})|^2$ for cube sites (blue colors, open symbols) and Lieb sites (red colors, filled symbols) with disorders $W = 10$ ($\circ$), 20 ($\diamond$) and 50 ($\square$) for $\mathcal{L}_3(1)$ as in Fig. 6.3, but with a different range in E to highlight the crossing point at $E \sim 2.45$ (vertical dashed line). (b) Participation numbers expressed relative to the number of cube and Lieb sites. In both panels, the line for Lieb sites with $W = 10$ is given to highlight that the data points represent averages for 144 potential configurations with energy resolution $\Delta E = 0.05$. The system size in all cases is $L = 4 \times 20^3$.

Chapter7 Summary and outlook

This article primarily investigates the localization properties of two-dimensional and three-dimensional Lieb models and their extended versions. Our research findings include:

1. For the two-dimensional Lieb model and its extended version with onsite potentials following a uniform random distribution, the density of states (DOS) peak originating from the flat band is rapidly destroyed by disorder. States at the flat band and those at the dispersion band exhibit distinctly different localization properties; states at the flat band seem to manifest a localization similar to a one-dimensional scenario. However, for disorder strengths as low as $W \sim t$, all states become localized.

2. Extending the above scenario to three dimensions, the DOS peak originating from the flat band is similarly rapidly destroyed by disorder. The three-dimensional Lieb model and its extended versions exhibit a lower critical disorder strength W_c compared to a simple cubic lattice, indicating a stronger localization tendency in the Lieb model. However, the critical exponent at the transition point remains unchanged.

3. After introducing correlated disorder, i.e., considering a combination of ordered and disordered potentials, high degeneracy energy levels and compact localized states (CLS) continue to exist, while ensuring the presence of disorder. Interestingly, the existence of CLS seems to lead to a divergence of the mobility edge and a potential "inverse" Anderson transition in low-disorder regimes. The divergence of the mobility edge primarily arises from the fact that with increasing disorder strength W, half of the states from the non-dispersive band tend to approach the CLS states in terms of energy and spatial distribution, resulting in an accumulation of states near CLS and thus causing the divergence of the mobility edge.

4. Furthermore, building upon the aforementioned work, we discover that uniform random disorder is not necessary for enhancing CLS; a constant potential with a smaller disorder strength is sufficient.

As mentioned earlier, CLS may belong to a category of states relevant to future information storage devices. While solid-state devices with selectively highly correlated ordered/disordered distributions are unlikely to be realized in the near future, a simpler approach might involve cold atoms in optical lattices [58,125,126] or photonic bandgap systems [59–63,127], where modulation of single lattice site potentials has become a routine operation [120]. Therefore, our results may offer new insights for future information storage devices.

We emphasize that our results are based on a uniform random distribution of diagonal

disorder. For non-diagonal disorder cases, interesting effects such as special energy levels like $E = 0$ can arise due to the chiral symmetry of pure non-diagonal disorder [128–130]. How these cases interact with the flat band of the Lieb model presents an intriguing avenue for further investigation. Additionally, many-body and non-Hermitian problems [131, 132] represent cutting-edge areas, and exploring what new phenomena the flat band may exhibit in such contexts is worth exploring.

参考文献

[1] Anderson P. W. Absence of Diffusion in Certain Random Lattices[J]. Physical Review, 1958, 109(5): 1492-1505.

[2] Kramer B, MacKinnon A. Localization: theory and experiment[J]. Reports on Progress in Physics, 1993, 56(12): 1469-1564.

[3] Evers F, Mirlin A. D. Anderson transitions[J]. Reviews of Modern Physics, 2008, 80(4): 1355-1417.

[4] Belitz D, Kirkpatrick T. R. The Anderson-Mott transition[J]. Reviews of Modern Physics, 1994, 66(2): 261-380.

[5] Wegner F. J. Electrons in disordered systems. Scaling near the mobility edge[J]. Zeitschrift für Physik B Condensed Matter and Quanta, 1976, 25(4): 327-337.

[6] Slevin K, Ohtsuki T. Corrections to Scaling at the Anderson Transition[J]. Physical Review Letters, 1999, 82(2): 382-385.

[7] Abrahams E, Anderson P. W, Licciardello D. C, et al. Scaling theory of localization: Absence of quantum diffusion in two dimensions[J]. Physical Review Letters, 1979, 42(10): 673-676.

[8] Thouless D. J. A relation between the density of states and range of localization for one dimensional random systems[J]. Journal of Physics C: Solid State Physics, 1972, 5(1): 77-81.

[9] Billy J, Josse V, Zuo Z, et al. Direct observation of Anderson localization of matter waves in a controlled disorder[J]. Nature, 2008, 453(7197): 891-894.

[10] Flach S, Leykam D, Bodyfelt J. D, et al. Detangling flat bands into Fano lattices[J]. EPL (Europhysics Letters), 2014, 105(3): 30001.

[11] Sutherland B. Localization of electronic wave functions due to local topology[J]. Physical Review B, 1986, 34(8): 5208-5211.

[12] Lieb E. H. Two theorems on the Hubbard model[J]. Physical Review Letters, 1989, 62(10): 1201-1204.

[13] Mielke A. Ferromagnetic ground states for the Hubbard model on line graphs[J]. Journal of Physics A: Mathematical and General, 1991, 24(2): L73-L77.

[14] Tasaki H. Ferromagnetism in the Hubbard models with degenerate single-electron ground states[J]. Physical Review Letters, 1992, 69(10): 1608-1611.

[15] Maimaiti W, Andreanov A, Park H. C, et al. Compact localized states and flat-band generators in one dimension[J]. Physical Review B, 2017, 95(11): 115135.

[16] Dias R. G, Gouveia J. D. Origami rules for the construction of localized eigenstates of the Hubbard model in decorated lattices[J]. Scientific Reports, 2015, 5(1): 16852.

[17] Weimann S, Morales-Inostroza L, Real B, et al. Transport in Sawtooth photonic lattices[J]. Optics Letters, 2016, 41(11): 2414.

[18] Röntgen M, Morfonios C. V, Schmelcher P. Compact localized states and flat bands from local symmetry partitioning[J]. Physical Review B, 2018, 97(3): 035161.

[19] Nandy A, Chakrabarti A. Engineering flat electronic bands in quasiperiodic and fractal loop geometries[J]. Physics Letters A, 2015, 379(43-44): 2876-2882.

[20] Pal B, Saha K. Flat bands in fractal-like geometry[J]. Physical Review B, 2018, 97(19): 195101.

[21] Leykam D, Flach S, Bahat-Treidel O, et al. Flat band states: Disorder and nonlinearity[J]. Physical Review B, 2013, 88(22): 224203.

[22] Leykam D, Bodyfelt J. D, Desyatnikov A. S, et al. Localization of weakly disordered flat band states[J]. The European Physical Journal B, 2017, 90(1): 1.

[23] Ge L. Anomalous Minimum and Scaling Behavior of Localization Length Near an Isolated Flat Band[J]. Annalen der Physik, 2017, 529(8): 1600182.

[24] Bodyfelt J. D, Leykam D, Danieli C, et al. Flatbands under correlated perturbations[J]. Physical Review Letters, 2014, 113(23): 1-5.

[25] Goda M, Nishino S, Matsuda H. Inverse Anderson Transition Caused by Flatbands[J]. Physical Review Letters, 2006, 96(12): 126401.

[26] Shukla P. Disorder perturbed flat bands: Level density and inverse participation ratio[J]. Physical Review B, 2018, 98(5): 054206.

[27] Chen R, Xu D.-H, Zhou B. Disorder-induced topological phase transitions on Lieb lattices[J]. Physical Review B, 2017, 96(20): 205304.

[28] Zhao A, Shen S.-Q. Quantum anomalous Hall effect in a flat band ferromagnet[J]. Physical Review B, 2012, 85(8): 085209.

[29] Takayoshi S, Katsura H, Watanabe N, et al. Phase diagram and pair Tomonaga-Luttinger liquid in a Bose-Hubbard model with flat bands[J]. Physical Review A, 2013, 88(6): 063613.

[30] Tsai W.-F, Fang C, Yao H, et al. Interaction-driven topological and nematic phases on the Lieb lattice[J]. New Journal of Physics, 2015, 17(5): 055016.

[31] Metcalf M, Chern G.-W, Ventra M. D, et al. Matter-wave propagation in optical lattices: geometrical and flat-band effects[J]. Journal of Physics B: Atomic, Molecular and Optical Physics, 2016, 49(7): 075301.

[32] Luo X, Yu Y. Gauge fermions with flat bands and anomalous transport via chiral modes from breaking gauge symmetry[J]. undefined, 2016.

[33] Bercx M, Hofmann J. S, Assaad F. F, et al. Spontaneous particle-hole symmetry breaking of correlated fermions on the Lieb lattice[J]. Physical Review B, 2017, 95(3): 035108.

[34] Parameswaran S. A, Roy R, Sondhi S. L. Fractional quantum Hall physics in topological flat bands[J]. Comptes Rendus Physique, 2013, 14(9-10): 816-839.

[35] Bergholtz E. J, Liu Z. Topological flat band models and fractional chern insulators[J]. International Journal of Modern Physics B, 2013, 27(24): 1330017.

[36] Tang E, Mei J.-W, Wen X.-G. High-Temperature Fractional Quantum Hall States[J]. Physical Review Letters, 2011, 106(23): 236802.

[37] Neupert T, Santos L, Chamon C, et al. Fractional Quantum Hall States at Zero Magnetic Field[J]. Physical Review Letters, 2011, 106(23): 236804.

[38] Sun K, Gu Z, Katsura H, et al. Nearly Flatbands with Nontrivial Topology[J]. Physical Review Letters, 2011, 106(23): 236803.

[39] Savary L, Balents L. Quantum spin liquids: a review[J]. Reports on Progress in Physics, 2017, 80(1): 016502.

[40] Balents L. Spin liquids in frustrated magnets[J]. Nature, 2010, 464(7286): 199-208.

[41] Tasaki H. From Nagaoka's Ferromagnetism to Flat-Band Ferromagnetism and Beyond: An Introduction to Ferromagnetism in the Hubbard Model[J]. Progress of Theoretical Physics, 1998, 99(4): 489-548.

[42] Mielke A, Tasaki H. Ferromagnetism in the Hubbard model[J]. Communications in Mathematical Physics, 1993, 158(2): 341-371.

[43] Ramirez A. P. Strongly Geometrically Frustrated Magnets[J]. Annual Review of Materials Science, 1994, 24(1): 453-480.

[44] Danieli C, Andreanov A, Flach S. Many-body flatband localization[J]. Physical Review B, 2020, 102(4): 041116.

[45] Kuno Y, Orito T, Ichinose I. Flat-band many-body localization and ergodicity breaking in the Creutz ladder[J]. New Journal of Physics, 2020, 22(1): 013032.

[46] Miyahara S, Kusuta S, Furukawa N. BCS theory on a flat band lattice[J]. Physica C: Superconductivity, 2007, 460-462: 1145-1146.

[47] Julku A, Peotta S, Vanhala T. I, et al. Geometric Origin of Superfluidity in the Lieb-Lattice Flat Band[J]. Physical Review Letters, 2016, 117(4): 045303.

[48] Kopnin N. B, Heikkilä T. T, Volovik G. E. High-temperature surface superconductivity in topological flat-band systems[J]. Physical Review B, 2011, 83(22): 220503.

[49] Peotta S, Törmä P. Superfluidity in topologically nontrivial flat bands[J]. Nature Communications, 2015, 6(1): 8944.

[50] Tovmasyan M, Peotta S, Liang L, et al. Preformed pairs in flat Bloch bands[J]. Physical Review B, 2018, 98(13): 134513.

[51] Mondaini R, Batrouni G. G, Grémaud B. Pairing and superconductivity in the flat band: Creutz lattice[J]. Physical Review B, 2018, 98(15): 155142.

[52] Aoki H. Theoretical Possibilities for Flat Band Superconductivity[J]. Journal of Superconductivity and Novel Magnetism, 2020, 33(8): 2341-2346.

[53] Abilio C. C, Butaud P, Fournier T, et al. Magnetic Field Induced Localization in a Two-Dimensional Superconducting Wire Network[J]. Physical Review Letters, 1999, 83(24): 5102-5105.

[54] Drost R, Ojanen T, Harju A, et al. Topological states in engineered atomic lattices[J]. Nature Physics, 2017, 13(7): 668-671.

[55] Slot M. R, Gardenier T. S, Jacobse P. H, et al. Experimental realization and characterization of an electronic Lieb lattice[J]. Nature Physics, 2017, 13(7): 672-676.

[56] Li Z, Zhuang J, Wang L, et al. Realization of flat band with possible nontrivial topology in electronic Kagome lattice[J]. Science Advances, 2018, 4(11).

[57] Jo G.-B, Guzman J, Thomas C. K, et al. Ultracold Atoms in a Tunable Optical Kagome Lattice[J]. Physical Review Letters, 2012, 108(4): 045305.

[58] Shen R, Shao L. B, Wang B, et al. Single Dirac cone with a flat band touching on line-centered-square optical lattices[J]. Physical Review B, 2010, 81(4): 041410.

[59] Taie S, Ozawa H, Ichinose T, et al. Coherent driving and freezing of bosonic matter wave in an optical Lieb lattice[J]. Science Advances, 2015, 1(10): e1500854.

[60] Guzmán-Silva D, Mejía-Cortés C, Bandres M. A, et al. Experimental observation of bulk and edge transport in photonic Lieb lattices[J]. New Journal of Physics, 2014, 16(6): 063061.

[61] Vicencio R. A, Cantillano C, Morales-Inostroza L, et al. Observation of Localized States in Lieb Photonic Lattices[J]. Physical Review Letters, 2015, 114(24): 245503.

[62] Mukherjee S, Spracklen A, Choudhury D, et al. Observation of a Localized Flat-Band State in a Photonic Lieb Lattice[J]. Physical Review Letters, 2015, 114(24): 245504.

[63] Diebel F, Leykam D, Kroesen S, et al. Conical Diffraction and Composite Lieb Bosons in Photonic Lattices[J]. Physical Review Letters, 2016, 116(18): 183902.

[64] Nakata Y, Okada T, Nakanishi T, et al. Observation of flat band for terahertz spoof plasmons in a metallic kagomé lattice[J]. Physical Review B - Condensed Matter and Materials Physics, 2012, 85(20): 1-5.

[65] Kajiwara S, Urade Y, Nakata Y, et al. Observation of a nonradiative flat band for spoof surface plasmons in a metallic Lieb lattice[J]. Physical Review B, 2016, 93(7): 075126.

[66] Zong Y, Xia S, Tang L, et al. Observation of localized flat-band states in Kagome photonic lattices[J]. Optics Express, 2016, 24(8): 8877.

[67] Xia S, Hu Y, Song D, et al. Demonstration of flat-band image transmission in optically induced Lieb photonic lattices[J]. Optics letters, 2016, 41(7).

[68] Mao X, Liu J, Zhong J, et al. Disorder effects in the two-dimensional Lieb lattice and its extensions[J]. Physica E: Low-Dimensional Systems and Nanostructures, 2020, 124(January): 114340.

[69] Liu J, Mao X, Zhong J, et al. Localization, phases, and transitions in three-dimensional extended Lieb lattices[J]. Physical Review B, 2020, 102(17): 174207.

[70] MacKinnon A, Kramer B. The scaling theory of electrons in disordered solids: Additional numerical results[J]. Zeitschrift für Physik B Condensed Matter, 1983, 53(1): 1-13.

[71] Kramer B, Schreiber M. Transfer-Matrix Methods and Finite-Size Scaling for Disordered Systems[M]. Berlin, Heidelberg: Springer Berlin Heidelberg, 1996, 166-188.

[72] Oseledets V. I. A multiplicative ergodic theorem. characteristic Ljapunov, exponents of dynamical systems[J]. Tr. Mosk. Mat. Obs., 1968, 19: 179-210.

[73] Ishii K. Localization of Eigenstates and Transport Phenomena in the One-Dimensional Disordered System[J]. Progress of Theoretical Physics Supplement, 1973, 53: 77-138.

[74] Beenakker C. W. J. Random-matrix theory of quantum transport[J]. Reviews of Modern Physics, 1997, 69(3): 731-808.

[75] Bollhöfer M, Notay Y. JADAMILU: a software code for computing selected eigenvalues of large sparse symmetric matrices[J]. Computer Physics Communications, 2007, 177(12): 951-964.

[76] L.R. . Statistical theories of spectra: fluctuations[J]. Nuclear Physics, 1966, 78(3): 696.

[77] Guhr T, Müller–Groeling A, Weidenmüller H. A. Random-matrix theories in quantum physics: common concepts[J]. Physics Reports, 1998, 299(4-6): 189-425.

[78] Oganesyan V, Huse D. A. Localization of interacting fermions at high temperature[J]. Physical Review B, 2007, 75(15): 155111.

[79] Atas Y. Y, Bogomolny E, Giraud O, et al. Distribution of the Ratio of Consecutive Level Spacings in Random Matrix Ensembles[J]. Physical Review Letters, 2013, 110(8): 084101.

[80] Sá L, Ribeiro P, Prosen T. Complex Spacing Ratios: A Signature of Dissipative Quantum Chaos[J]. Physical Review X, 2020, 10(2): 021019.

[81] Luo X, Ohtsuki T, Shindou R. Universality Classes of the Anderson Transitions Driven by Non-Hermitian Disorder[J]. Physical Review Letters, 2021, 126(9): 090402.

[82] Liu J, Danieli C, Zhong J, et al. Data for "Unconventional delocalization in three-dimensional Lieb lattices", 2022.

[83] Römer R. A. Numerical methods for localization, 2022.

[84] Mirlin A. D. Statistics of energy levels and eigenfunctions in disordered systems[J]. Physics Report, 2000, 326(5-6): 259-382.

[85] MacKinnon A. Critical exponents for the metal-insulator transition[J]. Journal of Physics: Condensed Matter, 1994, 6(13): 2511-2518.

[86] G. W, Press W. H, Teukolsky S. A, et al. Numerical Recipes in Fortran: The Art of Scientific Computing.[J]. Mathematics of Computation, 1994, 62(205): 433.

[87] Leykam D, Flach S. Perspective: Photonic flatbands[J]. APL Photonics, 2018, 3(7): 070901.

[88] Shukla P. Disorder perturbed flat bands. II. Search for criticality[J]. Physical Review B, 2018, 98(18): 184202.

[89] Ramachandran A, Andreanov A, Flach S. Chiral flat bands: Existence, engineering, and stability[J]. Physical Review B, 2017, 96(16): 161104.

[90] Qiu W.-X, Li S, Gao J.-H, et al. Designing an artificial Lieb lattice on a metal surface[J]. Physical Review B, 2016, 94(24): 241409.

[91] Niţă M, Ostahie B, Aldea A. Spectral and transport properties of the two-dimensional Lieb lattice[J]. Physical Review B, 2013, 87(12): 125428.

[92] Sun M, Savenko I. G, Flach S, et al. Excitation of localized condensates in the flat band of the exciton-polariton Lieb lattice[J]. Physical Review B, 2018, 98(16): 161204.

[93] Biplab Bhattacharya A. P. Flat bands and nontrivial topological properties in an extended Lieb lattice[J]. Physical Review B, 2019, 100(23): 235145.

[94] Leadbeater M, Römer R, Schreiber M. Interaction-dependent enhancement of the localisation length for two interacting particles in a one-dimensional random potential[J]. The European Physical Journal B, 1999, 8(4): 643-652.

[95] Zhang D, Zhang Y, Zhong H, et al. New edge-centered photonic square lattices with flat bands[J]. Annals of Physics, 2017, 382: 160-169.

[96] Edwards J. T, Thouless D. J. Numerical studies of localization in disordered systems[J]. Journal of Physics C: Solid State Physics, 1972, 5(8): 807-820.

[97] Kappus M, Wegner F. Anomaly in the band centre of the one-dimensional Anderson model[J]. Zeitschrift für Physik B Condensed Matter, 1981, 45(1): 15-21.

[98] Römer R. A, Schulz-Baldes H. Weak-disorder expansion for localization lengths of quasi-1D systems[J]. Europhysics Letters (EPL), 2004, 68(2): 247-253.

[99] Danieli C, Bodyfelt J. D, Flach S. Flat-band engineering of mobility edges[J]. Physical Review B, 2015, 91(23): 235134.

[100] Bilitewski T, Moessner R. Disordered flat bands on the kagome lattice[J]. Physical Review B, 2018, 98(23): 1-6.

[101] Nishino S, Matsuda H, Goda M. Flat-Band Localization in Weakly Disordered System[J]. Journal of the Physical Society of Japan, 2007, 76(2): 024709.

[102] MacKinnon A, Kramer B. One-Parameter Scaling of Localization Length and Conductance in Disordered Systems[J]. Physical Review Letters, 1981, 47(21): 1546-1549.

[103] Rodriguez A, Vasquez L. J, Slevin K, et al. Multifractal finite-size scaling and universality at the Anderson transition[J]. Physical Review B, 2011, 84(13): 134209.

[104] Silverman B. W. Density Estimation for Statistics and Data Analysis[M]. Routledge, 2018, 176.

[105] Eilmes A, Fischer A. M, Römer R. A. Critical parameters for the disorder-induced metal-insulator transition in fcc and bcc lattices[J]. Physical Review B, 2008, 77(24): 245117.

[106] Bulka B, Kramer B, MacKinnon A. Mobility edge in the three dimensional Anderson model[J]. Z. Phys. B -Condensed Matter, 1985, 60(1): 13-17.

[107] Tomioka Y, Asamitsu A, Kuwahara H, et al. Magnetic-field-induced metal-insulator phenomena in Pr 1x Ca x MnO 3 with controlled charge-ordering instability[J]. , 1996, 53: 53.

[108] Webman I, Grest G. S. Dynamical behavior of fractal structures[J]. Physical Review B, 1985, 31(3): 1689.

[109] Grussbach H, Schreiber M. Determination of the mobility edge in the Anderson model of localization in three dimensions by multifractal analysis[J]. Physical Review B, 1995, 51(1): 663-666.

[110] Plyushchay I. V, Römer R. A, Schreiber M. Three-dimensional Anderson model of localization with binary random potential[J]. Physical Review B, 2003, 68(6): 064201.

[111] Oseledets V. I. V. I. Oseledets[J]. Physical Review B - Condensed Matter and Materials Physics, 2008, 78(12): 5104-5109.

[112] Xia S, Ramachandran A, Xia S, et al. Unconventional Flatband Line States in Photonic Lieb Lattices[J]. Physical Review Letters, 2018, 121(26): 263902.

[113] Cain P, Roemer R. A, Schreiber M. Phase diagram of the three-dimensional Anderson model of localization with random hopping[J]. Ann. Phys., 1999, 8(5): 507-510.

[114] Aoki H, Ando M, Matsumura H. Hofstadter butterflies for flat bands[J]. Physical Review B, 1996, 54(24): R17296-R17299.

[115] Brandes , Kettemann . Anderson Localization and Its Ramifications[M]. Berlin, Heidelberg: Springer Berlin Heidelberg, 2003, 315.

[116] Aubry S, André G. Analyticity breaking and Anderson localization in incommensurate lattices[J]. Ann. Israel Phys. Soc, 1980, 3(133): 18.

[117] Izrailev F. M, Krokhin A. A. Localization and the Mobility Edge in One-Dimensional Potentials with Correlated Disorder[J]. Physical Review Letters, 1999, 82(20): 4062-4065.

[118] Derzhko O, Richter J, Maksymenko M. Strongly correlated flat-band systems: The route from Heisenberg spins to Hubbard electrons[J]. International Journal of Modern Physics B, 2015, 29(12): 1530007.

[119] Leykam D, Andreanov A, Flach S. Artificial flat band systems: from lattice models to experiments[J]. Advances in Physics: X, 2018, 3(1): 1473052.

[120] Leykam D, Flach S. Perspective: Photonic flatbands[J]. APL Photonics, 2018, 3(7): 070901.

[121] Röntgen M, Morfonios C. V, Brouzos I, et al. Quantum Network Transfer and Storage with Compact Localized States Induced by Local Symmetries[J]. Physical Review Letters, 2019, 123(8): 080504.

[122] Chalker J. T, Pickles T. S, Shukla P. Anderson localization in tight-binding models with flat bands[J]. Physical Review B, 2010, 82(10): 104209.

[123] Čadež T, Kim Y, Andreanov A, et al. Metal-insulator transition in infinitesimally weakly disordered flat bands[J]. Physical Review B, 2021, 104(18): L180201.

[124] Rodriguez A, Vasquez L. J, Römer R. A. Multifractal analysis of the metal-insulator transition in the three-dimensional Anderson model. II. Symmetry relation under ensemble averaging[J]. Physical Review B, 2008, 78(19): 195107.

[125] Goldman N, Urban D. F, Bercioux D. Topological phases for fermionic cold atoms on the Lieb lattice[J]. Physical Review A, 2011, 83(6): 063601.

[126] Apaja V, Hyrkäs M, Manninen M. Flat bands, Dirac cones, and atom dynamics in an optical lattice[J]. Physical Review A, 2010, 82(4): 041402.

[127] Nixon M, Ronen E, Friesem A. A, et al. Observing Geometric Frustration with Thousands of Coupled Lasers[J]. Physical Review Letters, 2013, 110(18): 184102.

[128] Soukoulis C. M, Economou E. N. Off-diagonal disorder in one-dimensional systems[J]. Phys. Rev. B, 1981, 24: 5698.

[129] Soukoulis C. M, Webman I, Grest G. S, et al. Study of electronic states with off-diagonal disorder in two dimensions[J]. Phys. Rev. B, 1982, 26: 1838-1841.

[130] Eilmes A, Römer R, Schreiber M. The two-dimensional Anderson model of localization with random hopping[J]. The European Physical Journal B, 1998, 1(1): 29-38.

[131] Ashida Y, Gong Z, Ueda M. Non-Hermitian physics, 2020.

[132] Bender C. M. Making sense of non-Hermitian Hamiltonians[J]. Reports on Progress in Physics, 2007, 70(6): 947-1018.

Academic papers published during the school

- Academic papers

[1] **Author**, xxx, xxx, and xxx, Unconventional Delocalization in a Family of Three-Dimensional Lieb Lattices, Phys. Rev. B 106, 214204 (2022). （一作，SCI 二区，物理类 Top）

[2] **Author**, xxx, xxx, and xxx, Localization Properties in Lieb Lattices and Their Extensions, Ann. Phys. (N. Y). 435, 168544 (2021). （一作，SCI 三区）

[3] **Author**, xxx, xxx, and xxx, Localization, Phases, and Transitions in Three-Dimensional Extended Lieb Lattices, Phys. Rev. B 102, 174207 (2020). （一作，SCI 二区，物理类 Top）

[4] xxx, **Author**, xxx, and xxx, Disorder Effects in the Two-Dimensional Lieb Lattice and Its Extensions, Phys. E Low-Dimensional Syst. Nanostructures 124, 114340 (2020). （二作，SCI 三区）

- Scientific research project

[1] Lieb 模型及其扩展模型的局域化性质研究，获批日期：2021 年，项目来源：湖南省研究生科研创新项目（Postgraduate Scientific Research Innovation Project of Hunan province），项目经费 3 万元，项目编号 CX20210515。（主持）